BAR-ILAN UNIVERSITY

Opto-Mechanical Interactions in Few-Mode Fibers

Elad Layosh

Submitted in partial fulfillment of the requirements for the Master's Degree in the Alexander Kofkin Faculty of Engineering,

Bar-Ilan University

Ramat Gan, Israel 2025

This work was carried out under the supervision of Prof. Avi Zadok, The Alexander Kofkin Faculty of Engineering, Bar-Ilan University

Acknowledgments

"*Success is the sum of small efforts - repeated day in and day out*" (R. Collier)

The past few years, during which I worked on my M.Sc. degree, have been the most intense and meaningful years of my life. These years were marked by both professional development and personal growth, during which I learned extensively about electro-optics and about myself. Looking back, I realize how much I have progressed through small, consistent efforts that resulted in the following thesis.

First and foremost, I would like to express my deep gratitude to my supervisor and advisor, Prof. Avi Zadok, who has guided me throughout this journey, both professionally and personally. His support and guidance during my M.Sc. studies and military service, both regular and reserve duty, were invaluable, and I sincerely appreciate his dedication. The care he has shown to me and to all members of our group is truly remarkable and should not be taken for granted. I am deeply grateful for his trust and his personal support.

I would also like to thank my fiber team members, Elad Zehavi and Alon Bernstein, for their continuous support in both discussions and experiments. They taught me and guided me through my initial steps in the lab, helping me gain confidence and independence in my research.

Next, I would like to extend my thanks to the rest of our research group members: Dr. Mirit Hen, Inbar Shafir, Shai Ben-Ami, Matan Slook, Leroy Dokhanian, Rafael Suna, Maayan Holsblat, Ori Pearl, and Shahaf Noimark. Their help and support during our daily work, lunch breaks, and group meetings were greatly appreciated.

I would also like to express my gratitude to the former members of our research group: Dr. Hagai Diamandi, Dr. Yosef London, and Dr. Gil Bashan. They welcomed me into the group during my final year of B.Sc. studies and guided me through my final project, introducing me to the fascinating field of fiber opto-mechanics.

I am deeply thankful to the Faculty of Engineering at Bar-Ilan University for their support and scholarship, which allowed me to focus on my research. The staff consistently showed me great care and were always willing to assist whenever needed.

My sincere thanks also go to the Institute for Nanotechnology and Advanced Materials at Bar-Ilan University (BINA) for their continued support and scholarship.

I also wish to express my gratitude to the brave soldiers of the IDF, who fight to protect us and maintain our daily lives. Along with all the people of our country, I hope for the safe return of the hostages and the recovery of all those injured.

Last but not least, I owe my deepest gratitude to my family. To my parents, Yishai and Yael, whose constant encouragement has driven my passion for knowledge and hard work. To my beloved wife, Rotem, who entered my life during my research and continues to support and motivate me. I would also like to honor my late grandfather, Israel Fridchay, who passed away last year. He was the pillar of our family, always offering his support and satisfaction, and sharing his life experience.

Table of Contents

Abstract i

1. Background 1

1.1. Optical fibers 1

1.2. Brillouin scattering in standard optical fibers 1

1.2.1. Backward scattering: applications in lasers and sensing 1

1.2.2. Forward Brillouin scattering 3

1.3. Forward Brillouin scattering sensing of media outside the fiber cladding 4

1.4. Few-mode fibers and their application in space division multiplexing 6

1.5. Brillouin scattering interactions through multiple optical modes 7

1.5.1. Demonstration in photonic integrated circuits 7

1.5.2. Forward scattering in polarization maintaining fibers and thin tapered fibers 8

1.5.3. Backward scattering in few-mode fibers 11

2. Objectives 13

3. Theoretical analysis 14

3.1. Guided optical core modes in standard optical fibers 14

3.1.1. Guided optical core modes in step-index fibers 14

3.1.2. The linearly polarized mode groups 19

3.2. Guided acoustic cladding modes in optical fibers 21

3.2.1. Basic definitions 21

3.2.2. The torsional-radial acoustic cladding modes 22

3.2.3. Classification of the torsional-radial modes 26

3.2.4. Dispersion relations of the torsional-radial modes 27

3.3. The driving force: electro-striction 28

3.3.1. Derivation of the driving force 28

3.3.2. Wavenumbers of driving forces 30
3.3.3. Excitation of acoustic modes with arbitrary azimuthal orders 31
3.4. Scattering of light by acoustic waves: photoelasticity 33
3.4.1. Derivation of the dielectric perturbation tensor 33
3.4.2. Photoelastic coupling between optical and acoustic waves 34
3.4.3. Equivalence of electro-striction and photoelasticity spatial overlap integrals 36
3.5. Forward Brillouin scattering in few-mode fibers 38
3.5.1. The opto-mechanical nonlinear coefficient 38
3.5.2. Phase modulation of probe waves 39
3.5.3. Polarization rotation of probe waves 43
3.5.4. Coupling of power between pump waves 45
4. Numerical analysis 48
5. Experimental setup and results 54
5.1. Experimental setup for intra-modal measurements 54
5.2. Experimental setup for inter-modal measurements 56
5.3. Results: forward Brillouin scattering spectra in a few-mode fiber 57
5.4. Sensing demonstration 64
6. Summary and discussion 66
6.1. Main results 66
6.2. Limitations 67
6.3. Future works 67
References 69
תקציר ..... א

List of Symbols

Symbol	Units in S.I.	Description
$[A, B, C]$	$[m^2]$	Vector of coefficients of an acoustic wave displacement profile
A_i	$[V]$	Complex magnitude of electric field propagating in optical mode i
$[A_l, C_l]$	$[V/m]$	Vector of coefficients of the axial component of the electric field profile
A_{pm}, C_{pm}	$[m^2]$	Coefficients of the normalized transverse displacement profile of a TR_{pm} acoustic mode
A_s	$[V]$	Complex magnitude of the optical probe field
A_{total}	$[V]$	Complex magnitude of the total optical probe field with its sidebands
$A_{\pm}$	$[V]$	Complex magnitude of the sidebands of the optical probe field
$[B_l, D_l]$	$[A/m]$	Vector of coefficients of the axial component of the magnetic field profile
D_{pm}	$[1/m^2]$	Normalization factor of the transverse displacement profile of a TR_{pm} acoustic mode
$\vec{E}$	$[V/m]$	Electric field vector
$\tilde{E}$	$[V/m]$	spatial dependence of the electric field vector
E_i	$[V/m]$	Spatial component of the electric field vector, $i \in \{x, y, z\}/\{r, \phi, z\}$
$\vec{E}_s$	$[V/m]$	Electric field vector of the optical probe
$\vec{E}_{T,ln}^{(EH)}$	$[1/m]$	Normalized transverse profile of the electric field vector for an EH optical mode with azimuthal order l and radial order n. $l, n \in \mathbb{N}$
$\vec{E}_{T,ln}^{(HE)}$	$[1/m]$	Normalized transverse profile of the electric field vector for an HE optical mode with azimuthal order l and radial order n. $l, n \in \mathbb{N}$

$\vec{E}_{T,ln}^{(LP)}$	$[1/m]$	Normalized transverse profile of the electric field vector for an LP optical mode group with azimuthal order l and radial order n. $l, n \in \mathbb{N}$
$\vec{E}_{T,0n}^{(TE)}$	$[1/m]$	Normalized transverse profile of the electric field vector for a TE optical mode with radial order n. $n \in \mathbb{N}$
$\vec{E}_{T,0n}^{(TM)}$	$[1/m]$	Normalized transverse profile of the electric field vector for a TM optical mode with radial order n. $n \in \mathbb{N}$
$E_{ln}^{(EH)}$	$[1/m^2]$	Normalization factor of the electric field transverse profile for an EH optical mode
$E_{ln}^{(HE)}$	$[1/m^2]$	Normalization factor of the electric field transverse profile for an HE optical mode
$\vec{E}_{1,2}$	$[V/m]$	Electric field vectors of the pump waves propagating at optical modes 1 and 2
$\vec{E}_{T,1,2}$	$[1/m]$	Normalized transverse profiles of the two pump waves
$E_{i,1,2}$	$[1/m]$	Vector component of the electric fields' transverse profiles of the pump waves, $i \in \{x, y\}/\{r, \phi\}$
$\vec{E}_{\pm}$	$[V/m]$	Electric field vector of the optical probe's sidebands
EH_{ln}		The EH guided optical mode in the fiber with azimuthal order l and radial order n. $l, n \in \mathbb{N}$
$\vec{F}_{1,2}$	$[N/m^3]$	The electro-strictive force per unit volume driven by the two pump fields
$F_{i,1,2}$	$[N/m^3]$	Vector component of the electro-strictive driving force, , $i \in \{x, y\}/\{r, \phi\}$
$G_{ln}^{(EH)}$	$[1/m]$	Radial profile of the transverse electric field of an EH optical mode
$G_{ln}^{(HE)}$	$[1/m]$	Radial profile of the transverse electric field of an HE optical mode
$G_{ln}^{(LP)}$	$[1/m]$	Radial profile of the transverse electric field of an LP optical mode group
$H(\Omega)$		Complex-valued frequency response of F-SBS measured in the experimental setup

$\widetilde{H}(\Omega)$		Complex-valued frequency response of F-SBS without Kerr effect contribution
H_i	$[A/m]$	Spatial component of the magnetic field vector, $i \in \{x, y, z\}/\{r, \phi, z\}$
HE_{ln}		The HE guided optical mode in the fiber with azimuthal order l and radial order n. $l, n \in \mathbb{N}$
$\boldsymbol{I}_{1,2}$	$[1/m^2]$	Second-order tensor of cross-products between the normalized components of the pump fields
$I_{ij,1,2}$	$[1/m^2]$	Elements of the tensor of cross-products, $i, j \in \{x, y\}/\{r, \phi\}$
K	$[1/m]$	Axial wavenumber of an acoustic wave
K_{inter}, K_{intra}	$[1/m]$	Axial wavenumbers of acoustic waves stimulated by intra-modal and inter-modal processes
L	$[m]$	Fiber length
LP_{ln}		The linearly polarized optical mode group with azimuthal order l and radial order n. $l, n \in \mathbb{N}$
$\boldsymbol{M}_p$		Matrix of coefficients describing the boundary conditions equations of guided acoustic modes
$P(\Omega, z)$	$[W]$	Optical beating power between the pump waves
$P_{1,2}(z)$	$[W]$	Optical power levels of the pump waves
$P_p(\Omega)$	$[V]$	Magnitude of pump power modulation measured in the experimental setup
$\vec{P}_{pm}^{NL}$	$[C/m^2]$	Nonlinear polarization induced by dielectric perturbations associated with a TR_{pm} acoustic mode
$\vec{P}_{pm,\pm}^{NL}$	$[C/m^2]$	Nonlinear polarization driving the probe field's sidebands
$\vec{P}_{pm,\pm\frac{1}{2}}^{NL}$	$[C/m^2]$	Nonlinear polarization coupling between pump fields
$Q_{1,2,pm}^{(ES)}$	$[1/m^2]$	Spatial overlap integral between the transverse profiles of the electro-strictive force driven by optical modes 1,2 and the acoustic TR_{pm} mode displacement

$Q_{1,2,pm}^{(PE)}$	$[1/m^2]$	Spatial overlap integral between the transverse profiles of the two optical modes 1,2 and the dielectric perturbations induced by the acoustic TR_{pm} mode
$Q_{1,2,pm}$	$[1/m^2]$	Equivalent spatial overlap integral of both electro-striction and photoelasticity
R_{0m}		The purely radial guided acoustic mode in the fiber with radial order m. $m \in \mathbb{N}$
$S(\Omega)$	$[V]$	Magnitude of the detected signal wave measured in the experimental setup
$\boldsymbol{S}$		The second-order strain tensor
$\boldsymbol{S}_{pm}$		The second-order strain tensor associated with an acoustic TR_{pm} mode
S_{ij}		Elements of the strain tensor, $i,j \in \{x,y,z\}/\{r,\phi,z\}$
$\boldsymbol{T}$	$[N/m^2]$	The second-order stress tensor
T_{ij}	$[N/m^2]$	Elements of the stress tensor, $i,j \in \{x,y,z\}/\{r,\phi,z\}$
T_{0m}		The purely torsional guided acoustic mode in the fiber with radial order m. $m \in \mathbb{N}$
TE_{0n}		The transverse-electric guided optical mode in the fiber with radial order n. $n \in \mathbb{N}$
TM_{0n}		The transverse-magnetic guided optical mode in the fiber with radial order n. $n \in \mathbb{N}$
TR_{pm}		The torsional-radial guided acoustic mode in the fiber with azimuthal order p and radial order m. $p,m \in \mathbb{N}$
$\vec{U}$	$[m]$	Material displacement vector
U_i	$[m]$	Elements of the material displacement vector, $i \in \{x,y,z\}/\{r,\phi,z\}$
$\vec{U}_{pm}$	$[m]$	Material displacement vector of a given acoustic TR_{pm} mode
V		Parameter which governs the number of optical modes guided in the fiber
a	$[m]$	Radius of the fiber core

b	$[m]$	Radius of the fiber cladding
$b_{pm}(\Omega, z)$	$[m^2]$	Modal magnitude of the TR_{pm} guided acoustic mode
c	$[m/s]$	The speed of light in vacuum
$\boldsymbol{c}$	$[N/m^2]$	The fourth-order stiffness tensor
c_{ijkl}	$[N/m^2]$	Elements of the stiffness tensor, $i, j, k, l \in \{x, y, z\}/\{r, \phi, z\}$
c_{12}, c_{44}	$[N/m^2]$	Elements of the stiffness tensor of silica in abbreviated notation
$\hat{\boldsymbol{e}}$		Unit vector of an arbitrary state of polarization
$f_{1,2}$	$[Hz]$	Intermediate frequencies used for intensity modulation in the experimental setup
$\vec{f}_{1,2}$	$[1/m^3]$	Normalized transverse profile of the electro-strictive driving force
$f_{i,1,2}$	$[1/m^3]$	Vector component of the normalized transverse profile of the electro-strictive driving force, $i \in \{x, y\}/\{r, \phi\}$
$h(t)$		Impulse response of F-SBS measured in the experimental setup
$\tilde{h}(t)$		Impulse response of F-SBS without Kerr effect contribution
h_{ln}^{clad}	$[1/m]$	Wavenumber used in the spatial profile of an optical mode in the fiber cladding
h_{ln}^{core}	$[1/m]$	Wavenumber used in the spatial profile of an optical mode in the fiber core
k_0	$[1/m]$	Vacuum wavenumber of an optical wave
k_{tl}	$[1/m]$	Transverse component of the acoustic wave vector describing dilatational movement
k_{ts}	$[1/m]$	Transverse component of the acoustic wave vector describing shear movement
$l_{1,2}$		Azimuthal orders of the pumps optical modes 1,2
n_0		Refractive index of silica
n_1		Refractive index of the fiber core
n_2		Refractive index of the fiber cladding
$n_{\mathrm{eff},i}$		Effective refractive index of an optical mode i

p		Azimuthal order of a guided acoustic mode
$\boldsymbol{p}$		The fourth-order photo-elastic tensor
p_{ijkl}		Elements of the photo-elastic tensor, $i,j,k,l \in \{x,y,z\}/\{r,\phi,z\}$
p_{11}, p_{12}, p_{44}		Elements of the photo-elastic tensor of silica in abbreviated notation
$\{\hat{\boldsymbol{r}}, \hat{\boldsymbol{\phi}}, \hat{\boldsymbol{z}}\}$		Unit vectors of the cylindrical coordinate system
$\boldsymbol{s}_{pm}$	$[1/m^2]$	Normalized symmetric strain tensor associated with a TR_{pm} acoustic mode
$s_{ij,pm}$	$[1/m^2]$	Elements of the normalized strain tensor, $i,j \in \{x,y\}/\{r,\phi\}$
t	$[s]$	Time
$\vec{u}_{pm}$	$[1/m]$	Normalized transverse displacement profile of a TR_{pm} acoustic mode
$u_{i,pm}$	$[1/m]$	Vector component of the normalized transverse displacement profile of a TR_{pm} acoustic mode, $i \in \{x,y\}/\{r,\phi\}$
v_L	$[m/s]$	Acoustic velocity of dilatational waves in silica
v_S	$[m/s]$	Acoustic velocity of shear waves in silica
v_{phase}	$[m/s]$	Phase velocity of a guided optical mode
$\{\hat{\boldsymbol{x}}, \hat{\boldsymbol{y}}, \hat{\boldsymbol{z}}\}$		Unit vectors of the Cartesian coordinate system
$\Gamma(\Omega)$	$[rad/s]$	Acoustic dissipation parameter
Γ_{pm}	$[rad/s]$	Modal linewidth and energy decay rate of a TR_{pm} acoustic mode
$\Delta\boldsymbol{\varepsilon}$		The second-order dielectric perturbation tensor
$\Delta\varepsilon_{ij}$		Elements of the dielectric perturbation tensor, $i,j \in \{x,y,z\}/\{r,\phi,z\}$
$\Delta\boldsymbol{\varepsilon}_{pm}$		Dielectric perturbation tensor associated with a given TR_{pm} acoustic mode
$\Delta\varphi_{pm}$	$[rad]$	Phase accumulation associated with F-SBS for a given TR_{pm} acoustic mode

$\Delta\varphi_{total}$	$[rad]$	Phase accumulation associated with F-SBS for a given TR_{pm} acoustic mode and Kerr nonlinearity
Ω	$[rad/s]$	Radio frequency
Ω_B	$[rad/s]$	The Brillouin frequency shift of B-SBS
Ω_{pm}	$[rad/s]$	Cut-off frequency of a TR_{pm} acoustic mode
$\Omega_{pm}^{(\mathrm{R})}$	$[rad/s]$	Resonance frequency of maximum Brillouin interaction for a given TR_{pm} acoustic mode
β_i	$[1/m]$	Axial propagation constant of optical mode i
β_{ln}	$[1/m]$	Axial propagation constant of an optical mode with azimuthal order l and radial order n. $l, n \in \mathbb{N}$
β_s	$[1/m]$	Axial propagation constant of the optical probe wave
$\beta_{\pm}$	$[1/m]$	Axial propagation constant of the probe's sidebands
$\gamma_{1,2,pm}$	$[1/(W \cdot m)]$	The opto-mechanical nonlinear coefficient of F-SBS between a pair of optical modes 1 and 2 and an acoustic mode TR_{pm}
$\gamma_{1,2,pm}^{(0)}$	$[1/(W \cdot m)]$	Maximum value of the opto-mechanical coefficient for a pair of optical modes 1 and 2 and an acoustic mode TR_{pm}
$\gamma_{1,2,total}$	$[1/(W \cdot m)]$	The total opto-mechanical spectrum comprising all acoustic TR_{pm} modes participating in the F-SBS process
γ_{Kerr}	$[1/(W \cdot m)]$	The nonlinear coefficient associated with the Kerr effect
ε_0	$[N/V^2]$	Vacuum permittivity
μ_0	$[N/A^2]$	Vacuum permeability
$\boldsymbol{\mu}_{pm}$	$[1/m^2]$	The normalized dielectric perturbation tensor associated with an acoustic TR_{pm} mode
$\mu_{ij,pm}$	$[1/m^2]$	Elements of the normalized dielectric perturbation tensor, $i, j \in \{x, y\}/\{r, \phi\}$
ρ_0	$[kg/m^3]$	Material density of silica
$\boldsymbol{\sigma}_{1,2}$	$[N/m^2]$	The second-order electro-strictive stress tensor associated with two pump waves at optical modes 1,2
$\sigma_{ij,1,2}$	$[N/m^2]$	Elements of the electro-strictive stress tensor, $i, j \in \{x, y, z\}/\{r, \phi, z\}$
$\tilde{\boldsymbol{\sigma}}_{1,2}$	$[1/m^2]$	The normalized transverse stress tensor

$\tilde{\sigma}_{ij,1,2}$	$[1/m^2]$	Elements of the normalized stress tensor, $i,j \in \{x,y\}/\{r,\phi\}$
φ	$[rad]$	Phase accumulation
ω_i	$[rad/s]$	Optical frequency of a field propagating in optical mode i
ω_p	$[rad/s]$	Mean optical frequency of two pump waves
ω_s	$[rad/s]$	Optical frequency of the probe field

List of Acronyms

B-SBS	Backward stimulated Brillouin scattering
dB	Decibel
EDFA	Erbium-doped fiber amplifier
EOM	Electro-optic modulator
FMF	Few-mode fiber
F-SBS	Forward stimulated Brillouin scattering
LP	Linearly polarized
MDM	Mode division multiplexer
PC	Polarization controller
PM	Polarization-maintaining
RIU	Refractive index units
SBS	Stimulated Brillouin scattering
SDM	Space division multiplexing
SMF	Single-mode fiber
SSB	Single-sideband
TE	Transverse-electric
TM	Transverse-magnetic
TR	Torsional-radial
WDM	Wavelength division multiplexing

List of Figures

Figure 1 – Schematic illustartion of mechanisms that provide a postive feedback in backward SBS over standard fibers ……2

Figure 2 – Dispersion relations between temporal frequency and axial wavenumber in forward SBS……3

Figure 3 – Measured forward SBS spectra of the TR_{2m} modes in a bare fiber immersed in water (solid blue) and kept in air (dashed black)……5

Figure 4 – Top: Schematic illustration of inter-modal forward SBS over a silicon waveguide. Middle: Schematic of the three modes participating in the inter-modal Brillouin process: the two optical modes and the acoustic mode that couples between them. Bottom: Operation scheme of the inegrated mode multiplexers ……6

Figure 5 – Calculated normalized transverse $\hat{\boldsymbol{x}}$ (left) and $\hat{\boldsymbol{y}}$ (right) components of material displacement in one guided acoustic mode in a PM fiber, with a cut-off frequency of 175MHz……7

Figure 6 – Non-reciprocal cross-polarization coupling of probe waves due to inter-modal forward SBS……8

Figure 7 – Measured optical power of the F-SBS fiber laser signal as a function of the pump power. The bare fiber cavity was kept in air (red), immersed in water for 40% of its length (blue), or fully immersed in water (black)……9

Figure 8 – Schematic illustration of an inter-modal forward SBS interaction in a narrow fiber taper ……9

Figure 9 – Measured (black) and calculated (green) backward SBS gain spectra of intra-modal interactions in the first four LP mode groups of a few-mode fiber……10

Figure 10 – Calculated transverse profiles of electric field vectors in the HE_{11} optical mode in two spatially orthogonal orientations ……15

Figure 11 – Calculated transverse profiles of electric field vectors in the EH_{11} optical mode in two spatially orthogonal orientations ……15

Figure 12 – Calculated transverse profiles of electric field vectors in the TE_{01} (left) and TM_{01} (right) optical modes ……16

Figure 13 – Calculated normalized radial profiles of the electromagnetic intensity of the first four LP mode groups……17

Figure 14 – Calculated effective refractive indices n_{eff} of multiple guided optical mode groups in a standard fiber as a function of the V parameter……18

Figure 15 – Schematic illustation of dispersion curves of the radial guided acoustic modes R_{0m} ……21

Figure 16 – Normalized calculated transverse profiles of material displacement of several guided acoustic cladding modes……22

Figure 17 – Calculated opto-mechanical spectra $|\gamma(\Omega/2\pi)|$ of intra-modal forward SBS between two optical waves in the fundamental LP_{01} mode ……41

Figure 18 – Calculated opto-mechanical spectra $|\gamma(\Omega/2\pi)|$ of intra-modal forward SBS between two optical waves in the LP_{02} mode ……42

Figure 19 – Calculated opto-mechanical gain coefficients $\mathrm{Im}\{\gamma(\Omega/2\pi)\}$ of inter-modal forward SBS between one optical wave in the LP_{01} mode and another in the LP_{02} mode……42

Figure 20 – Calculated opto-mechanical spectra $|\gamma(\Omega/2\pi)|$ of forward SBS between optical waves within the LP_{11} mode group……43

Figure 21 – Calculated opto-mechanical gain coefficients $\mathrm{Im}\{\gamma(\Omega/2\pi)\}$ of inter-modal forward SBS between one optical wave in the LP_{01} mode and another in the LP_{11} mode group……44

Figure 22 – Schematic illustration of the experimental setup used in characterization of intra-modal F-SBS in a few-mode fiber ……46

Figure 23 – Schematic illustration of the experimental setup used in characterization of inter-modal F-SBS in a few-mode fiber ……47

Figure 24 – Measured (solid, blue) and calculated (dashed, red) normalized spectra $\left|\gamma_{LP01,LP01,pm}(\Omega)\right|^2$ of intra-modal forward SBS in the fundamental LP_{01} mode of a few-mode fiber ……48

Figure 25 – Measured (solid, blue) and calculated (dashed, red) normalized spectra $\left|\gamma_{LP02,LP02,pm}(\Omega)\right|^2$ of intra-modal forward SBS in the LP_{02} mode of a few-mode fiber……49

Figure 26 – Measured (solid, blue) and calculated (dashed, red) normalized spectra $\left|\gamma_{LP11,LP11,0m}(\Omega)\right|^2$ of intra-modal forward SBS in the LP_{11} modes group of a few-mode fiber, through the radial acoustic modes R_{0m} ……49

Figure 27 – (a): Measured (solid, blue) and calculated (dashed, red) normalized spectra of intra-modal forward SBS in the LP_{11} modes group of a few-mode fiber, through torsional-radial acoustic modes. (b), (c), (d) and (e): Magnified views of the experimental trace of panel (a) (blue), alongside the measured, normalized torsional-radial modes spectrum of intra-modal scattering in the LP_{01} mode (red) ……50

Figure 28 – Solid blue – measured normalized gain coefficient of inter-modal forward SBS between one optical wave in the fundamental LP_{01} mode and another in the LP_{11} mode group. Dashed red – calculated normalized gain coefficient $\mathrm{Im}\{\gamma_{LP01,LP11,1m}\}$ of inter-modal forward SBS between the two optical modes through the TR_{1m} acoustic modes ……51

Figure 29 – (a): Solid blue – measured normalized gain coefficient of inter-modal forward SBS between one optical wave in the fundamental LP_{01} mode and another in the LP_{02} mode. Dashed red – calculated normalized gain coefficient of the inter-modal scattering process through the R_{0m} and TR_{2m} acoustic modes. (b), (c), (d) and (e): Magnified view of the measured normalized inter-modal scattering spectrum (blue), alongside the measured normalized spectra of intra-modal scattering in the fundamental LP_{01} mode ……52

Figure 30 – Circular markers - Measured spectral offsets $\Delta\Omega/2\pi$ between the resonance frequencies of inter-modal forward SBS through the LP_{01} and LP_{02} modes, and the corresponding resonance frequencies of intra-modal scattering. Solid lines – calculated offsets according to Eq. (98). Modes dominated by their dilatational components are shown in blue, whereas those that are primarily of shear characteristics are shown in red……53

Figure 31 – Measured inter-modal forward SBS gain coefficient of the TR_{1m} modes in a bare few-mode fiber immersed in water (solid blue) and kept in air (dashed black)……54

List of Tables

Table 1 – Parameters of the step-index FMF used in the numerical calculations……40

List of Publications

[1] **E. Layosh**, E. Zehavi, A. Bernstein, M. Hen, M. Holtsblatt, O. Pearl and A. Zadok, “Forward Brillouin Scattering in Few-mode Fibers“, *Light Sci Appl* (under review).

Abstract

Brillouin scattering is an opto-mechanical interaction that couples between optical and acoustic waves in a common medium. The phenomenon has been studied in standard fibers for over 50 years, and it may take place in either the backward or forward directions. In backward interactions, two counter-propagating optical field components may stimulate a longitudinal acoustic mode that is guided in the core of the fiber. In forward Brillouin scattering, two co-propagating optical fields couple with a predominantly transverse acoustic mode that is guided by the entire cladding cross-section. Forward Brillouin scattering in single mode fibers has been formulated and reported in 1985. Interest in the effect has increased in recent years, towards sensing of substances outside the boundaries of standard cladding, where guided light does not reach. The decay rates of the acoustic modes in forward Brillouin scattering interactions are affected by the elastic boundary conditions at the edge of the cladding, and their monitoring enables the analysis of surrounding media.

Most studies of forward Brillouin scattering in standard fibers were carried out in the single-mode regime. A pair of optical fields in the fundamental, single mode may only stimulate acoustic modes of two specific classes: purely radial ones, and modes of two-fold azimuthal symmetry. Although the fiber cladding supports guided acoustic modes of any integer order of azimuthal symmetry, other classes of acoustic modes cannot be addressed through forward Brillouin scattering in single-mode fibers. The efficiency of forward Brillouin scattering scales with the spatial overlap between the transverse profiles of the optical and acoustic modes involved. In standard single-mode fibers, that overlap is maximal for acoustic modes of frequencies between 200-600 MHz. The effect diminishes strongly at higher acoustic frequencies. Lastly, forward Brillouin stimulation of acoustic modes in single-mode fibers is only possible at their cut-off frequencies. At that limit, the acoustic modes are almost entirely transverse, and their axial wavenumbers are vanishingly small.

Over the last decade, few-mode optical fibers have taken an increasing role in space-division multiplexing of optical telecommunication channels, and they have also found many sensing applications. The number of mode groups supported by the fiber can be controlled through the dimensions and index contrast of the core. Few-mode fibers provide additional degrees of freedom for Brillouin scattering interactions, as the optical fields that take part in the process may

be guided in different spatial modes. Brillouin scattering interactions through multiple guided optical modes have been reported in photonic integrated waveguides and in thin tapered fibers. Backward Brillouin scattering interactions have been investigated in standard few-mode fibers, and they were used towards strain and temperature sensing and for modal dispersion analysis. The forward effect has been studied in standard, panda-type polarization maintaining fibers, in which the two polarization modes are non-degenerate. However, the difference in effective indices between the two principal states of the fiber is comparatively small, in the fourth decimal point. In addition, the guided acoustic modes of the panda-type fiber cannot be solved analytically and do not maintain regular azimuthal symmetries. Forward Brillouin scattering in standard few-mode fibers has yet to be examined.

In this work, I report the analysis, calculations, and experimental demonstration of forward Brillouin scattering in a step-index few-mode fiber with standard, uniform cladding. The spectrum of forward Brillouin scattering is formulated for the launch of each of the optical fields involved in an arbitrary guided mode. The experimental setup supported selective coupling of light to the fundamental LP_{01} mode, the LP_{02} mode, or the LP_{11} mode group of a few-mode fiber. The results show that forward Brillouin scattering in the LP_{02} mode reaches acoustic frequencies up to 1.8 GHz, much higher than in the fundamental mode. The measurements demonstrate the Brillouin stimulation of additional classes of acoustic modes, with first-order and fourth-order azimuthal symmetries, which are inaccessible through the corresponding process in single-mode fibers. Further, inter-modal interactions between optical waves in the LP_{01} and LP_{02} modes stimulate acoustic modes that are detuned from their cut-off frequencies by few MHz. Certain inter-modal forward Brillouin interactions signify the transfer of angular momentum quanta between the orbital degrees of freedom of optical and acoustic waves. The results extend the formulation and scope of fiber opto-mechanics beyond the single-mode regime, and they may find applications in fiber lasers, sensing, and quantum states manipulation.

1. Background

1.1. Optical fibers

For decades, the demands for ever higher data communication rates keep growing exponentially. The nearly exclusive technological solution for long-reach, high-rate communication has been optical transmission over silica-based fibers. Optical fibers are dielectric waveguides which exhibit ultra-low losses of only 0.2 dB/km at 1550 nm wavelength [1]. In addition to communication, optical fibers are also utilized as sensors for various metrics of interests, including temperature, deformations, sound and vibrations, and various chemicals [2,3].

The optical fiber is composed of two distinct sections: an inner core region, with a radius of few microns, and an outer cladding layer, usually 125 microns in diameter. The core is doped with few percent of germanium to achieve slightly higher refractive index than that of the cladding. The difference in refractive indices between the core and the cladding, in the order of 0.01 [RIU], enables the propagation of light in guided core modes [1]. Mostly, the core radius and doping are chosen so that only a single spatial mode may be guided within the core of the fiber. These single-mode fibers (SMFs) are free of modal dispersion, and they enable the transfer of Tbits/s of data over thousands of kilometers [1].

1.2. Brillouin scattering in standard optical fibers

1.2.1. Backward scattering: applications in lasers and sensing

Brillouin scattering refers to the nonlinear effect in which light and acoustic waves interact with each other. The effect was first proposed by Leon Brillouin in 1922 [4]. It was first observed in liquids in 1964 [5] and demonstrated in optical fibers in 1972 [6]. Brillouin scattering in standard fibers may take place in either the backward or forward directions [6-13].

In backward stimulated Brillouin scattering (backward SBS or B-SBS), two counter-propagating optical fields, detuned by a radio-frequency offset, induce a propagating beating pattern along the fiber axis [6,12,13]. The axial wavenumber of the travelling beating pattern equals the sum of the wavenumbers of the two optical fields, and its temporal frequency equals the spectral offset between the fields. The intensity beating gives rise to an axial mechanical force, which may excite acoustic core modes with the same wavenumber and frequency of the beating pattern [6,12,13].

Acoustic waves are effectively stimulated when both wavenumber and frequency of the optical beating pattern match those of a guided acoustic mode. That condition is met for a specific acoustic frequency, known as the Brillouin frequency shift Ω_B. In standard SMFs at 1550 nm wavelength, $\Omega_B = 2\pi \times 10.85$ GHz. The linewidth of the acoustic wave is determined by their lifetime: about $2\pi \times 30$ MHz. The acoustic wave, in turn, induces perturbations to the refractive index in the fiber core and creates a moving grating, travelling alongside the acoustic wave. The grating may couple between the two input optical fields, resulting in a positive feedback loop (Figure 1). The entire process may lead to the exponential amplification of the lower frequency tone (signal) at the expense of the higher frequency one (pump) [6,12,13].

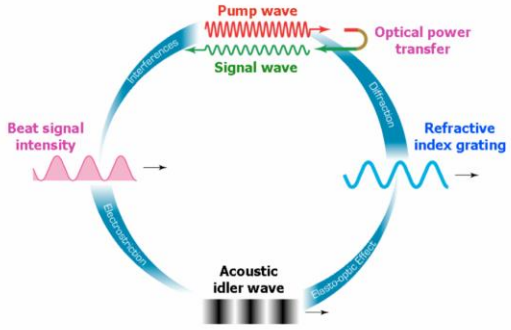

Figure 1 – Schematic illustartion of mechanisms that provide a postive feedback in backward SBS over standard fibers. Image curtsy Luc Thévenaz, EPFL.

The backward SBS effect can be utilized for sensing [14,15]: The Brillouin frequency shift is governed by the dilatational acoustic velocity in the silica, as well as the effective index of the optical core mode. Outside conditions, such as axial strain and temperature, may affect the elastic and optical material properties of the fiber, and shift the resonance frequency of the acoustic mode [14]. Since the pump and signal propagate in opposite directions, the Brillouin scattering spectra may be spatially resolved based on time-of-flight analysis [14]. Therefore, B-SBS measurements support spatially distributed analysis of local strain and temperature conditions [14]. Brillouin fiber sensors reach millimeter-scale spatial resolution [16-19], hundreds of kilometers range [20,21], and precision of sub-degree centigrade and ppm-level strain [22,23].

B-SBS serves as an amplifier for the optical signal at the expense of the pump wave. When the fiber is placed in a feedback loop, spontaneous backward scattering of the pump wave might reach a lasing threshold, resulting in a lasing signal. Fiber laser based on backward SBS was first demonstrated in 1991 using a ring configuration [24], exhibiting ultra-narrow linewidths of few

kHz. Backward Brillouin fiber lasers are used in microwave-photonic signal generation and processing [25], and in fiber-optic gyroscopes [26]. They were also demonstrated in micro-resonator and integrated-photonic platforms [27-31].

1.2.2. Forward Brillouin scattering

In forward stimulated Brillouin scattering (forward SBS or F-SBS), the two optical pump waves participating in the process co-propagate along the fiber axis. The two pump waves induce an electro-strictive driving force, propagating at the beating frequency Ω between the pumps. The electro-strictive driving force in the forward scattering case is mostly confined to the transverse plane. This driving force may excite acoustic waves with the same radio-frequency Ω. Unlike the backward effect, the stimulated acoustic modes span the entire cross-section of the fiber cladding [32].

The most general category of acoustic modes supported by the cylindrical uniform fiber cladding is referred to as the torsional-radial (TR) acoustic modes TR_{pm}. The transverse profiles of material displacement are described by an integer azimuthal order $p \geq 0$ and an integer radial order $m \geq 1$. Each TR mode is characterized by a cut-off frequency Ω_{pm}, below which it may no longer propagate in the axial direction. Close to their cut-offs, the axial components of the phase velocities of the acoustic modes approach infinity. The material displacement vectors of the modes in that limit become predominantly transverse [7,8]. Maximum excitation of the acoustic modes is achieved when the material displacement and electro-strictive driving force at frequency Ω are of equal axial wavenumbers. In standard SMFs, phase matching is achieved in radio-frequencies very close to the cut-off ($\Omega \approx \Omega_{pm}$), where the phase velocity of the acoustic mode may equal to the speed of light in the fiber [7,8].

In SMFs, not all the TR modes are accessible through electro-strictive excitation. Given the one-fold azimuthal symmetry of the fundamental optical mode, the induced electro-strictive force includes only two terms: one that is radially symmetric, and another that follows two-fold azimuthal symmetry [7,11]. For that reason, light waves guided in the single core mode may only excite two classes of acoustic modes: the purely radial ones known as R_{0m}, and the TR_{2m} modes [7,8,11].

The acoustic waves stimulated by electro-striction may scatter an additional optical probe wave through photoelasticity [7,33-35]. Acoustic waves are associated with local deformation of the

medium, which may be expressed in terms of strain. The deformations, in turn, modify the dielectric properties of the fiber medium. The dielectric perturbations themselves propagate along the fiber, hand-in-hand with the acoustic mode, at frequency Ω and with the phase velocity of guided light. The perturbations scatter the probe wave to multiple sidebands and may lead to its phase modulation (in the case of purely radial acoustic modes R_{0m}) or to phase modulation combined with polarization rotation (for any arbitrary TR_{pm} mode) [11]. In addition, the two optical pump tones that stimulate the acoustic mode in the first place are also coupled by that wave: the lower-frequency tone is amplified in the expense of the higher-frequency tone [11].

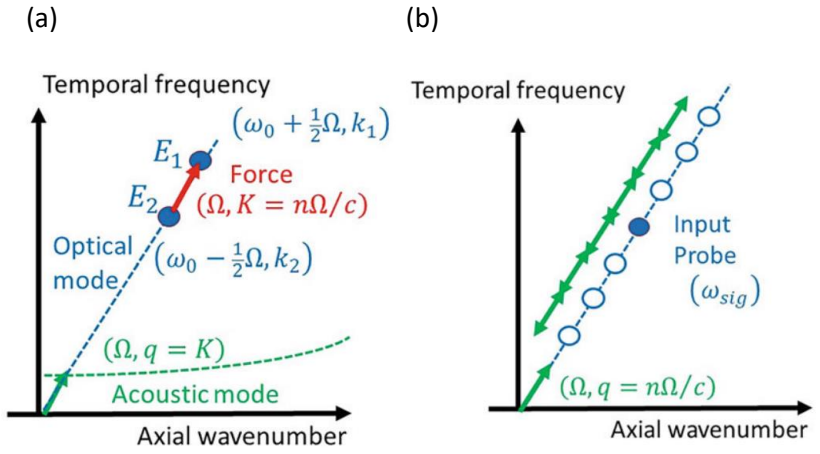

Figure 2 – Dispersion relations between temporal frequency and axial wavenumber in forward SBS. The optical core mode is represented by a dashed blue line, and one guided acoustic mode is represented by dashed green curve with a cut-off frequency. (a) Schematic illustration of the phase matching requirement between the electro-strictive driving force induced by two pump fields ($E_{1,2}$, frequencies $\omega_0 \pm \Omega/2$, wavenumbers $n(\omega_0 \pm \Omega/2)/c$) and a guided acoustic mode. The electro-strictive force takes up frequency Ω and wavenumber $K = n\Omega/c$. Stimulation is possible for acoustic modes of the same Ω, and axial wavenumber $q = K$. That condition implies that the axial phase velocity of the acoustic mode equals the speed of light in the fiber. The condition may be met close to the cut-off frequency of the acoustic mode, where its axial phase velocity approaches infinity. (b) Illustration of a probe wave scattered to multiple side-bands by photo-elastic perturbations associated with the acoustic mode, resulting in its phase modulation [11].

1.3. Forward Brillouin scattering sensing of media outside the fiber cladding

In recent years, the F-SBS effect has raised a growing interest towards the sensing of substances outside the boundaries of standard fiber cladding, where guided light does not reach [11,36-51]. Sensing towards forward SBS was first demonstrated by Antman, London and Clain from our group in 2016, through the radial guided acoustic modes R_{0m} [36]. In that case, the acoustic waves are entirely dilatational in the radial direction. When the fiber is stripped of its protective coating, acoustic waves in the cladding can interact with the outside medium. The decay rates of the acoustic modes are affected by the elastic boundary conditions at the edge of the cladding, and

they may vary between different substances outside the fiber. The decay rates manifest in the spectral linewidths of the acoustic modes, and their monitoring enables the analysis of the surrounding media [36].

The initial F-SBS sensing method required the removal of the standard coating layer of the optical fiber, in order to enable acoustic interaction with the outside medium. However, the use of bare fibers is often impractical. In 2018, Chow and Thévenaz demonstrated F-SBS sensing of surrounding liquids using a fiber coated with a thin polyimide layer [39]. The polyimide-coating layer provides the necessary mechanical protection, and it was also thin enough to allow acoustic wave propagation to the outside liquid. This sensing method was later extended for the elastic characterization of the coating layer itself [42]. F-SBS fiber sensing has been extended to point-measurements over cm-long discrete sections [52] and to spatially distributed analysis [41,53-55]. In most previous demonstrations, only the radial acoustic modes R_{0m} participated in the sensing process.

F-SBS sensors in SMFs were extended through the use of torsional-radial modes of two-fold azimuthal symmetry, known as TR_{2m} modes, by Hayashi and co-workers in 2017 [37]. These modes can be classified in two types: modes that are predominantly dilatational and others with shear-like characteristics [45]. The distinction between the two types was first considered by the group of Andrés in 2022 [45]. In 2023, Bernstein, Zehavi and co-workers from our group demonstrated different sensing behavior between the two types of TR_{2m} modes in a bare SMF [56]: When the fiber was immersed in liquid, the linewidths of dilatational TR_{2m} modes were broadend much like the radial ones, whereas the shear modes' linewidths remained narrow. This observation has been explained by the properities of liquid media: Unlike dilatational movement, liquids do not support shear wave motion. Therefore, a shear wave reaching the interface between the fiber cladding and the liquid cannot propagate outward and becomes reflected back, leading to its slower decay. The monitoring of multiple mode categories enhances the capabilities of forward SBS fiber sensors and provides more complete assessment of the outside media [56].

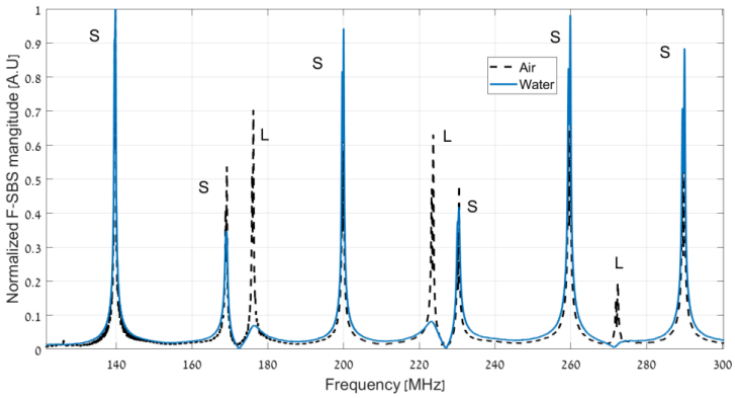

Figure 3 – Measured forward SBS spectra of the TR_{2m} modes in a bare fiber immersed in water (solid blue) and kept in air (dashed black). The linewidths of the dilatational modes (noted by L) are broadened when immersed in water, whereas the shear modes (labeled S) remain narrow [56].

1.4. Few-mode fibers and their application in space division multiplexing

As mentioned in previous sections, optical fibers serve as the main platform for high-rate communication channels. As the data rates kept rising, transmission over a single optical carrier became insufficient, since it was limited to hundreds of Gbit/s by interface electronics. Several technological solutions have been developed to transmit multiple communication channels over a single optical fiber. The primary technique is wavelength division multiplexing (WDM), which refers to the use of several carrier waves in parallel, each with its own distinct wavelength [57-59]. However, even WDM is limited to no more than 100 channels. The further increase in capacity must rely on space division multiplexing (SDM), in which the optical channels are spatially separated [60,61]. Rather than install additional, separate fibers, SDM can be implemented using multiple single-mode cores within the same cladding [60]. The cores are sufficiently separated from each other, to maintain acceptable levels of optical crosstalk.

SDM channels can also be transmitted over multiple optical modes in a single core. With proper design of the core radius and refractive index of the fiber, the number of guided optical mode groups can be controlled. These groups refer to as the linearly polarized (LP) mode groups LP_{ln}, where the integer $l \geq 0$ refers to the azimuthal order and the integer $n \geq 1$ is the radial order [62]. Few-mode fibers (FMFs) support the propagation of the spatially orthogonal LP groups, often up to 20 groups in total. Independent data streams can be multiplexed and transmitted over different mode groups and de-multiplexed at the receiver end [61]. However, crosstalk in such mode-division multiplexing is more substantial than among separate cores. Large scale digital

signal processing is often necessary to undo the coupling accumulated among mode groups over long fibers [61].

1.5. Brillouin scattering interactions through multiple optical modes

1.5.1. Demonstration in photonic integrated circuits

The existence of several guided optical modes extends the possibilities for Brillouin scattering interactions. The optical fields that take part in Brillouin scattering may be guided in different spatial modes, providing additional degrees of freedom to the process. This type of Brillouin interactions refers to as inter-modal processes, and they are markedly different from the intra-modal ones, in which both fields are guided in the same optical mode. In 2017, Eric A. Kittlaus *et.al.* demonstrated inter-modal forward SBS over a silicon waveguide for the first time [63]. Two different optical modes were launched through an integrated mode multiplexer: the fundamental symmetric transverse electric (TE) mode and the first-excited anti-symmetric TE mode. The two fields co-propagated through the active device region and excited a guided acoustic mode in the silicon membrane. The acoustic mode, in turn, coupled between the optical fields through inter-modal forward SBS. Both optical and acoustic modes were solved numerically. Due to different dispersion curves of the optical modes, phase matching was obtained for a single sideband only, resulting by the amplification of that sideband rather than in its phase modulation. This symmetry breaking provided significant unidirectional energy transfer between the optical fields and led to non-reciprocal propagation effects [63]. Inter-modal forward SBS interactions in hybrid photonic-phononic waveguides are markedly stronger than intra-modal ones [63].

In 2018, Nils T. Otterstorm *et.al.* utilized the inter-modal forward SBS over photonic waveguides to demonstrate a silicon Brillouin laser [64]. Pump light was launched through the anti-symmetric optical mode. Feedback for the lasing signal was obtained by a ring cavity, and the single sideband amplification process reached a lasing threshold in the fundamental symmetric optical mode. The laser obtained was ultra-narrow with 20kHz linewidth.

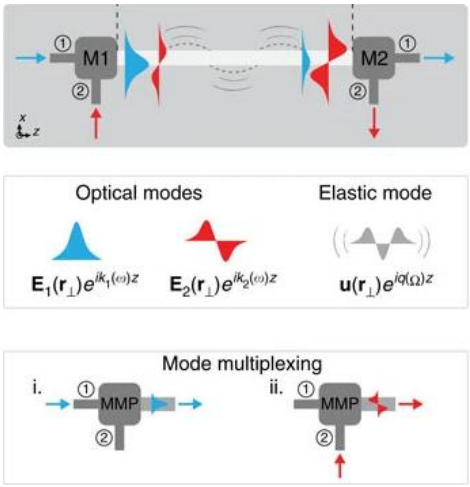

Figure 4 – Top: Schematic illustration of inter-modal forward SBS over a silicon waveguide. Two optical fields are launched through an integrated mode multiplexer (denoted M1) and are coupled into the fundamental symmetirc mode (blue) and the first-excited anti-symmetric mode (red). Optical power is exchanged between the fields by inter-modal F-SBS. The fields are demultiplexed at the end of the waveguide (M2). Middle: Schematic of the three modes participating in the inter-modal Brillouin process: the two optical modes and the acoustic mode that couples between them. Bottom: Operation scheme of the inegrated mode multiplexers [63].

1.5.2. Forward scattering in polarization maintaining fibers and thin tapered fibers

Inter modal forward SBS processes may take place over optical fibers as well. In 2021, Gil Bashan *et. al.* carried out a comprehensive study of forward SBS interactions over a standard, panda-type polarization-maintaining (PM) fiber [65]. The panda fiber includes two strain rods of silica doped with B_2O_3 glass, which induce permanent birefringence between two linear and orthogonal principal axes. The birefringence between the fast axis ($\hat{\boldsymbol{y}}$) and the slow axis ($\hat{\boldsymbol{x}}$) manifests in two orthogonal optical modes with a difference of about 10^{-4} refractive index units between their effective indices. Analysis and measurements were demonstrated for both intra-modal and inter-modal processes over PM fibers.

The intra-modal processes largely follow the SMF case, with phase modulation of optical probe waves propagating in either the fast or the slow axis [65]. By contrast, the inter-modal process is associated with much larger acoustic wavenumbers. Much like the photonic waveguide demonstration, the symmetry between scattering to upper and lower sidebands is removed, thus providing amplification to a single sideband. Due to the presence of strain rods in PM fibers, the radial and azimuthal symmetries of acoustic mode profiles are broken, and the transverse profiles of the acoustic modes are far more complex than those of the TR modes. Nevertheless, numerical analysis successfully predicted all F-SBS spectra [65].

The inter-modal coupling in PM fibers also gives rise to non-reciprocal propagation effects [65]: a probe wave at a certain frequency which is counter-propagating with respect to the pump fields may be scattered to a sideband at the orthogonal principal axis. Conversely, a probe wave with the same frequency that is co-propagating with the pumps is unaffected. Non-reciprocity can be induced in several probe wavelength windows using the same pumps, through a multitude of guided acoustic modes. The non-reciprocity effects in PM fibers may provide the building blocks for opto-mechanical isolators and circulators [65].

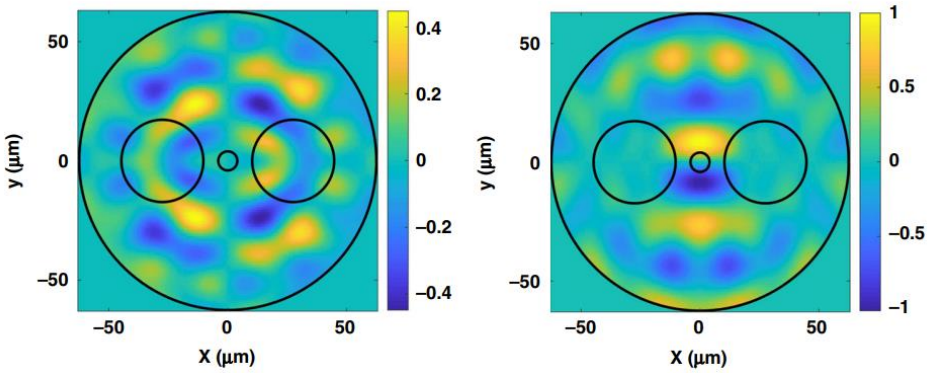

Figure 5 – Calculated normalized transverse $\hat{x}$ (left) and $\hat{y}$ (right) components of material displacement in one guided acoustic mode in a PM fiber, with a cut-off frequency of 175MHz. Black circles denote the boundaries of the cladding, strain rods, and core [65].

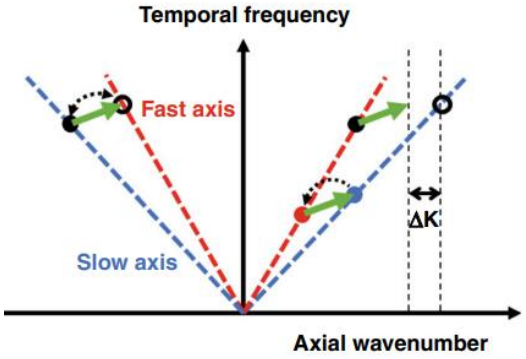

Figure 6 – Non-reciprocal cross-polarization coupling of probe waves due to inter-modal forward SBS. The acoustic wave induced by the pump fields (lower right green arrow) may scatter a counter-propagating probe wave of a specific frequency from one principal axis to the other (upper left green arrow). Cross-polarization coupling of the same probe frequency is prohibited in the forward direction (upper right green arrow) due to wavenumber mismatch, noted as Δk [65].

In 2022, Bashan proposed and demonstrated a first forward SBS fiber laser, utilizing the single-sideband amplification of the inter-modal process in PM fibers [66]. Feedback for the lasing signal was obtained by fiber Bragg gratings at both ends of the fiber, and the single-sideband amplification reached a lasing threshold. Due to the PM fiber birefringence, feedback was

provided to the lasing signal only, while the pump passed through the gratings with low residual reflections. The laser linewidth reached few kHz, limited by thermal drifting of the longitudinal cavity modes. The observed output power of the laser was 250 µW, restricted by the onset of intra-modal backward SBS lasing within the cavity [66].

The F-SBS fiber laser is sensitive to media outside the cladding boundary, even though such media does not affect the optical cavity. When the PM fiber was partially immersed in water, the opto-mechanical gain of the immersed section dropped by an order of magnitude due to larger acoustic dissipation, and a higher pump power was required to achieve the lasing threshold. Lasing was not achieved when the fiber was fully immersed in water. Such sensitivity is unique to the forward SBS mechanism. The F-SBS fiber laser may be utilized as an ultra-high coherence source and in precision sensing of media outside the cladding [66].

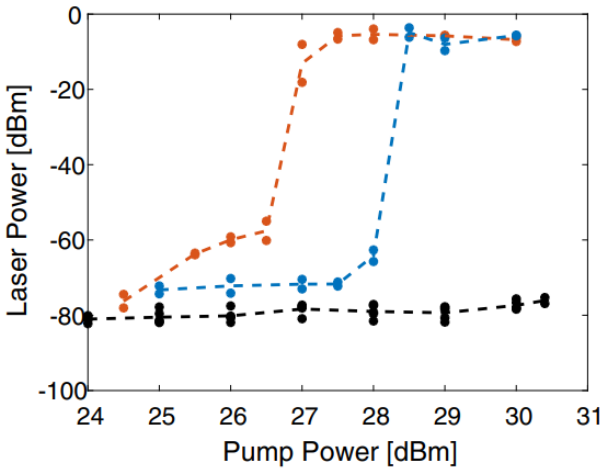

Figure 7 – Measured optical power of the F-SBS fiber laser signal as a function of the pump power. The bare fiber cavity was kept in air (red), immersed in water for 40% of its length (blue), or fully immersed in water (black). Partial immersion elevated the lasing threshold since the opto-mechanical coefficient in the immersed section is reduced by an order of magnitude. Lasing could not be reached when the fiber was wet for its entire length [66].

Inter-modal forward SBS was also demonstrated over thin fiber tapers by Xu *et al.* in 2022 [67]. A uniform-cladding fiber was tapered down to a waist diameter of 1.6 µm. The optical modes were guided by the contrast between the fiber silica and the air, and the waist diameter was selected to support the LP_{01}, LP_{11} groups only. Large overlap was achieved between the optical and acoustic modes, with both spanning the entire cross-section of the fiber taper. Accordingly, the Brillouin gain coefficients reached were unusually high, 1-2 orders of magnitude beyond those of standard fibers [67].

The acoustic modes supported by the narrow fiber tapers combine between bulk and surface terms, and they are generally more complex than the TR modes of standard fibers. TR-like modes in tapered fibers only appear at high hypersonic frequencies, beyond 1.5 GHz, and they were not stimulated in the experiment. The results provided a first example of forward Brillouin scattering among distinct spatial optical modes in uniform-cladding fibers. However, the drastic tapering restricts the fiber lengths that may be used.

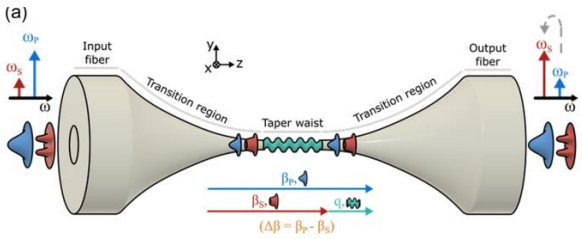

Figure 8 – Schematic illustration of an inter-modal forward SBS interaction in a narrow fiber taper [67].

1.5.3. Backward scattering in few-mode fibers

Inter-modal Brillouin scattering interactions may also take place in standard few-mode fibers, supporting the propagation of several distinct spatial optical modes. In 2013, Song *et al.* characterized and measured backward SBS interactions between the first four mode groups in a standard few-mode fiber: $LP_{01}, LP_{11}, LP_{21}$ and LP_{02} [68]. The FMF used was a uniform cladding step-index fiber at 1550 nm wavelength. A mode-division multiplexer composed of concatenated mode-selective couplers was applied for selective launching of each LP group. Both intra-modal and inter-modal processes were observed, and the Brillouin gain spectra were characterized experimentally. The spontaneous backward SBS threshold was also evaluated for each of the optical modes [68].

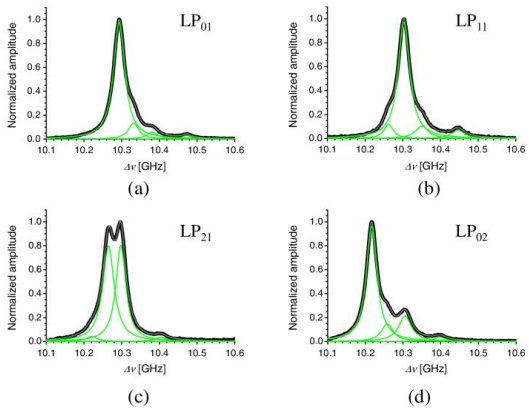

Figure 9 – Measured (black) and calculated (green) backward SBS gain spectra of intra-modal interactions in the first four LP mode groups of a few-mode fiber. Each spectrum consists of contribution of four acoustic core modes [68].

In 2021, Kim *et al.* proposed and demonstrated distributed Brillouin sensing in standard few-mode fibers [69]. The B-SBS spectra were utilized for direct measurements of polarization and modal birefringence in the fiber. Moreover, environmental variables like strain, temperature and pressure affect modal dispersion and might be extracted from the backward SBS spectra using distributed analysis protocols [69].

Thus far, Brillouin scattering in standard few-mode fibers has been demonstrated only in the backward direction. Forward SBS in standard FMFs has yet to be examined.

2. Objectives

In this thesis, I report the analysis, calculations, and experimental demonstration of forward SBS in an off-the-shelf, step-index FMF with standard, uniform cladding. The FMF supports three guided optical core modes: LP_{01}, LP_{02} and the LP_{11} group. Intra-modal and inter-modal processes were observed between the LP groups and the guided acoustic cladding modes TR_{pm}. The main novelty of the research is the following:

- Analytical formulation of the forward SBS process for arbitrary guided optical modes and guided acoustic TR modes. Both intra-modal and inter-modal processes were considered.
- Observation of higher acoustic frequencies up to 1.8 GHz in the intra-modal process through the LP_{02} mode.
- Stimulation of additional categories of TR acoustic modes: TR_{1m} and TR_{4m}. The TR_{1m} class was observed in the inter-modal process between the LP_{01} mode and the LP_{11} group, and the TR_{4m} category was observed in the intra-modal process of the LP_{11} group.
- Excitation of the R_{0m} and TR_{2m} acoustic modes above their cut-off frequencies through inter-modal process between the LP_{01} and LP_{02} modes.

The results represent the first analysis of F-SBS in an FMF, and they could not be obtained in standard SMFs. The study extends the formulation and scope of fiber opto-mechanics beyond the single-mode regime, and it may find applications in fiber lasers and sensing.

3. Theoretical analysis

3.1. Guided optical core modes in standard optical fibers

3.1.1. Guided optical core modes in step-index fibers

The optical modal solutions in step-index fibers are governed by Maxwell's equations in dielectric media. The equations may be brought to the form of the wave equation and solved in cylindrical coordinates in the core and the cladding of the fiber. For a monochromatic electric field vector propagating at an optical frequency ω, $\vec{E}(r,\phi,z,t) = \tilde{E}(r,\phi,z)\exp(-j\omega t)$, the wave equation becomes [1]:

$$\nabla^2\tilde{E} + n_{1,2}^2 k_0^2 \tilde{E} = 0 \tag{1}$$

Here, r and ϕ are the radial and azimuthal transverse coordinates, respectively, and z is the axial coordinate aligned with the fiber axis. $\tilde{E}(r,\phi,z)$ holds the spatial dependence of the electric field vector, and $n_{1,2}$ are the refractive indices of the core and the cladding, respectively. $k_0 = \omega/c$ is the vacuum wavenumber of incident light, where c is the speed of light in vacuum.

Let us denote the axial propagation constant of the electro-magnetic wave as β, and define: $h^{core} = \sqrt{n_1^2 k_0^2 - \beta^2}$ and $h^{clad} = \sqrt{\beta^2 - n_2^2 k_0^2}$. Solving the wave equation, the axial components of the electric and magnetic fields E_z, H_z in the core of the fiber are given by [1]:

$$E_z(r,\phi,z) = A_l J_l(h^{core} r)\exp(jl\phi)\exp(j\beta z)\,, \qquad r \le a \tag{2}$$

$$H_z(r,\phi,z) = B_l J_l(h^{core} r)\exp(jl\phi)\exp(j\beta z)\,, \qquad r \le a \tag{3}$$

Here, A_l and B_l are constants, $l \ge 0$ is an integer which denotes the azimuthal symmetry order of the optical field, J_l is the Bessel function of the first kind, order l, and a is the core radius.

The corresponding fields in the cladding of the fiber are given by [1]:

$$E_z(r,\phi,z) = C_l K_l\left(h^{clad} r\right)\exp(jl\phi)\exp(j\beta z)\,, \qquad r > a \tag{4}$$

$$H_z(r,\phi,z) = D_l J_l\left(h^{clad} r\right)\exp(jl\phi)\exp(j\beta z)\,, \qquad r > a \tag{5}$$

Here, C_l and D_l are also constants, and K_l represents the modified Bessel function of the second kind, order l.

The radial and azimuthal components of the electro-magnetic field are derived from the axial components. Inside the core we obtain [1]:

$$E_r = \frac{j}{(h^{core})^2}\left[\beta\frac{\partial E_z}{\partial r} + \mu_0\frac{\omega}{r}\frac{\partial H_z}{\partial \phi}\right] \tag{6}$$

$$E_\phi = \frac{j}{(h^{core})^2}\left[\frac{\beta}{r}\frac{\partial E_z}{\partial \phi} - \mu_0\omega\frac{\partial H_z}{\partial r}\right] \tag{7}$$

$$H_r = \frac{j}{(h^{core})^2}\left[\beta\frac{\partial H_z}{\partial r} - \varepsilon_0 n_1^2\frac{\omega}{r}\frac{\partial E_z}{\partial \phi}\right] \tag{8}$$

$$H_\phi = \frac{j}{(h^{core})^2}\left[\frac{\beta}{r}\frac{\partial H_z}{\partial \phi} + \varepsilon_0 n_1^2\omega\frac{\partial E_z}{\partial r}\right] \tag{9}$$

Here ε_0 and μ_0 are the vacuum permittivity and permeability, respectively. The corresponding expressions for Eqs. (6)-(9) in the cladding are identical, with $(h^{core})^2$ replaced by $-(h^{clad})^2$ and n_1 replaced by n_2.

The electro-magnetic wave propagating in the optical fiber must satisfy the boundary conditions in the core-cladding interface. It is required that all field components E_z, E_ϕ, H_z, H_ϕ tangential to the boundary interface $r = a$ are continuous at that boundary. These requirements lead to a set of four homogenous equations that must be satisfied for the coefficients A_l, B_l, C_l and D_l. The equations may be arranged in the form of a matrix:

$$\begin{pmatrix} J_l(h^{core}a) & 0 & -K_l(h^{clad}a) & 0 \\ 0 & J_l(h^{core}a) & 0 & -K_l(h^{clad}a) \\ j\dfrac{\beta l\cdot J_l(h^{core}a)}{(h^{core})^2 a} & -\dfrac{\mu_0\omega}{h^{core}}J_l'(h^{core}a) & j\dfrac{\beta l\cdot K_l(h^{clad}a)}{(h^{clad})^2 a} & -\dfrac{\mu_0\omega}{h^{clad}}K_l'(h^{clad}a) \\ \dfrac{\varepsilon_0 n_1^2\omega}{h^{core}}J_l'(h^{core}a) & j\dfrac{\beta l\cdot J_l(h^{core}a)}{(h^{core})^2 a} & \dfrac{\varepsilon_0 n_2^2\omega}{h^{clad}}K_l'(h^{clad}a) & j\dfrac{\beta l\cdot K_l(h^{clad}a)}{(h^{clad})^2 a} \end{pmatrix}\begin{pmatrix} A_l \\ B_l \\ C_l \\ D_l \end{pmatrix} = 0 \tag{10}$$

Here, J_l' and K_l' are the derivatives of the Bessel functions with respect to their arguments.

Non-trivial solutions are obtained only if the determinant of the coefficients matrix equals zero. Following that, we obtain the eigen-value equation for the electro-magnetic wave in the optical fiber [1]:

$$\left[\frac{J_l'(h^{core}a)}{h^{core}J_l(h^{core}a)}+\frac{K_l'(h^{clad}a)}{h^{clad}K_l(h^{clad}a)}\right]\cdot\left[\frac{J_l'(h^{core}a)}{h^{core}J_l(h^{core}a)}+\frac{n_2^2}{n_1^2}\frac{K_l'(h^{clad}a)}{h^{clad}K_l(h^{clad}a)}\right]$$
$$=\frac{l^2}{a^2}\left(\frac{1}{(h^{core})^2}+\frac{1}{(h^{clad})^2}\right)\cdot\left(\frac{1}{(h^{core})^2}+\frac{n_2^2}{n_1^2}\frac{1}{(h^{clad})^2}\right) \quad (11)$$

For a given azimuthal order l, the eigen-value equation leads to a discrete set of solutions for the propagation constant β. We denote the wavenumber solutions as β_{ln}, where $n \geq 1$ is the integer radial order. The solutions are arranged in descending order, where β_{l1} is the largest solution for a particular l. Substituting each β_{ln} to the electro-magnetic field components, we obtain a unique spatial profile for the optical field, which corresponds to a guided optical mode in the fiber.

The guided optical core modes supported by the fiber are denoted by HE_{ln} and EH_{ln}. In the HE_{ln} category, the axial component of the magnetic field H_z dominates the electric field E_z. The opposite is true for EH_{ln}. In Both categories the transverse components of the electro-magnetic field are much larger than the axial ones, hence E_z and H_z are often disregarded, and the optical modes are considered as nearly transverse. For $l = 0$ the modal solutions are actually purely transverse, and they are denoted as the transverse-electric modes TE_{0n} and transverse-magnetic modes TM_{0n}. Each optical mode is associated with an effective refractive index, defined as $n_{eff} = \beta_{ln}/k_0$. The effective index governs the phase velocity of the optical mode ($v_{phase} = c/n_{eff}$) and satisfies $n_2 < n_{eff} < n_1$.

When considering a weakly guided fiber ($|n_1 - n_2| \ll 1$), the eigen-value equation can be simplified to obtain the spatial transverse profiles of the optical modes and approximated propagation constants β_{ln}. In Eq. (11) we approximate $n_2^2/n_1^2 \approx 1$, leading to [62]:

$$\left[\frac{J_l'(h^{core}a)}{h^{core}J_l(h^{core}a)}+\frac{K_l'(h^{clad}a)}{h^{clad}K_l(h^{clad}a)}\right]^2=\frac{l^2}{a^2}\left(\frac{1}{(h^{core})^2}+\frac{1}{(h^{clad})^2}\right)^2 \quad (12)$$

Taking the square root of both sides, we obtain:

$$\frac{J_l'(h^{core}a)}{h^{core}J_l(h^{core}a)}+\frac{K_l'(h^{clad}a)}{h^{clad}K_l(h^{clad}a)}=\pm\frac{l}{a}\left(\frac{1}{(h^{core})^2}+\frac{1}{(h^{clad})^2}\right) \quad (13)$$

The $\pm$ sign corresponds to two different equations for the modal categories HE_{ln} and EH_{ln} respectively. Using Bessel function identities, the eigen-value equation for the HE category may be expressed as [62]:

$$\frac{J_{l-1}(h^{core}a)}{h^{core}J_l(h^{core}a)} = \frac{K_{l-1}(h^{clad}a)}{h^{clad}K_l(h^{clad}a)} \tag{14}$$

Substituting the approximate solutions β_{ln} of Eq. (14) into Eqs. (6)-(7), we find the normalized transverse profile of the electric filed vector for the HE category:

$$\vec{E}_{T,ln}^{(HE)}(r,\phi) = G_{ln}^{(HE)}(r)\left[\begin{Bmatrix}\cos(l\phi)\\ \sin(l\phi)\end{Bmatrix}\hat{\boldsymbol{r}} + \begin{Bmatrix}-\sin(l\phi)\\ \cos(l\phi)\end{Bmatrix}\hat{\boldsymbol{\phi}}\right] \tag{15}$$

Here $\hat{\boldsymbol{r}}$ and $\hat{\boldsymbol{\phi}}$ are unit vectors in the radial and azimuthal directions, respectively. The curled brackets correspond to two spatially orthogonal solutions for each mode, and $G_{ln}^{(HE)}(r)$ is the radial profile of the optical field, defined as:

$$G_{ln}^{(HE)}(r) = E_{ln}^{(HE)}\begin{cases}\dfrac{J_{l-1}(h_{ln}^{core}r)}{h_{ln}^{core}J_l(h_{ln}^{core}a)}, & r \le a\\ \dfrac{K_{l-1}(h_{ln}^{clad}r)}{h_{ln}^{clad}K_l(h_{ln}^{clad}a)}, & r > a\end{cases} \tag{16}$$

$E_{ln}^{(HE)}$ is defined so that $\iint \left|\vec{E}_{T,ln}^{(HE)}(r,\phi)\right|^2 rdrd\phi = 1$. The units of $G_{ln}^{(HE)}(r)$ and $\vec{E}_{T,ln}^{(HE)}(r,\phi)$ are m^{-1}.

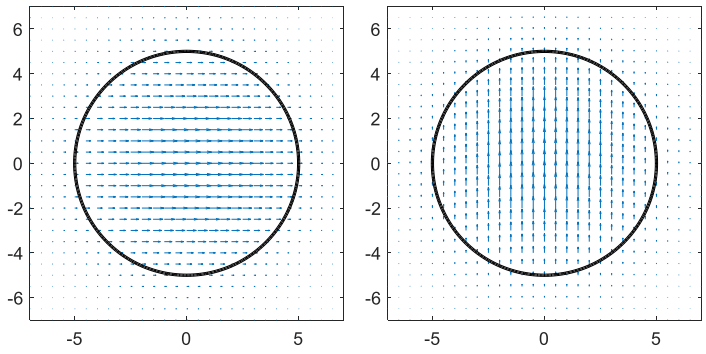

Figure 10 – Calculated transverse profiles of electric field vectors in the HE_{11} optical mode in two spatially orthogonal orientations. The arrows direction and length at each spatial point correspond to the field vector direction and magnitude, respectively.

For the EH modal category, we obtain the following equation driven from Eq. (13):

$$\frac{J_{l+1}(h^{core}a)}{h^{core}J_{l+2}(h^{core}a)} = \frac{K_{l+1}(h^{clad}a)}{h^{clad}K_{l+2}(h^{clad}a)} \tag{17}$$

Similar to HE, we obtain the normalized transverse profile of the electric filed vector:

$$\vec{E}_{T,ln}^{(EH)}(r,\phi) = G_{ln}^{(EH)}(r)\left[\begin{Bmatrix}\cos(l\phi)\\ \sin(l\phi)\end{Bmatrix}\hat{\boldsymbol{r}} + \begin{Bmatrix}\sin(l\phi)\\ -\cos(l\phi)\end{Bmatrix}\hat{\boldsymbol{\phi}}\right] \tag{18}$$

Here $G_{ln}^{(EH)}(r)$ is defined as:

$$G_{ln}^{(EH)}(r) = E_{ln}^{(EH)}\begin{cases}\dfrac{J_{l+1}(h_{ln}^{core}r)}{h_{ln}^{core}J_{l+2}(h_{ln}^{core}a)}, & r \le a\\ \dfrac{K_{l+1}(h_{ln}^{clad}r)}{h_{ln}^{clad}K_{l+2}(h_{ln}^{clad}a)}, & r > a\end{cases} \tag{19}$$

$E_{ln}^{(EH)}$ is also defined so that $\iint \left|\vec{E}_{T,ln}^{(EH)}(r,\phi)\right|^2 r dr d\phi = 1$.

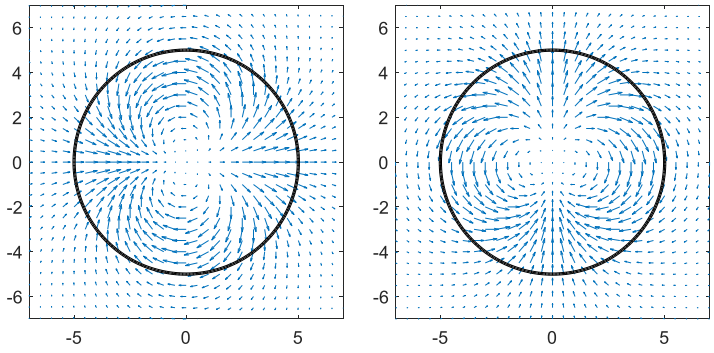

Figure 11 – Calculated transverse profiles of electric field vectors in the EH_{11} optical mode in two spatially orthogonal orientations. The arrows direction and length at each spatial point correspond to the field vector direction and magnitude, respectively.

For the specific cases of TE and TM modes, we get:

$$\vec{E}_{T,0n}^{(TE)}(r,\phi) = G_{0n}^{(HE)}(r)\hat{\boldsymbol{\phi}} \tag{20}$$

$$\vec{E}_{T,0n}^{(TM)}(r,\phi) = G_{0n}^{(EH)}(r)\hat{\boldsymbol{r}} \tag{21}$$

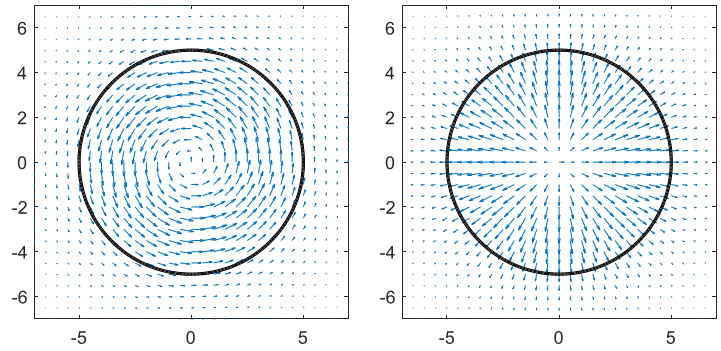

Figure 12 – Calculated transverse profiles of electric field vectors in the TE_{01} (left) and TM_{01} (right) optical modes. The arrows direction and length at each spatial point correspond to the field vector direction and magnitude, respectively.

3.1.2. The linearly polarized mode groups

Given an azimuthal order $l \geq 2$, one may notice that for the modal categories $HE_{l+1,n}$ and $EH_{l-1,n}$, Eqs. (14) and (17) become identical and take the following form:

$$\frac{J_l(h^{core}a)}{h^{core}J_{l+1}(h^{core}a)} = \frac{K_l(h^{clad}a)}{h^{clad}K_{l+1}(h^{clad}a)} \tag{22}$$

Hence, we find that in the weakly guiding approximation regime, the $HE_{l+1,n}$ and $EH_{l-1,n}$ modes are degenerate: they share the same approximated propagation constants β_{ln} and the same transverse radial profiles $G_{l+1,n}^{(HE)}(r) = G_{l-1,n}^{(EH)}(r)$. Linear combinations of these optical modes with different spatial orientations yield the following quasi-modes which exhibit linear polarization:

$$\vec{E}_{T,ln}^{(LP)}(r,\phi) = G_{ln}^{(LP)}(r)\begin{Bmatrix}\cos(l\phi)\\ \sin(l\phi)\end{Bmatrix}\hat{\boldsymbol{e}} \tag{23}$$

Here, $G_{ln}^{(LP)}(r)$ is the common transverse radial profile of the optical modes and $\hat{\boldsymbol{e}}$ is a unit vector of an arbitrary state of polarization. These quasi-modes refer to as the linearly polarized (LP) modes LP_{ln}. The LP modes are not exact modes since there is a slight difference in effective indices between the $HE_{l+1,n}$ and $EH_{l-1,n}$ modes. Nevertheless, the LP quasi-modes are often considered as mode groups. The differences in the refractive indices among modes within the same LP group are in the order of 10^{-5} refractive index units (RIU), 2-3 orders of magnitude smaller than the corresponding differences between different LP mode groups. Therefore, they are often launched and de-multiplexed collectively in SDM architectures, providing the building blocks for higher data transmission.

For azimuthal order $l = 1$, the LP_{1n} group consists of the TE_{0n}, TM_{0n} and HE_{2n} optical modes. For $l = 0$, the LP_{0n} group includes the HE_{1n} mode only, hence LP_{0n} is considered as an exact mode.

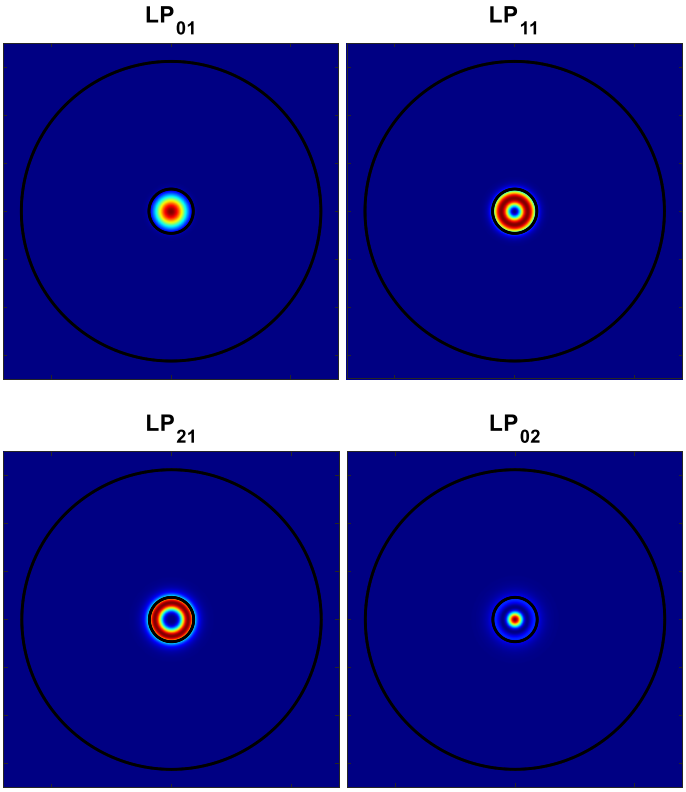

Figure 13 – Calculated normalized radial profiles of the electromagnetic intensity of the first four LP mode groups (see panels titles). Optical vacuum wavelength: λ_0 = 1550nm; Refractive indices of core and cladding, respectively: n_1 = 1.463, n_2 = 1.458; Core and cladding diameters, respectively: $2a$ = 18.5μm, $2b$ = 125μm (V = 4.53).

The number of LP mode groups supported by the optical fiber is governed by the V parameter:

$$V = k_0 a \sqrt{n_1^2 - n_2^2} \tag{24}$$

Figure 14 illustrates the effective refractive indices of multiple guided LP mode groups as functions of the V parameter. For $V \leq 2.405$, only the fundamental mode LP_{01} (or HE_{11}) is allowed to propagate in the fiber, and the fiber is referred to as an SMF. As the V parameter is increased, more and more LP groups are able to propagate in the optical fiber, entering the few-mode regime.

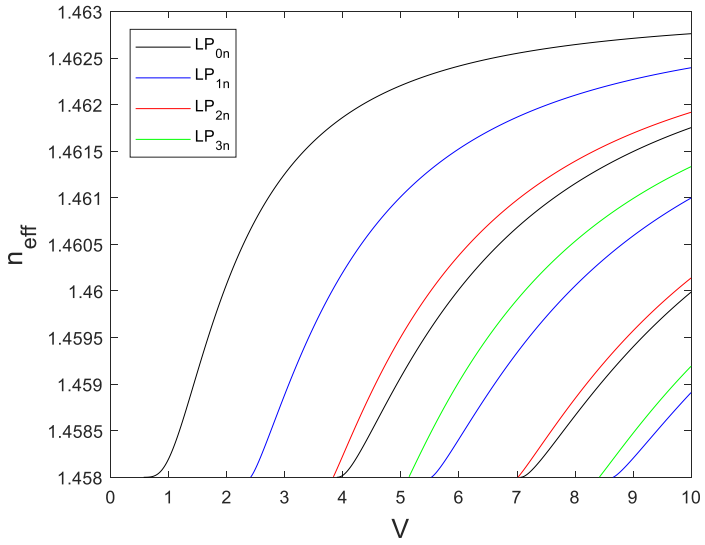

Figure 14 – Calculated effective refractive indices n_{eff} of multiple guided optical mode groups in a standard fiber as a function of the V parameter. The core and cladding refractive indices are chosen n_1 = 1.463 and n_2 = 1.458, respectively.

3.2. Guided acoustic cladding modes in optical fibers

3.2.1. Basic definitions

In the following section we define the terms and variables associated with guided acoustic modes in optical fibers:

- $\vec{U} = \left(U_x, U_y, U_z\right)^T$ – The material displacement vector [m] in Cartesian coordinates x, y, z.
- $\boldsymbol{S}$ – The second-order strain tensor [unit-less].

The strain is obtained by the tensor gradient of the displacement:

$$\boldsymbol{S} = \boldsymbol{\nabla}\vec{U} \tag{25}$$

In Cartesian coordinates, the strain elements are given by:

$$S_{ij} = \frac{\partial U_i}{\partial j} \tag{26}$$

Where $i, j \in \{x, y, z\}$.

We often use the symmetric form of the strain tensor, with elements given by:

$$S_{ij} = \frac{1}{2}\left(\frac{\partial U_i}{\partial j} + \frac{\partial U_j}{\partial i}\right) \tag{27}$$

- $\boldsymbol{T}$ – The second-order stress tensor [N×m^{-2}].

For purely elastic materials, the relation between the second-order stress and strain tensors is given by the fourth-order stiffness tensor $\boldsymbol{c}$ [N×m^{-2}]:

$$\boldsymbol{T} = \boldsymbol{c} : \boldsymbol{S} \tag{28}$$

With elements:

$$T_{ij} = \sum_{k,l} c_{ijkl} S_{kl} \tag{29}$$

Here k, l also scan over $\{x, y, z\}$.

- $\boldsymbol{p}$ – The fourth-order photo-elastic tensor [unit-less].

For non-birefringent materials, the second-order dielectric perturbation tensor $\Delta\boldsymbol{\varepsilon}$ associated with material strain is governed by:

$$\Delta\boldsymbol{\varepsilon} = -n_0^4\, \boldsymbol{p} : \boldsymbol{S} \tag{30}$$

With elements:

$$\Delta\varepsilon_{ij} = -n_0^4 \sum_{k,l} p_{ijkl} S_{kl} \tag{31}$$

Here n_0 is the medium refractive index.

3.2.2. The torsional-radial acoustic cladding modes

The material displacements of guided acoustic modes in optical fibers are governed by the elastic wave equation. For a lossless medium, the homogeneous equation is expressed by [34]:

$$\frac{\partial^2 \vec{U}}{\partial t^2} - v_S^2 \nabla^2 \vec{U} - (v_L^2 - v_S^2)\nabla\left(\nabla \cdot \vec{U}\right) = 0 \tag{32}$$

Here $v_{L,S}$ are the velocities of dilatational and shear acoustic waves in silica, respectively. Since cladding acoustic modes are considered, we disregard the difference in refractive indices between the core and the cladding and solve the equation for a uniform silica cylinder.

The material displacement $\vec{U}$ propagates along the fiber axis as a wave, with axial wavenumber K and temporal frequency Ω. Solving Eq. (32), the vector components of the displacement in cylindrical coordinates are given by [70,71]:

$$U_r = \left[Ak_{tl}J_p'(k_{tl}r) + jKBJ_p'(k_{ts}r) + \frac{p}{r}CJ_p(k_{ts}r)\right]\begin{Bmatrix}\cos(p\phi)\\ \sin(p\phi)\end{Bmatrix}\exp(jKz - j\Omega t) \tag{33}$$

$$U_\phi = \left[\frac{p}{r}AJ_p(k_{tl}r) + \frac{jKp}{k_{ts}r}BJ_p(k_{ts}r) + k_{ts}CJ_p'(k_{ts}r)\right]\begin{Bmatrix}-\sin(p\phi)\\ \cos(p\phi)\end{Bmatrix}\exp(jKz - j\Omega t) \tag{34}$$

$$U_z = \left[jKAJ_p(k_{tl}r) - k_{ts}BJ_p(k_{ts}r)\right]\begin{Bmatrix}\cos(p\phi)\\ \sin(p\phi)\end{Bmatrix}\exp(jKz - j\Omega t) \tag{35}$$

In Eqs. (33)-(35) $p \geq 0$ is the integer azimuthal symmetry order of the acoustic wave, k_{tl} and k_{ts} are the transverse components of the wave vector describing dilatational and shear movement, respectively, and A, B and C are constant coefficients. Note that the displacement profile exhibits two spatially orthogonal solutions, represented in curled brackets.

The wave vector components k_{tl}, k_{ts}, K and the acoustic frequency Ω satisfy the following dispersion relations [70-72]:

$$k_{tl}^2 + K^2 = \frac{\Omega^2}{v_L^2} \quad ; \quad k_{ts}^2 + K^2 = \frac{\Omega^2}{v_S^2} \tag{36}$$

The boundary conditions of a free infinite cylinder in air require zero stress in all directions at the outer surface of the cladding $r = b$:

$$T_{rr}(r = b^-) = 0 \quad ; \quad T_{rz}(r = b^-) = 0 \quad ; \quad T_{r\phi}(r = b^-) = 0 \tag{37}$$

Here b is the radius of the fiber cladding. The boundary equations may be rearranged in terms of a 3×3 matrix [11,70-72]:

$$\boldsymbol{M}_p\begin{pmatrix}A\\ B\\ C\end{pmatrix} = 0 \tag{38}$$

$$\boldsymbol{M}_p = \begin{pmatrix} -c_{12}(k_{tl}^2 + K^2)J_p(k_{tl}b) + 2c_{44}k_{tl}^2 J_p''(k_{tl}b) & -2jc_{44}K \cdot k_{ts}J_p''(k_{ts}b) & \frac{2(c_{12}+c_{44})p}{b}k_{ts}J_p'(k_{ts}b) - \frac{2c_{44}p}{b^2}J_p(k_{ts}b) \\ 2jK \cdot k_{tl}J_p'(k_{tl}b) & (k_{ts}^2 - K^2)J_p'(k_{ts}b) & -\frac{jKp}{b}J_p(k_{ts}b) \\ \frac{2p}{b}\left[k_{tl}J_p'(k_{tl}b) - \frac{1}{b}J_p(k_{tl}b)\right] & -\frac{2jKp}{k_{ts}b}\left[k_{ts}J_p'(k_{ts}b) - \frac{1}{b}J_p(k_{ts}b)\right] & \frac{p^2}{b^2}J_p(k_{ts}b) + k_{ts}^2 J_p''(k_{ts}b) - \frac{k_{ts}}{b}J_p'(k_{ts}b) \end{pmatrix} \quad (39)$$

Here J_p'' denotes the second derivative of the Bessel function with respect to its arguments, and c_{12}, c_{44} are components of the stiffness tensor $\boldsymbol{c}$. Non-trivial solutions to the boundary equations are obtained when the determinant of the matrix $\boldsymbol{M}_p$ equals zero:

$$\det(\boldsymbol{M}_p) = 0 \quad (40)$$

For a given azimuthal symmetry p, every choice of axial wavenumber K leads to a discrete set of acoustic frequencies Ω that satisfy Eq. (40). Each Ω is associated with a unique spatial profile of the material displacement, corresponding to several acoustic modes guided by the fiber cladding. These modes are referred to as the torsional-radial (TR) acoustic cladding modes TR_{pm}, where $m \geq 1$ denotes the integer radial order. Scanning the K axis and solving Eq. (40) for Ω, we obtain the dispersion curves of the TR_{pm} modes. Each curve is characterized by a cut-off frequency, obtained by substituting $K = 0$ into the boundary conditions equations. These cut-off frequencies are denoted as Ω_{pm}. Below cut-off, the acoustic modes may no longer propagate in the axial direction.

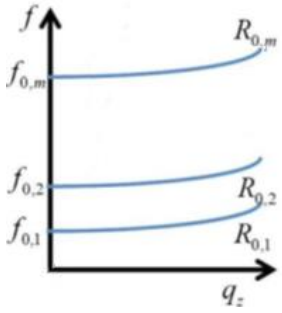

Figure 15 – Schematic illustation of dispersion curves of the radial guided acoustic modes R_{0m}. The axial wavenumber is denoted q_z, and the modal cut-off frequencies are denoted $f_{0,m}$ [36].

When considering acoustic modes excited through forward SBS, the electro-strictive driving force in both intra-modal and inter modal processes exhibits axial wavenumbers which are much smaller than the transverse wavenumbers of the acoustic modes, $K \ll k_{tl}, k_{ts}$. Therefore, we assume that the acoustic modes are excited very close to their cut-offs $(\Omega \to \Omega_{pm}, K \to 0)$. At that limit, the phase velocities of the guided acoustic modes approach infinity, and the material displacement vectors become predominantly transverse $(U_z \ll U_r, U_\phi)$.

Following that, we substitute $K = 0$, $B = 0$ in Eqs. (38)-(40). The boundary equations are then reduced to the determinant of a 2×2 matrix [11,71,72]:

$$\begin{vmatrix} p^2 - 1 - \frac{1}{2}\Psi^2 & 2(p^2-1)\left[\Theta_p(\Psi) - p\right] - \Psi^2 \\ \Theta_{\mathrm{p}}(\Phi) - p - 1 & 2p^2 - 2\left[\Theta_p(\Psi) - p\right] - \Psi^2 \end{vmatrix} = 0 \tag{41}$$

$$\Psi = \frac{\Omega_{pm} b}{v_L}; \Phi = \frac{\Omega_{pm} b}{v_S}; \Theta_{\mathrm{p}}(\xi) = \frac{\xi J_{p-1}(\xi)}{J_p(\xi)} \tag{42}$$

Solving Eq. (41), we obtain the modal cut-off frequencies Ω_{pm}. Substituting into Eqs. (33)-(34), we obtain the normalized transverse displacement profiles of the TR acoustic modes:

$$\begin{aligned} \vec{u}_{pm}(r,\phi) = D_{pm}\left[A_{pm}\frac{\Omega_{pm}}{v_L}J_p'\left(\frac{\Omega_{pm}}{v_L}r\right) + \frac{p}{r}C_{pm}J_p\left(\frac{\Omega_{pm}}{v_S}r\right)\right]\begin{Bmatrix}\cos(p\phi)\\ \sin(p\phi)\end{Bmatrix}\hat{\boldsymbol{r}} \\ + \; D_{pm}\left[\frac{p}{r}A_{pm}J_p\left(\frac{\Omega_{pm}}{v_L}r\right) + C_{pm}\frac{\Omega_{pm}}{v_S}J_p'\left(\frac{\Omega_{pm}}{v_S}r\right)\right]\begin{Bmatrix}-\sin(p\phi)\\ \cos(p\phi)\end{Bmatrix}\hat{\boldsymbol{\phi}} \end{aligned} \tag{43}$$

Here, A_{pm} and C_{pm} are the two elements of the eigen-vectors corresponding to the cut-off frequency eigen-values Ω_{pm} of Eq. (41). D_{pm} is a normalization factor, defined so that $\int_0^{2\pi}\int_0^b \left|\vec{u}_{pm}(r,\phi)\right|^2 r\mathrm{d}r\,\mathrm{d}\phi = 1$. Therefore, $\vec{u}_{pm}$ has units of m^{-1}.

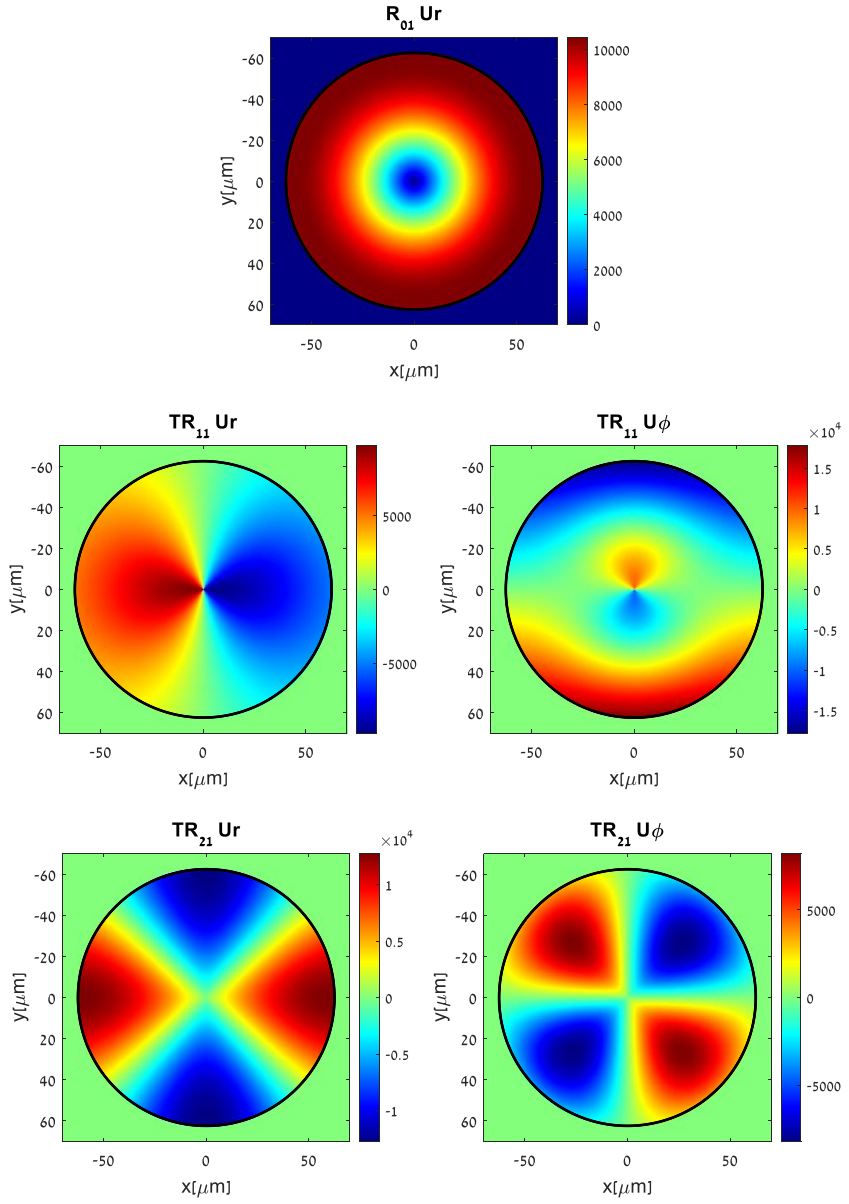

Figure 16 – Normalized calculated transverse profiles of material displacement of several guided acoustic cladding modes. Top: radial displacement in mode R_{01}. Center: radial (left) and azimuthal (right) displacement in mode TR_{11}. Bottom: radial (left) and azimuthal (right) displacement in mode TR_{21}.

3.2.3. Classification of the torsional-radial modes

The radial and azimuthal components of the normalized displacement in Eq. (43) consist of two terms each. The first term in each pair describes dilatational wave motion, governed by velocity v_L, whereas the second term in each pair represents shear wave motion with velocity v_S [56]. Every TR_{pm} mode with $p \geq 1$ includes nonzero contributions of both types of waves. The relative magnitudes of the two contributions are proportional to A_{pm}, C_{pm}. TR modes may be broadly classified as either predominantly dilatational, (where $A_{pm} \gg C_{pm}$), or shear-like, in cases where

$C_{pm} \gg A_{pm}$ [44,45,56]. For $p = 0$, the radial modes R_{0m} are purely dilatational, whereas the torsional modes T_{0m} are strictly shear waves.

The spacing between the cut-off frequencies Ω_{pm} of TR modes that are primarily dilatational is approximately $v_L/(2b)$, and the corresponding spacing for shear-like modes equals approximately $v_S/(2b)$ [44,45]. While the classification of modes as either dilatational or shear-like is not complete, and the above frequency spacings are not precise, they are nevertheless useful in the study of forward Brillouin scattering processes.

3.2.4. Dispersion relations of the torsional-radial modes

As discussed in previous section, each guided acoustic mode is characterized by a dispersion curve between the acoustic frequency Ω and axial wavenumber K. The curve is governed by either one of the dispersion relations of Eq. (36), depending on whether the acoustic mode is predominantly dilatational or shear-like. In cut-off, $K = 0$, therefore we obtain:

$$k_{tl} = \frac{\Omega_{pm}}{v_L} \quad ; \quad k_{ts} = \frac{\Omega_{pm}}{v_S} \tag{44}$$

Substituting back in Eq. (36), we obtain the following dispersion relations close to cut-off:

$$\Omega - \Omega_{pm} \approx \frac{v_{L,S}^2}{2\Omega_{pm}} K^2 \tag{45}$$

In intra-modal F-SBS interactions, the axial wavenumber K is very small, typically in the order of 1-10 rad×m^{-1}. Therefore, in these processes the acoustic modes are excited practically at their cut-offs $\Omega = \Omega_{pm}$. By contrast, in inter-modal interactions K may reach the order of 10^4 rad×m^{-1}. These values may be within a single order of magnitude of the transverse wavenumbers k_{tl}, k_{ts}. Following Eq. (45), the acoustic modes might be stimulated at frequencies detuned from the cut-offs by several MHz.

3.3. The driving force: electro-striction

3.3.1. Derivation of the driving force

Consider two co-propagating optical fields of frequencies $\omega_{1,2} = \omega_{\mathrm{p}} \pm \frac{1}{2}\Omega$, in spatial optical modes 1 and 2, respectively:

$$\vec{E}_{1,2}(x,y,z,t) = A_{1,2}(z)\vec{E}_{T,1,2}(x,y)\exp\left(j\beta_{1,2}z - j\omega_{1,2}t\right) + c.c \tag{46}$$

Here ω_p is a central optical frequency, Ω denotes a frequency detuning on the acoustic scale, and $A_{1,2}(z)$ represent scalar complex magnitudes in Volts. $\beta_{1,2}$ and $\vec{E}_{T,1,2}$ are the propagation constants and normalized transverse profiles of the two optical waves, according to their specific modes. We denote these optical fields as two pump waves.

The two fields induce mechanical stress in the optical fiber, pulling the medium particle towards higher intensity regions. The second-order electro-strictive stress tensor $\boldsymbol{\sigma}_{1,2}$ [N×m^{-2}] associated with the two pumps includes components which propagate along the fiber as a wave, with temporal frequency Ω and axial wavenumber $K = \beta_1 - \beta_2$. The tensor components are given by [11]:

$$\sigma_{ij,1,2}(x,y,z,t) = -\frac{1}{2}\varepsilon_0 n_0^4\left[\sum_{k,l} p_{ijkl}A_1(z)A_2^*(z)E_{k1}(x,y)E_{l2}(x,y)\right]\exp(jKz - j\Omega t) + c.c \tag{47}$$

Here, i,j,k,l scan over the Cartesian coordinates x,y,z, E_{k1} and E_{l2} are the vector components of the electric fields' transverse profiles, and n_0 is the refractive index of silica. As will be discussed in more detail later, the electro-strictive forces per unit volume associated with the pump waves are given be spatial derivatives of $\boldsymbol{\sigma}_{1,2}$. in settings of F-SBS K is comparatively small, and axial derivatives of Eq. (47) are much smaller than transverse ones. In addition, the optical fields are restricted to the transverse plane as well. We therefore restrict $i,j,k,l \in \{x,y\}$ only from now on.

We rearrange Eq. (47) and obtain:

$$\sigma_{ij,1,2}(x,y,z,t) = -\frac{1}{4n_0 c}n_0^4\left[\sum_{k,l} p_{ijkl}E_{k1}(x,y)E_{l2}(x,y)\right]P(\Omega,z)\exp(jKz - j\Omega t) + c.c \tag{48}$$

Here, $P(\Omega, z) = 2n_0 c\varepsilon_0 A_1(z)A_2^*(z)$ [Watts] refers to the beating power between the pump waves.

We define the tensor $\boldsymbol{I}_{1,2}$ [m^{-2}] of cross-products between the normalized field components:

$$I_{ij,1,2} = E_{i1}E_{j2} \tag{49}$$

Substituting into Eq. (48) yields:

$$\sigma_{ij,1,2} = -\frac{1}{4n_0 c} n_0^4 \left[\sum_{k,l} p_{ijkl} I_{kl,1,2}\right] P(\Omega, z)\exp(jKz - j\Omega t) + c.c \tag{50}$$

We define the normalized transverse stress tensor $\tilde{\boldsymbol{\sigma}}_{1,2}$ [m^{-2}]:

$$\tilde{\boldsymbol{\sigma}}_{1,2} = -n_0^4\, \boldsymbol{p} : \boldsymbol{I}_{1,2} \tag{51}$$

With elements:

$$\tilde{\sigma}_{ij,1,2} = -n_0^4 \sum_{k,l} p_{ijkl} I_{kl,1,2} \tag{52}$$

We may write:

$$\boldsymbol{\sigma}_{1,2}(x, y, z, t) = \frac{1}{4n_0 c}\tilde{\boldsymbol{\sigma}}_{1,2}(x, y)P(\Omega, z)\exp(jKz - j\Omega t) + c.c \tag{53}$$

Here the normalized stress tensor $\tilde{\boldsymbol{\sigma}}_{1,2}(x, y)$ contains the transverse dependence of $\boldsymbol{\sigma}_{1,2}$. The electro-strictive force per unit volume [N×m^{-3}] driven by the two optical fields is given by the tensor divergence of the stress [73]:

$$\vec{F}_{1,2} = -\boldsymbol{\nabla} \cdot \boldsymbol{\sigma}_{1,2} \tag{54}$$

With elements:

$$F_{i,1,2} = -\sum_j \frac{\partial}{\partial j}\sigma_{ij,1,2} \tag{55}$$

Similarly, we define the normalized transverse profile of the electro-strictive force [m^{-3}]:

$$\vec{f}_{1,2} = -\boldsymbol{\nabla} \cdot \tilde{\boldsymbol{\sigma}}_{1,2} \tag{56}$$

With elements:

$$f_{i,1,2} = -\sum_j \frac{\partial}{\partial j}\tilde{\sigma}_{ij,1,2} \tag{57}$$

We therefore may write:

$$\vec{F}_{1,2}(x,y,z,t) = \frac{1}{4n_0 c}\vec{f}_{1,2}(x,y)P(\Omega,z)\exp(jKz - j\Omega t) + c.c \tag{58}$$

We may express the components of the normalized transverse stress tensor $\tilde{\boldsymbol{\sigma}}_{1,2}$ in Eq. (52) explicitly in terms of 3×1 vectors and a 3×3 matrix. In cylindrical coordinates, we obtain [11]:

$$\begin{pmatrix} \tilde{\sigma}_{rr,1,2}(r,\phi) \\ \tilde{\sigma}_{\phi\phi,1,2}(r,\phi) \\ \tilde{\sigma}_{r\phi,1,2}(r,\phi) \end{pmatrix} = -n_0^4 \begin{pmatrix} p_{11} & p_{12} & 0 \\ p_{12} & p_{11} & 0 \\ 0 & 0 & p_{44} \end{pmatrix} \begin{pmatrix} E_{r1}(r,\phi)E_{r2}(r,\phi) \\ E_{\phi 1}(r,\phi)E_{\phi 2}(r,\phi) \\ E_{r1}(r,\phi)E_{\phi 2}(r,\phi) + E_{\phi 1}(r,\phi)E_{r2}(r,\phi) \end{pmatrix} \tag{59}$$

The formalism invokes the symmetries of the photoelastic tensor in isotropic media such as silica. Here $p_{11} \equiv p_{1111}, p_{12} \equiv p_{1122}$, $p_{44} = \frac{1}{2}(p_{11} - p_{12})$, and $E_{r,1,2}$, $E_{\phi,1,2}$ refer to the radial and azimuthal components of the normalized transverse profiles of the electric fields, respectively.

The normalized electro-strictive driving force is expressed in cylindrical coordinates as [73]:

$$\begin{aligned} \vec{f}_{1,2}(r,\phi) = &-\left[\frac{\partial\tilde{\sigma}_{rr,1,2}}{\partial r} + \frac{1}{r}\frac{\partial\tilde{\sigma}_{r\phi,1,2}}{\partial\phi} + \frac{1}{r}\left(\tilde{\sigma}_{rr,1,2} - \tilde{\sigma}_{\phi\phi,1,2}\right)\right]\hat{\boldsymbol{r}} \\ &-\left[\frac{\partial\tilde{\sigma}_{r\phi,1,2}}{\partial r} + \frac{1}{r}\frac{\partial\tilde{\sigma}_{\phi\phi,1,2}}{\partial\phi} + \frac{2}{r}\tilde{\sigma}_{r\phi,1,2}\right]\hat{\boldsymbol{\phi}} \end{aligned} \tag{60}$$

Examination of Eqs. (59)-(60) reveals that for a given choice of optical modes with azimuthal orders $l_{1,2}$ respectively, the driving force includes terms with azimuthal symmetries $l_1 \pm l_2$ only. For example, when both optical waves are guided in the fundamental mode HE_{11} ($l_{1,2} = 1$), the electro-strictive force per unit volume consists of a radially symmetric term and a term of two-fold azimuthal symmetry. By contrast, if the optical fields 1 and 2 propagate in arbitrary high-order modes, the electro-strictive force may take up any integer azimuthal order.

3.3.2. Wavenumbers of driving forces

The axial wavenumber K of the electro-strictive force per unit volume varies considerably between intra-modal and inter-modal processes. In the intra-modal case, where both pumps are guided in the same optical mode, we obtain:

$$K_{intra} = \frac{n_{\mathrm{eff},1}\left(\omega_{\mathrm{p}} + \frac{1}{2}\Omega\right)}{c} - \frac{n_{\mathrm{eff},1}\left(\omega_{\mathrm{p}} - \frac{1}{2}\Omega\right)}{c} = \frac{n_{\mathrm{eff},1}\Omega}{c} \tag{61}$$

Here $n_{\mathrm{eff},1}$ is the effective index of the common optical mode. The wavenumber in Eq. (61) is very small, typically in the order of 1-10 rad×m^{-1}, and the corresponding driving force may excite acoustic modes very close to their cut-offs as discussed before in section 3.2.4. By contrast, in inter-modal interactions, where the two pumps propagate in different spatial modes, we find that:

$$K_{inter} = \frac{n_{\mathrm{eff},1}\left(\omega_{\mathrm{p}} + \frac{1}{2}\Omega\right)}{c} - \frac{n_{\mathrm{eff},2}\left(\omega_{\mathrm{p}} - \frac{1}{2}\Omega\right)}{c} = \frac{\left(n_{\mathrm{eff},1} - n_{\mathrm{eff},2}\right)\omega_{\mathrm{p}}}{c} + \frac{n_{\mathrm{eff},1} + n_{\mathrm{eff},2}}{2}\frac{\Omega}{c} \tag{62}$$

Here $n_{\mathrm{eff},2}$ is the effective index of optical mode 2. Since $\omega_{\mathrm{p}} \gg \Omega$, we may approximate:

$$K_{inter} \approx \frac{\left(n_{\mathrm{eff},1} - n_{\mathrm{eff},2}\right)\omega_{\mathrm{p}}}{c} \tag{63}$$

The difference in effective indices between mode groups may reach the second decimal point. Hence, the axial wavenumber of the electro-strictive force driven by two distinct mode groups can be in the order of 10^4 rad×m^{-1}. This wavenumber is way larger than the intra-modal one. The large differences in wavenumbers between intra-modal vs. inter-modal scattering manifest in the forward Brillouin spectra of the two settings, as discussed in later sections.

3.3.3. Excitation of acoustic modes with arbitrary azimuthal orders

The material displacement driven by the electro-strictive force in the fiber is governed by the non-homogeneous elastic wave equation [34]:

$$\rho_0\left[\frac{\partial^2\vec{U}}{\partial t^2} + \Gamma(\Omega)\frac{\partial\vec{U}}{\partial t} - v_S^2\nabla^2\vec{U} - (v_L^2 - v_S^2)\nabla\left(\nabla\cdot\vec{U}\right)\right] = \vec{F}_{1,2} \tag{64}$$

Here ρ_0 is the material density of silica and $\Gamma(\Omega)$ represents acoustic dissipation. The electro-strictive force may stimulate guided acoustic TR modes very close to their cut-offs, propagating along the fiber hand-in-hand with the driving force at wavenumber K and acoustic frequency Ω. Each mode is associated with a modal magnitude $b_{pm}(\Omega, z)$ which depends on the acoustic frequency and axial position. The total displacement vector may be expressed in the basis of all the TR modes:

$$\vec{U}(r,\phi,z,t) = \left[\sum_{p,m} b_{pm}(\Omega,z)\,\vec{u}_{pm}(r,\phi)\right]\exp(jKz - j\Omega t) + c.c \tag{65}$$

Substituting Eqs. (58), (65) into Eq. (64) yields:

$$\sum_{p,m} b_{pm}(\Omega,z)\left[-\Omega^2 - j\Omega\Gamma(\Omega) + \Omega_{pm}^2\right]\vec{u}_{pm}(r,\phi) = \frac{1}{4n_0 c\rho_0}\vec{f}_{1,2}(r,\phi)P(\Omega,z) \tag{66}$$

We multiply both sides by the transverse displacement profile $\vec{u}_{pm}(r,\phi)$ and integrate both sides of Eq. (66) over the transverse plane. We obtain:

$$b_{pm}(\Omega,z) = \frac{1}{4n_0 c\rho_0}\frac{1}{\Omega_{pm}^2 - \Omega^2 - j\Omega\Gamma(\Omega)}P(\Omega,z)\int_0^{2\pi}\int_0^{b}\vec{u}_{pm}(r,\phi)\cdot\vec{f}_{1,2}(r,\phi)rdrd\phi \tag{67}$$

We assume that $\Gamma(\Omega) \ll \Omega_{pm}$. Therefore, we omit the frequency dependence of Γ within the frequency range of each acoustic mode and replace it by a modal constant value Γ_{pm} which represents the decay rate and spectral linewidth of that acoustic mode. We approximate the frequency response of Eq. (67) by a Lorentzian line shape:

$$\frac{1}{\Omega_{pm}^2 - \Omega^2 - j\Omega\Gamma(\Omega)} \approx \frac{j}{\Gamma_{pm}\Omega_{pm}}\frac{1}{1 - 2j\dfrac{\Omega - \Omega_{pm}}{\Gamma_{pm}}} \tag{68}$$

We now define the spatial overlap integral between the transverse profiles of the electro-strictive force driven by optical modes 1,2 and the acoustic mode displacement:

$$Q_{1,2,pm}^{(ES)} = \int_0^{2\pi}\int_0^{b}\vec{u}_{pm}(r,\phi)\cdot\vec{f}_{1,2}(r,\phi)rdrd\phi \tag{69}$$

Substituting Eqs. (68), (69) back into Eq. (67) yields:

$$b_{pm}(\Omega,z) = j\frac{Q_{1,2,pm}^{(ES)}}{4n_0 c\rho_0\Gamma_{pm}\Omega_{pm}}\frac{1}{1 - 2j\dfrac{\Omega - \Omega_{pm}}{\Gamma_{pm}}}P(\Omega,z) \tag{70}$$

The spatial overlap integral $Q_{1,2,pm}^{(ES)}$ depends on the choices of the optical modes 1 and 2 and of the acoustic mode TR_{pm}. The overlap vanishes when the azimuthal orders of $\vec{u}_{pm}$ and $\vec{f}_{1,2}$ do not match. Consequently, the azimuthal order p of the stimulated acoustic mode must equal $l_1 \pm l_2$.

Referring again to the specific case of two optical fields in the fundamental mode in which $l_{1,2} = 1$, we find that only acoustic modes with $p = 0, 2$ may be excited through forward Brillouin interactions: R_{0m}, T_{0m}, or TR_{2m}. Further, the azimuthally independent component of $\vec{f}_{1,1}$ in single-mode fibers is entirely in the $\hat{\boldsymbol{r}}$ direction. Therefore the R_{0m} acoustic modes are observed in forward Brillouin scattering in single-mode fibers, but the T_{0m} are not.

By contrast, forward Brillouin interactions in few-mode fibers, with one or both optical fields propagating in optical modes with $l \neq 1$, may result in the stimulation of additional classes of guided acoustic modes with different azimuthal symmetries. For example, the $LP_{1,1}$ group contains modes with $l = 0$ and $l = 2$. Electro-strictive stimulation through modes within that group may generate acoustic waves with azimuthal order $p = 0, 2, 4$. Inter-modal interactions between optical fields in the $LP_{0,1}$ mode and the $LP_{1,1}$ group might stimulate acoustic modes with $p = 1$ or $p = 3$.

3.4. Scattering of light by acoustic waves: photoelasticity

3.4.1. Derivation of the dielectric perturbation tensor

Consider a stimulated guided acoustic mode TR_{pm} with material displacement $\vec{U}_{pm}$:

$$\vec{U}_{pm}(r, \phi, z, t) = b_{pm}(\Omega, z)\vec{u}_{pm}(r, \phi)\exp(jKz - j\Omega t) + c.c \tag{71}$$

The displacement is associated with a symmetric strain tensor, given by:

$$\boldsymbol{S}_{pm}(r, \phi, z, t) = b_{pm}(\Omega, z)\boldsymbol{s}_{pm}(r, \phi)\exp(jKz - j\Omega t) + c.c \tag{72}$$

Here, $\boldsymbol{s}_{pm}(r, \phi)$ is the normalized symmetric strain tensor, in units of m^{-2}. Following Eq. (25), the elements of the normalized strain tensor in cylindrical coordinates are given by:

$$s_{rr,pm}(r, \phi) = \frac{\partial u_{r,pm}(r, \phi)}{\partial r} \tag{73}$$

$$s_{\phi\phi,pm}(r, \phi) = \frac{u_{r,pm}(r, \phi)}{r} + \frac{1}{r}\frac{\partial u_{\phi,pm}(r, \phi)}{\partial \phi} \tag{74}$$

$$s_{r\phi,pm}(r, \phi) = \frac{1}{2}\left(\frac{1}{r}\frac{\partial u_{r,pm}(r, \phi)}{\partial \phi} + \frac{\partial u_{\phi,pm}(r, \phi)}{\partial r} - \frac{u_{\phi,pm}(r, \phi)}{r}\right) \tag{75}$$

In Eqs. (73)-(75), $u_{r,pm}$ and $u_{\phi,pm}$ denote the radial and azimuthal components of the normalized displacement vector, respectively (see Eq. (43)). Strain in the fiber medium gives rise to photo-elastic perturbations to the dielectric tensor [11]:

$$\Delta\boldsymbol{\varepsilon}_{pm}(r,\phi,z,t) = b_{pm}(\Omega,z)\boldsymbol{\mu}_{pm}(r,\phi)\exp(jKz - j\Omega t) + c.c \tag{76}$$

Here $\boldsymbol{\mu}_{pm}(r,\phi)$ is the normalized dielectric perturbation tensor, in units of m^{-2}. The tensor $\Delta\boldsymbol{\varepsilon}_{pm}$ propagates along the fiber as a wave of frequency Ω and wavenumber K. The perturbations scale with the modal displacement magnitude $b_{pm}(\Omega,z)$, and hence also with the beating power between the two stimulating optical fields, $P(\Omega,z)$.

Following Eq. (31), the elements of the normalized dielectric tensor $\boldsymbol{\mu}_{pm}$ in Cartesian coordinates are given by:

$$\mu_{ij,pm} = -n_0^4 \sum_{k,l} p_{ijkl} s_{kl,pm} \tag{77}$$

We may express the components of $\boldsymbol{\mu}_{pm}(r,\phi)$ explicitly in terms of 3×1 vectors and a 3×3 matrix. In cylindrical coordinates, we obtain [11]:

$$\begin{pmatrix} \mu_{rr,pm}(r,\phi) \\ \mu_{\phi\phi,pm}(r,\phi) \\ \mu_{r\phi,pm}(r,\phi) \end{pmatrix} = -n_0^4 \begin{pmatrix} p_{11} & p_{12} & 0 \\ p_{12} & p_{11} & 0 \\ 0 & 0 & p_{44} \end{pmatrix} \begin{pmatrix} s_{rr,pm}(r,\phi) \\ s_{\phi\phi,pm}(r,\phi) \\ 2s_{r\phi,pm}(r,\phi) \end{pmatrix} \tag{78}$$

3.4.2. Photoelastic coupling between optical and acoustic waves

The dielectric perturbations induced by the acoustic wave may couple light between a pair of optical fields, $\vec{E}_{3,4}$, propagating in optical modes 3 and 4:

$$\vec{E}_{3,4}(r,\phi,z,t) = A_{3,4}(z)\vec{E}_{T,3,4}(r,\phi)\exp\left(j\beta_{3,4}z - j\omega_{3,4}t\right) + c.c \tag{79}$$

Here $A_{3,4}$ are the complex magnitudes of the two fields [V], $\beta_{3,4}$ are their propagation constants in their respective modes, $\vec{E}_{T,3,4}$ are the corresponding normalized transverse profiles of the two modes, and $\omega_{3,4}$ are their respective optical frequencies. Effective coupling requires matching in both frequency and wavenumber between the pair of optical fields and the photo-elastic perturbations:

$$\omega_3 - \omega_4 = \pm\Omega, \qquad \beta_3 - \beta_4 = \pm K \tag{80}$$

In intra-modal processes, where all four waves involved propagate in the same mode 1, fulfilment of the frequency requirement guarantees the wavenumbers condition is met as well, since all optical waves satisfy:

$$\beta_i = \frac{n_{\mathrm{eff},1}\omega_i}{c},\ i = 1 \dots 4 \tag{81}$$

Whenever $\omega_3 - \omega_4 = \pm\Omega = \pm(\omega_1 - \omega_2)$, we automatically obtain also $\beta_3 - \beta_4 = \pm(\beta_1 - \beta_2) = \pm K$. This property holds as long as chromatic dispersion remains negligible. It suggests that intra-modal forward Brillouin scattering would couple a third, input optical probe wave with both its sidebands, spectrally detuned by $\pm\Omega$, regardless of its optical frequency. The coupling may take the form of phase modulation, polarization rotation, or both, depending on the choice of acoustic mode and the state of polarization of the optical probe wave (see sections 3.5.2, 3.5.3) [11].

The requirement for wavenumber matching is markedly different in the case of inter-modal scattering, in which the acoustic wave is stimulated by optical fields in distinct spatial modes 1 and 2. Let us denote the optical frequencies $\omega_{3,4}$ as $\omega_\mathrm{s} \pm \frac{1}{2}\Omega$, where ω_s is their average. Wavenumber matching in photoelastic coupling between $\vec{E}_{3,4}$ is reached when:

$$\frac{\left(n_{\mathrm{eff},3} - n_{\mathrm{eff},4}\right)\omega_\mathrm{s}}{\mathrm{c}} = \pm\frac{\left(n_{\mathrm{eff},1} - n_{\mathrm{eff},2}\right)\omega_\mathrm{p}}{\mathrm{c}} = \pm K \tag{82}$$

Here $n_{\mathrm{eff},3}$ and $n_{\mathrm{eff},4}$ denote the effective indices in modes 3 and 4, respectively. Wavenumber matching for photoelastic scattering in the inter-modal process is guaranteed between the two pump waves $\vec{E}_{1,2}$ which stimulate the acoustic wave in the first place, as $\omega_\mathrm{s} = \omega_\mathrm{p}$, $n_{\mathrm{eff},3} = n_{\mathrm{eff},1}$ and $n_{\mathrm{eff},4} = n_{\mathrm{eff},2}$. In that case the forward Brillouin interaction is in the stimulated regime, with the same pair of optical waves used to both generate the acoustic wave and to monitor the induced scattering. Forward stimulated Brillouin scattering results in the amplification of the lower-frequency pump field, at the expense of the higher-frequency one (see section 3.5.4) [11]. If the pair of modes 3 and 4 differs from the pair of modes 1 and 2, the wavenumbers for photoelastic coupling between $\vec{E}_{3,4}$ might only be matched for specific frequencies ω_s, if at all.

The photoelastic coupling between a pair of optical waves $\vec{E}_{3,4}$ and a given acoustic mode TR_{pm} is governed by the overlap integral between the transverse profiles of the dielectric perturbations and the two optical modes involved:

$$Q_{3,4,pm}^{(PE)} = \int_0^{2\pi} \int_0^{b} \left[\mu_{rr,pm} E_{r3} E_{r4} + \mu_{\phi\phi,pm} E_{\phi 3} E_{\phi 4} + \mu_{r\phi,pm}\left(E_{r3} E_{\phi 4} + E_{\phi 3} E_{r4}\right)\right] r dr d\phi \qquad (83)$$

Here E_{r3} and E_{r4} denote the radial components of $\vec{E}_{T,3,4}$, respectively, and $E_{\phi 3}$, $E_{\phi 4}$ are the corresponding azimuthal components. Similar to the electro-strictive overlap integral, the photoelastic spatial overlap vanishes unless the azimuthal order p of the acoustic mode equals $l_3 \pm l_4$, where $l_{3,4}$ are the azimuthal orders of optical modes 3 and 4, respectively.

Due to phase matching considerations discussed above, we consider from now on that $\vec{E}_{3,4} = \vec{E}_{1,2}$ respectively. The integrand in Eq. (83) may be rearranged in the following form, where the optical fields are presented as a 2×1 vectors and the dielectric perturbation tensor $\boldsymbol{\mu}_{pm}$ is given by a 2×2 matrix:

$$Q_{1,2,pm}^{(PE)} = \int_0^{2\pi} \int_0^{b} \left[\begin{pmatrix} E_{r2}, & E_{\phi 2} \end{pmatrix} \begin{pmatrix} \mu_{rr,pm} & \mu_{r\phi,pm} \\ \mu_{r\phi,pm} & \mu_{\phi\phi,pm} \end{pmatrix} \begin{pmatrix} E_{r1} \\ E_{\phi 1} \end{pmatrix}\right] r dr d\phi \qquad (84)$$

3.4.3. Equivalence of electro-striction and photoelasticity spatial overlap integrals

In the following section we show that for given two optical modes 1 and 2, the overlap integrals associated with electro-striction and photo-elasticity are identical: $Q_{1,2,pm}^{(ES)} = Q_{1,2,pm}^{(PE)}$. The derivation is detailed in Cartesian coordinates for convenience, but it holds for any choice of coordinates system.

Let us rearrange the overlap integrals in Cartesian coordinates in terms of the tensor elements of the optical and acoustic waves involved. The electro-striction overlap integral in Eq. (69) becomes:

$$Q_{1,2,pm}^{(ES)} = \iint \sum_i f_{i,1,2} u_{i,pm} \, ds \qquad (85)$$

And the spatial overlap integral associated with photo-elasticity in Eq. (83) is given by:

$$Q_{1,2,pm}^{(PE)} = \iint \sum_{i,j} \mu_{ij,pm} I_{ij,1,2} \, ds \qquad (86)$$

Here i, j scan over the transverse Cartesian coordinates x, y.

For electro-striction, we substitute Eqs. (52), (57) into Eq. (85) and get:

$$\sum_i f_{i,1,2}u_{i,pm} = -\sum_i \sum_j \frac{\partial}{\partial j}\tilde{\sigma}_{ij,1,2}\, u_{i,pm} = n_0^4 \sum_i \sum_j \frac{\partial}{\partial j}\left(\sum_{k,l} p_{ijkl} I_{kl,1,2}\right) u_{i,pm} \\ = n_0^4 \sum_{i,j,k,l} p_{ijkl}\, u_{i,pm} \frac{\partial}{\partial j} I_{kl,1,2} \tag{87}$$

Leading to:

$$Q_{1,2,pm}^{(ES)} = n_0^4 \iint \left(\sum_{i,j,k,l} p_{ijkl}\, u_{i,pm} \frac{\partial}{\partial j} I_{kl,1,2}\right) ds \tag{88}$$

In Eq. (87) we assume that the photo-elastic tensor $\boldsymbol{p}$ is constant across the silica fiber cladding. In addition, k, l also scan over x, y. Expressing the summation over $j = x, y$ explicitly, and moving the summation outside the integral, we obtain:

$$Q_{1,2,pm}^{(ES)} = n_0^4 \sum_{i,k,l} \iint \left(p_{ixkl} u_{i,pm} \frac{\partial}{\partial x} I_{kl,1,2} + p_{iykl} u_{i,pm} \frac{\partial}{\partial y} I_{kl,1,2}\right) ds \tag{89}$$

Next, for photo-elasticity we substitute Eqs. (26), (77) into Eq. (86) and obtain:

$$\sum_{i,j} \mu_{ij,pm} I_{ij,1,2} = -n_0^4 \sum_{i,j} \sum_{k,l} p_{ijkl} s_{kl,pm}\, I_{ij,1,2} = -n_0^4 \sum_{i,j,k,l} p_{ijkl} I_{ij,1,2} \frac{\partial}{\partial l} u_{k,pm} \tag{90}$$

With a change of indices $i' = k, j' = l, k' = i, l' = j$, we obtain:

$$\sum_{i,j} \mu_{ij,pm} I_{ij,1,2} = -n_0^4 \sum_{k',l',i',j'} p_{k'l'i'j'} I_{k'l',1,2} \frac{\partial}{\partial j'} u_{i',pm} \tag{91}$$

(The prime superscripts are omitted hereunder). The tensor $\boldsymbol{p}$ is symmetric, hence $p_{klij} = p_{ijkl}$. The photoelastic overlap integral is therefore brought to the following form:

$$Q_{1,2,pm}^{(PE)} = -n_0^4 \sum_{i,j,k,l} \iint p_{ijkl} I_{kl,1,2} \frac{\partial}{\partial j} u_{i,pm} ds \tag{92}$$

Expressing once again the summation with respect to index j in a direct form, we obtain:

$$Q_{1,2,pm}^{(PE)} = -n_0^4 \sum_{i,k,l} \iint \left(p_{ixkl} I_{kl,1,2} \frac{\partial}{\partial x} u_{i,pm} + p_{iykl} I_{kl,1,2} \frac{\partial}{\partial y} u_{i,pm}\right) ds \tag{93}$$

Integration in part yields:

$$Q_{1,2,pm}^{(PE)} = n_0^4 \sum_{i,k,l} \iint \left(p_{ixkl} u_{i,pm} \frac{\partial}{\partial x} I_{kl,1,2} + p_{iykl} u_{i,pm} \frac{\partial}{\partial y} I_{kl,1,2} \right) ds \\ - n_0^4 \sum_{i,k,l} \left[\oint_L p_{ixkl} u_{i,pm} I_{kl,1,2} dy + \oint_L p_{iykl} u_{i,pm} I_{kl,1,2} dx \right] \tag{94}$$

The first two terms in Eq. (94) equal $Q_{1,2,pm}^{(ES)}$ (see Eq. (89)). The last two terms are integrals carried out over the outer circumference of the cladding cross-section. At the cladding edge, $I_{kl,1,2} = 0$. These two terms therefore vanish, and we obtain:

$$Q_{1,2,pm}^{(PE)} = Q_{1,2,pm}^{(ES)} \tag{95}$$

In the following sections we denote both overlaps as:

$$Q_{1,2,pm} = Q_{1,2,pm}^{(ES)} = Q_{1,2,pm}^{(PE)} \tag{96}$$

3.5. Forward Brillouin scattering in few-mode fibers

3.5.1. The opto-mechanical nonlinear coefficient

We now address the forward SBS effect in few-mode fibers, which combines both electro-striction and photo-elasticity as discussed above. We define the opto-mechanical coefficient $\gamma_{1,2,pm}(\Omega)$ [$W^{-1} \times m^{-1}$] which determines the induced modulation of the probe wave in the intra-modal process, and governs the power exchange between the pump waves in the inter-modal process. The opto-mechanical coefficient of the forward SBS process between a pair of optical modes 1 and 2 and an acoustic mode TR_{pm} is given by:

$$\gamma_{1,2,pm}(\Omega) = j \frac{k_0 Q_{1,2,pm}^2}{8 n_0^2 c \rho_0 \Gamma_{pm} \Omega_{pm}^{(\mathrm{R})}} \frac{1}{1 - 2j \dfrac{\Omega - \Omega_{pm}^{(\mathrm{R})}}{\Gamma_{pm}}} \tag{97}$$

Here $\Omega_{pm}^{(\mathrm{R})}$ is the resonance frequency of maximum Brillouin interaction. It is achieved where phase matching conditions are met, governed by the dispersion relations of Eq. (45):

$$\Omega_{pm}^{(\mathrm{R})} \approx \Omega_{pm} + \frac{k_0^2 v_{L,S}^2}{2\Omega_{pm}} (n_{\mathrm{eff},1} - n_{\mathrm{eff},2})^2 \tag{98}$$

Eq. (98) refers to inter-modal scattering, in which the detuning from cut-off is inversely proportional to the acoustic frequency. The resonance frequency $\Omega_{pm}^{(R)}$ practically reduces to the cut-off frequency Ω_{pm} for intra-modal forward Brillouin scattering processes.

The modal linewidth Γ_{pm} depends on the mechanical impedance of media outside the cladding, and its monitoring provides the basis for forward Brillouin fiber sensing [36]. For bare fibers in air, the linewidths are determined by acoustic dissipation in silica and by inhomogeneities in the cladding radius, and scale quadratically with acoustic frequency [74]. Typical values range between tens to hundreds of kHz.

The opto-mechanical coefficient takes up its maximum value on resonance ($\Omega = \Omega_{pm}^{(\mathrm{R})}$), where it is purely imaginary. We define:

$$\gamma_{1,2,pm}^{(0)} = \frac{k_0 Q_{1,2,pm}^2}{8 n_0^2 c \rho_0 \Gamma_{pm} \Omega_{pm}^{(\mathrm{R})}} \tag{99}$$

Eq. (97) takes the form:

$$\gamma_{1,2,pm}(\Omega) = j\gamma_{1,2,pm}^{(0)} \frac{1}{1 - 2j\dfrac{\Omega - \Omega_{pm}^{(\mathrm{R})}}{\Gamma_{pm}}} \tag{100}$$

Typical $\gamma_{1,1,0m}^{(0)}$ values for radial acoustic modes in standard, bare single-mode fibers reach the order of 10 $W^{-1}\times m^{-1}$ [11]. These values are an order of magnitude weaker than those of backward Brillouin scattering in the same fiber, in which the acoustic waves are confined to the core in larger overlap with the optical mode [6,12,13].

The total opto-mechanical spectrum for optical modes 1 and 2 is given by the summation of all acoustic TR modes participating in the F-SBS process:

$$\gamma_{1,2,total}(\Omega) = \sum_{p,m} \gamma_{1,2,pm}(\Omega) \tag{101}$$

3.5.2. Phase modulation of probe waves

We consider here intra-modal interactions and define the probe field which co-propagates with the pump waves in a common spatial mode 1 at the same spatial orientation:

$$\vec{E}_s(r,\phi,z,t) = A_s(z)\vec{E}_{T,1}(r,\phi)\exp(j\beta_s z - j\omega_s t) + c.c \tag{102}$$

The dielectric perturbations induced by the acoustic mode TR_{pm} give rise to additional, nonlinear polarization in the fiber medium:

$$\vec{P}_{pm}^{NL}(r,\phi,z,t) = \varepsilon_0 \Delta\boldsymbol{\varepsilon}_{pm}(r,\phi,z,t)\vec{E}_s(r,\phi,z,t) \tag{103}$$

We substitute Eqs. (76), (102) into Eq. (103) and obtain:

$$\begin{aligned}\vec{P}_{pm}^{NL}(r,\phi,z,t) = \varepsilon_0\big[b_{pm}(\Omega,z)\boldsymbol{\mu}_{pm}(r,\phi)\exp(jKz - j\Omega t) + c.c\big] \\ \cdot\big[A_s(z)\vec{E}_{T,1}(r,\phi)\exp(j\beta_s z - j\omega_s t) + c.c\big]\end{aligned} \tag{104}$$

The nonlinear polarization consists of two harmonic terms of frequencies $\omega_s \pm \Omega$:

$$\begin{aligned}\vec{P}_{pm,+}^{NL}(r,\phi,z,t) = \varepsilon_0 A_s(z) b_{pm}(\Omega,z)\boldsymbol{\mu}_{pm}(r,\phi)\vec{E}_{T,1}(r,\phi)\exp[j(\beta_s + K)z - j(\omega_s + \Omega)t] \\ + c.c\end{aligned} \tag{105}$$

$$\begin{aligned}\vec{P}_{pm,-}^{NL}(r,\phi,z,t) = \varepsilon_0 A_s(z) b_{pm}^*(\Omega,z)\boldsymbol{\mu}_{pm}(r,\phi)\vec{E}_{T,1}(r,\phi)\exp[j(\beta_s - K)z - j(\omega_s - \Omega)t] \\ + c.c\end{aligned} \tag{106}$$

These terms give rise to the generation of optical field sidebands $\vec{E}_\pm$ at frequencies $\omega_s \pm \Omega$:

$$\vec{E}_\pm(r,\phi,z,t) = A_\pm(z)\vec{E}_{T,1}(r,\phi)\exp[j\beta_\pm z - j(\omega_s \pm \Omega)t] + c.c \tag{107}$$

Since all optical fields are guided in the same spatial mode, the field sidebands and the nonlinear polarization terms are wavenumber matched.

The evolution of the optical sideband field components is governed by the nonlinear wave equation for monochromatic waves:

$$\nabla^2\vec{E}_\pm + \beta_\pm^2\vec{E}_\pm = -\frac{(\omega_s \pm \Omega)^2}{\varepsilon_0 c^2}\vec{P}_{pm,\pm}^{NL} \tag{108}$$

We assume that the complex magnitudes $A_\pm(z)$ vary slowly over the axial position z. This assumption leads to the following equations for the evolution of the sideband magnitudes [11]:

$$\frac{\partial A_+(z)}{\partial z}\vec{E}_{T,1} = j\frac{k_0}{2n_0}A_s(z)b_{pm}(\Omega,z)\boldsymbol{\mu}_{pm}\vec{E}_{T,1} \tag{109}$$

$$\frac{\partial A_{-}(z)}{\partial z}\vec{E}_{T,1} = j\frac{k_0}{2n_0}A_s(z)b^*_{pm}(\Omega,z)\boldsymbol{\mu}_{pm}\vec{E}_{T,1} \tag{110}$$

We multiply both terms of Eqs. (109), (110) by $\left(\vec{E}_{T,1}\right)^T$ from the left side and integrate over the transverse plane. For Eq. (109) we obtain:

$$\frac{\partial A_{+}(z)}{\partial z}\int_0^{2\pi}\int_0^{b}\left|\vec{E}_{T,1}\right|^2 r\mathrm{d}r\,\mathrm{d}\phi = j\frac{k_0}{2n_0}A_s(z)b_{pm}(\Omega,z)\int_0^{2\pi}\int_0^{b}\left(\vec{E}_{T,1}\right)^T\boldsymbol{\mu}_{pm}\vec{E}_{T,1}r\mathrm{d}r\,\mathrm{d}\phi \tag{111}$$

The left integral equals 1 due to normalization. In the right integral we may express the field vector and the dielectric perturbation tensor in terms of a 2×1 vector and a 2×2 matrix, respectively. We obtain the photoelastic overlap integral $Q^{(PE)}_{1,1,pm}$ as expressed in Eq. (84). Therefore Eq. (111) may be written as [11]:

$$\frac{\partial A_{+}(z)}{\partial z} = j\frac{k_0}{2n_0}A_s(z)b_{pm}(\Omega,z)\mathrm{Q}_{1,1,pm} \tag{112}$$

Substituting the expression for $b_{pm}(\Omega,z)$ (Eq. (70)) yields:

$$\frac{\partial A_{+}(z)}{\partial z} = jA_s(z)\left[j\frac{k_0 Q^2_{1,1,pm}}{8n_0^2 c\rho_0\Gamma_{pm}\Omega_{pm}}\,\frac{1}{1-2j\dfrac{\Omega-\Omega_{pm}}{\Gamma_{pm}}}\right]P(\Omega,z) \tag{113}$$

The expression in square brackets is exactly the opto-mechanical coefficient as defined in Eq. (97). We get [11]:

$$\frac{\partial A_{+}(z)}{\partial z} = j\gamma_{1,1,pm}(\Omega)P(\Omega,z)A_s(z) \tag{114}$$

Similarly, for the lower sideband we obtain:

$$\frac{\partial A_{-}(z)}{\partial z} = j\gamma^*_{1,1,pm}(\Omega)P^*(\Omega,z)A_s(z) \tag{115}$$

We now assume that the photoelastic scattering of the probe wave is comparatively small, so that $\left|A_{\pm}(z)\right|^2 \ll |A_s(z)|^2$. Therefore, the magnitude of the input probe wave changes very little $A_s(z) \approx A_s(0)$. In addition, we assume that the beating power $P(\Omega)$ is position independent as well. At that limit, Eqs. (114) and (115) are readily solved:

$$A_+(L) = j\gamma_{1,1,pm}(\Omega)P(\Omega)A_s(0)L \tag{116}$$

$$A_-(L) = j\gamma^*_{1,1,pm}(\Omega)P^*(\Omega)A_s(0)L \tag{117}$$

Here L is the total fiber length.

The total magnitude of the probe wave at the end of the fiber is given by:

$$A_{total}(L) = A_s(0)\exp(-j\omega_s t) + A_+(L)\exp(-j(\omega_s+\Omega)t) + A_-(L)\exp(-j(\omega_s-\Omega)t) + c.c \tag{118}$$

We substitute Eqs. (116), (117) and obtain:

$$A_{total}(L) = A_s(0)\exp(-j\omega_s t)\left[1 + j\gamma_{1,1,pm}PL\exp(-j\Omega t) + j\gamma^*_{1,1,pm}P^*L\exp(j\Omega t)\right] + c.c = A_s(0)\exp(-j\omega_s t)\left[1 + j(\gamma_{1,1,pm}PL\exp(-j\Omega t) + c.c)\right] + c.c \tag{119}$$

We use the following approximation for $\varphi \ll 1$:

$$\exp(j\varphi) \approx 1 + j\varphi \tag{120}$$

Assuming that $\left|\gamma_{1,1,pm}(\Omega)P(\Omega)L\right| \ll 1$, Eq. (119) becomes:

$$A_{total}(L) = A_s(0)\exp(-j\omega_s t)\exp\left[j\left(\gamma_{1,1,pm}PL\exp(-j\Omega t) + c.c\right)\right] + c.c \tag{121}$$

We see from Eq. (121) that the sideband field components manifest in phase modulation of the original probe wave. The phase accumulation associated with intra-modal forward SBS propagates along the fiber at acoustic frequency Ω and wavenumber K, and is given by:

$$\Delta\varphi_{pm}(\Omega, L, t) = \gamma_{1,1,pm}(\Omega)P(\Omega)L\exp(jKL - j\Omega t) + c.c \tag{122}$$

The probe wave also acquires phase modulation due to the Kerr effect, which is independent by the frequency Ω [33]. Hence, the total nonlinear coefficient observed in measurements is composed of both opto-mechanical and Kerr nonlinearity:

$$\gamma_{total}(\Omega) = \gamma_{1,1,pm}(\Omega) + \gamma_{Kerr} \tag{123}$$

And the total observed phase accumulation is given by:

$$\Delta\varphi_{total}(\Omega, L, t) = \gamma_{total}(\Omega)P(\Omega)L\exp(jKL - j\Omega t) + c.c \tag{124}$$

3.5.3. Polarization rotation of probe waves

In the previous section we addressed the case in which the optical probe is spatially aligned with the pump waves, and show that the acoustic wave induces phase modulation to the probe wave. We now consider the general case in which the probe is sent in an arbitrary spatial orientation, which may be referred to as an arbitrary state of polarization.

Without loss of generality, we assume that the optical mode guiding all participating fields is in the HE category. The following derivation is similar for the EH category. The optical mode exhibits two spatial orientations, which are denoted as "even" and "odd". For a given azimuthal order l, the modal orientations are obtained from Eq. (15):

$$\vec{E}^{e}_{T,1}(r,\phi) = G_1(r)\left[\cos(l\phi)\,\hat{\boldsymbol{r}} - \sin(l\phi)\,\hat{\boldsymbol{\phi}}\right] \tag{125}$$

$$\vec{E}^{o}_{T,1}(r,\phi) = G_1(r)\left[\sin(l\phi)\,\hat{\boldsymbol{r}} + \cos(l\phi)\,\hat{\boldsymbol{\phi}}\right] \tag{126}$$

Here $G_1(r)$ is the transverse radial profile of the optical mode 1, as obtained in Eq. (16). A general optical field in the given mode is composed of both orientations:

$$\vec{E}_{T,1}(r,\phi) = A_e\vec{E}^{e}_{T,1}(r,\phi) + A_o\vec{E}^{o}_{T,1}(r,\phi) \tag{127}$$

Here A_e and A_o are arbitrary coefficients, satisfying $|A_e|^2 + |A_o|^2 = 1$.

Two pump waves in an intra-modal process stimulate guided acoustic modes with azimuthal orders p that equal either 0 or $2l$ (if $l \neq 0$). Therefore, the pumps may excite the R_{0m} and $TR_{2l,m}$ acoustic categories (like SMFs, the T_{0m} category cannot be addressed through intra-modal interactions). The probe wave may be scattered and modulated by both acoustic categories.

We rearrange the photoelastic overlap integral (Eq. (83)) in the intra-modal case:

$$Q^{(PE)}_{1,1,pm} = \int_0^{2\pi}\int_0^{b}\left[\mu_{rr,pm}E^2_{r1} + \mu_{\phi\phi,pm}E^2_{\phi 1} + 2\mu_{r\phi,pm}E_{r1}E_{\phi 1}\right]r\,dr\,d\phi \tag{128}$$

We first consider the photoelastic scattering by the radial acoustic modes R_{0m}. Given the radial symmetry of the material displacement, we obtain $\mu_{r\phi,0m} = 0$. Moreover, $\mu_{rr,0m}$ and $\mu_{\phi\phi,0m}$ depend only on the radial component r. Therefore, the photoelastic overlap integrals for spatial even and odd orientations are given by:

$$Q_{1,1,0m}^{(PE),e} = \int_0^{2\pi}\int_0^{b} G_1^2(r)\left[\mu_{rr,0m}(r)\cos^2(l\phi) + \mu_{\phi\phi,0m}(r)\sin^2(l\phi)\right] r dr d\phi \tag{129}$$

$$Q_{1,1,0m}^{(PE),o} = \int_0^{2\pi}\int_0^{b} G_1^2(r)\left[\mu_{rr,0m}(r)\sin^2(l\phi) + \mu_{\phi\phi,0m}(r)\cos^2(l\phi)\right] r dr d\phi \tag{130}$$

Since both integrals of $\sin^2(l\phi)$ and $\cos^2(l\phi)$ over the azimuthal component equal π, we obtain that $Q_{1,1,0m}^{(PE),e} = Q_{1,1,0m}^{(PE),o}$. Therefore, an optical probe propagating in an arbitrary state of polarization accumulates the same phase modulation induced by the R_{0m} modes, regardless of its initial orientation.

We now consider the induced modulation from the $TR_{2l,m}$ acoustic modes ($l \neq 0$). The overlap integrals for even and odd orientations are given by:

$$\begin{aligned} Q_{1,1,2l,m}^{(PE),e} = \int_0^{2\pi}\int_0^{b} G_1^2(r)\big[&\mu_{rr,2l,m}(r,\phi)\cos^2(l\phi) + \mu_{\phi\phi,2l,m}(r,\phi)\sin^2(l\phi) \\ &- \mu_{r\phi,2l,m}(r,\phi)\sin(2l\phi)\big] r dr d\phi \end{aligned} \tag{131}$$

$$\begin{aligned} Q_{1,1,2l,m}^{(PE),o} = \int_0^{2\pi}\int_0^{b} G_1^2(r)\big[&\mu_{rr,2l,m}(r,\phi)\sin^2(l\phi) + \mu_{\phi\phi,2l,m}(r,\phi)\cos^2(l\phi) \\ &+ \mu_{r\phi,2l,m}(r,\phi)\sin(2l\phi)\big] r dr d\phi \end{aligned} \tag{132}$$

Since $\cos^2(l\phi) + \sin^2(l\phi) = 1$, summing Eqs. (131), (132) together yields:

$$Q_{1,1,2l,m}^{(PE),e} + Q_{1,1,2l,m}^{(PE),o} = \int_0^{2\pi}\int_0^{b} G_1^2(r)\left[\mu_{rr,2l,m}(r,\phi) + \mu_{\phi\phi,2l,m}(r,\phi)\right] r dr d\phi \tag{133}$$

The dielectric tensor components $\mu_{rr,2l,m}(r,\phi)$, $\mu_{\phi\phi,2l,m}(r,\phi)$ exhibit azimuthal symmetry of $p = 2l$. Therefore, the integral in Eq. (133) vanishes, and we obtain:

$$Q_{1,1,2l,m}^{(PE),o} = -Q_{1,1,2l,m}^{(PE),e} \tag{134}$$

Eq. (134) states that probe waves in the even and odd orientations accumulate phase modulations that are equal in magnitudes but of opposite signs. Phase differences between the two states of polarization manifest in photoelastic birefringence which propagates along the fiber at frequency

Ω and wavenumber K. This induced birefringence rotates the polarization of a general probe field with any other, arbitrary spatial orientation.

Polarization rotation of probe waves may also occur through optical power coupling between different modes within the same LP group. For example, the LP_{11} group consists of the TE_{01}, TM_{01} modes with azimuthal order 0, and the HE_{21} mode with azimuthal order 2. All optical modes are launched together in intra-modal forward SBS as either pumps or probe. Through this process, acoustic waves stimulated by the pumps may couple between the corresponding modal components of the probe. For example, optical power might be exchanged between the TM_{01} and the HE_{21} mode, thus changing the total transverse profile of the electric field vector and rotating its polarization. Moreover, different modes within the same LP group may be scattered by the same acoustic mode. However, their phase modulations are different since they are determined by the specific optical mode (see Eq. (83)). Different phase accumulations also manifest in polarization rotation of the total probe field.

3.5.4. Coupling of power between pump waves

In this section we consider the inter-modal optical power coupling between the two pump waves that stimulate the acoustic waves in the first place. For convenience we bring again the expression of the two pumps co-propagating at optical modes 1 and 2 (Eq. (46)):

$$\vec{E}_1(r,\phi,z,t) = A_1(z)\vec{E}_{T,1}(r,\phi)\exp\left[j\beta_1 z - j\left(\omega_p + \frac{1}{2}\Omega\right)t\right] + c.c \tag{135}$$

$$\vec{E}_2(r,\phi,z,t) = A_2(z)\vec{E}_{T,2}(r,\phi)\exp\left[j\beta_2 z - j\left(\omega_p - \frac{1}{2}\Omega\right)t\right] + c.c \tag{136}$$

Without loss of generality, in Eqs. (135), (136) we assumed that the optical mode 1 is the higher frequency tone and mode 2 is the lower frequency one. The pump waves stimulate guided acoustic modes at frequency Ω and wavenumber $K = \beta_1 - \beta_2$. The acoustic modes, in turn, induce dielectric perturbations which scatter the pump waves and couple between them.

The nonlinear polarization associated with the pump waves and with a TR_{pm} acoustic mode is given by:

$$\vec{P}_{pm}^{NL}(r,\phi,z,t) = \varepsilon_0 \Delta\boldsymbol{\varepsilon}_{pm}(r,\phi,z,t)\left[\vec{E}_1(r,\phi,z,t) + \vec{E}_2(r,\phi,z,t)\right] \tag{137}$$

We substitute Eqs. (76), (135), (136) into Eq. (137) and obtain two polarization terms at frequencies $\omega_p \pm \frac{1}{2}\Omega$:

$$\vec{P}^{NL}_{pm,\frac{1}{2}} = \varepsilon_0 A_2(z) b_{pm}(\Omega, z) \boldsymbol{\mu}_{pm}(r,\phi) \vec{E}_{T,2}(r,\phi) \exp\left[j(\beta_2 + K)z - j\left(\omega_p + \frac{1}{2}\Omega\right)t\right] + c.c \quad (138)$$

$$\vec{P}^{NL}_{pm,-\frac{1}{2}} = \varepsilon_0 A_1(z) b^*_{pm}(\Omega, z) \boldsymbol{\mu}_{pm}(r,\phi) \vec{E}_{T,1}(r,\phi) \exp\left[j(\beta_1 - K)z - j\left(\omega_p - \frac{1}{2}\Omega\right)t\right] + c.c \quad (139)$$

The nonlinear polarization terms drive a pair of nonlinear wave equations for the two pump fields:

$$\nabla^2 \vec{E}_1 + \beta_1^2 \vec{E}_1 = -\frac{\left(\omega_p + \frac{1}{2}\Omega\right)^2}{\varepsilon_0 c^2} \vec{P}^{NL}_{pm,\frac{1}{2}} \quad (140)$$

$$\nabla^2 \vec{E}_2 + \beta_2^2 \vec{E}_2 = -\frac{\left(\omega_p - \frac{1}{2}\Omega\right)^2}{\varepsilon_0 c^2} \vec{P}^{NL}_{pm,-\frac{1}{2}} \quad (141)$$

We notice that the nonlinear polarization term which drives Eq. (140) is governed by $\vec{E}_2$ and the term driving Eq. (141) is determined by $\vec{E}_1$. Therefore, the optical pump fields are coupled together through the acoustic wave. Moreover, the optical fields and the nonlinear polarization terms are phase-matched in both equations. We solve the nonlinear equations assuming that the complex magnitudes $A_{1,2}(z)$ vary slowly over the axial position z. We obtain the following equations [11]:

$$\frac{\partial A_1(z)}{\partial z} \vec{E}_{T,1} = j \frac{k_0}{2n_0} A_2(z) b_{pm}(\Omega, z) \boldsymbol{\mu}_{pm} \vec{E}_{T,2} \quad (142)$$

$$\frac{\partial A_2(z)}{\partial z} \vec{E}_{T,2} = j \frac{k_0}{2n_0} A_1(z) b^*_{pm}(\Omega, z) \boldsymbol{\mu}_{pm} \vec{E}_{T,1} \quad (143)$$

We multiply both terms of Eqs. (142), (143) by the transverse profiles of the optical modes $\left(\vec{E}_{T,1,2}\right)^T$ respectively and integrate over the transverse plane. Following the procedure of section 3.5.2 we get [11]:

$$\frac{\partial A_1(z)}{\partial z} = j \frac{k_0}{2n_0} A_2(z) b_{pm}(\Omega, z) \mathrm{Q}_{1,2,pm} \quad (144)$$

$$\frac{\partial A_2(z)}{\partial z} = j\frac{k_0}{2n_0}A_1(z)b_{pm}^*(\Omega,z)\mathrm{Q}_{1,2,pm} \tag{145}$$

Substituting the expression for $b_{pm}(\Omega,z)$ (Eq. (70)) we obtain:

$$\frac{\partial A_1(z)}{\partial z} = j\gamma_{1,2,pm}(\Omega)P(\Omega,z)A_2(z) \tag{146}$$

$$\frac{\partial A_2(z)}{\partial z} = j\gamma_{1,2,pm}^*(\Omega)P^*(\Omega,z)A_1(z) \tag{147}$$

The coupled wave equations can be brought to describe the evolution of the two optical power levels. We substitute $P_{1,2}(z) = 2n_0c\varepsilon_0\left|A_{1,2}(z)\right|^2$ respectively and $P(\Omega,z) = 2n_0c\varepsilon_0A_1(z)A_2^*(z)$. We obtain [11]:

$$\frac{\partial P_1(z)}{\partial z} = -2\mathrm{Im}\{\gamma_{1,2,pm}(\Omega)\}P_1(z)P_2(z) \tag{148}$$

$$\frac{\partial P_2(z)}{\partial z} = 2\mathrm{Im}\{\gamma_{1,2,pm}(\Omega)\}P_1(z)P_2(z) \tag{149}$$

The imaginary part of $\gamma_{1,2,pm}(\Omega)$ is positive for all Ω. Eqs. (148), (149) therefore signify the stimulated forward Brillouin amplification of the lower frequency pump field $\vec{E}_2$ at the expense of the higher frequency one $\vec{E}_1$. Monitoring the power transfer between the pump waves may reveal the inter-modal forward SBS spectrum of the two specific optical modes 1 and 2.

4. Numerical analysis

The parameters of the step-index few-mode fiber used in numerical analysis of forward SBS processes are listed in the following table:

Parameter	Value [Units]
n_1	1.461 [RIU]
n_2, n_0	1.445 [RIU]
a	4.8 [µm]
b	62.8 [µm]
ρ_0	2200 [kg/m^3]
v_L	5970 [m/s]
v_S	3736 [m/s]
p_{11}	0.121
p_{12}	0.27

Table 1 – Parameters of the step-index FMF used in the numerical calculations

The parameters in table 1 were fitted based on the few-mode fiber used in experiments. The V parameter of the fiber at a vacuum wavelength of 1550 nm is 4.196, and it supports the LP_{01} and LP_{02} modes and the LP_{11} and LP_{21} mode groups. The mode multiplexers used in our experiments supported the selective coupling of light to the LP_{01} mode, LP_{02} mode, and LP_{11} group only, hence the LP_{21} mode group was not considered in the numerical calculations. The effective indices for the LP_{01} mode, LP_{02} mode, and LP_{11} mode group are 1.458, 1.446, and 1.453 [RIU], respectively. The differences between the effective indices of the three constituent modes of the LP_{11} group are below 5×10^{-5} RIU.

The calculated F-SBS spectra for both intra-modal and inter-modal processes in a FMF are presented below. In the following calculations, we assume that the fiber was uncoated with air outside the cladding. The modal linewidths of the acoustic modes Γ_{pm} were fitted based on experiments [11].

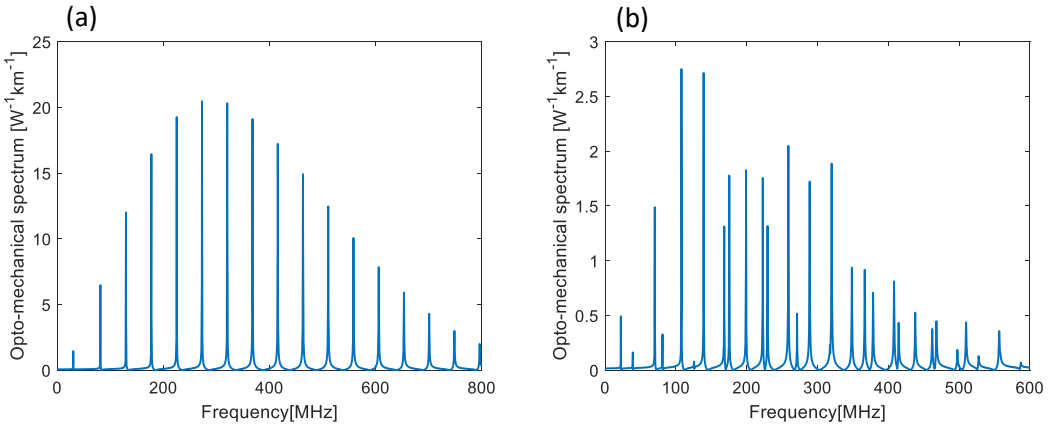

Figure 17 – Calculated opto-mechanical spectra $|\gamma(\Omega/2\pi)|$ of intra-modal forward SBS between two optical waves in the fundamental LP_{01} mode. (a): Scattering through radial acoustic modes R_{0m}. (b): Scattering through torsional-radial acoustic modes of two-fold azimuthal symmetry TR_{2m}.

Figure 17(a) presents the calculated opto-mechanical spectrum $\left|\gamma_{LP01,LP01,0m}(\Omega)\right|$ of intra-modal forward SBS between two optical waves in the fundamental LP_{01} mode, through the radial acoustic modes R_{0m}. Figure 17(b) shows the corresponding spectrum $\left|\gamma_{LP01,LP01,2m}(\Omega)\right|$ for the same optical mode and the TR_{2m} acoustic modes. Both spectra are very similar to those of the corresponding processes in standard SMFs [7-11]. Forward SBS through the R_{0m} modes is stronger, with $\gamma^{(0)}_{LP01,LP01,0m}$ reaching 20 W^{-1}×km^{-1} at frequencies near 300 MHz. The peak magnitudes $\gamma^{(0)}_{LP01,LP01,0m}$ decrease monotonously beyond that frequency. The radial modes are purely dilatational, with regular spacing between their resonance frequencies (Figure 17(a)). The spectrum of Figure 17(b) consists of both predominantly dilatational and shear-like TR_{2m} acoustic modes, with overall irregular spacing between peaks [44,45,56]. The $\left|\gamma_{LP01,LP01,2m}(\Omega)\right|$ spectrum also decreases considerably beyond acoustic frequencies of 500 MHz. At higher frequencies, the radial dependence of the material displacement profile $\vec{u}_{pm}$ changes sign within the spatial extent of the fundamental optical mode, and the spatial overlap integral largely cancels out.

Figure 18 presents the opto-mechanical spectra of intra-modal F-SBS in the LP_{02} mode. R_{0m} and TR_{2m} acoustic modes are considered in panels 18(a) and 18(b), respectively. Note that both spectra are plotted on logarithmic scales. The peaks of the radial modes spectrum $\left|\gamma_{LP02,LP02,0m}(\Omega)\right|$ reach a maximum at 300 MHz and decrease by nearly two orders of magnitude towards 600 MHz. The peak magnitudes $\gamma^{(0)}_{LP02,LP02,0m}$ increase again towards acoustic frequencies of 1.2 GHz. Compared with the fundamental LP_{01} mode, the radial profiles of the displacement vectors of a high-frequency acoustic modes match better with the higher-order

LP_{02} mode. The $\left|\gamma_{LP02,LP02,2m}(\Omega)\right|$ spectrum of panel 18(b) consists again of dilatational as well as shear TR_{2m} modes. In the 500-900 MHz range, the spectrum is dominated by the shear modes, identified by the closer spacing $v_S/(2b)$ between adjacent peaks. In that frequencies range, the shorter-period radial oscillations in the shear modes better match the radial profile of optical mode LP_{02} than those of the dilatational ones. The dilatational modes, noted by larger frequency spacing of approximately $v_L/(2b)$, become dominant beyond 1 GHz frequency.

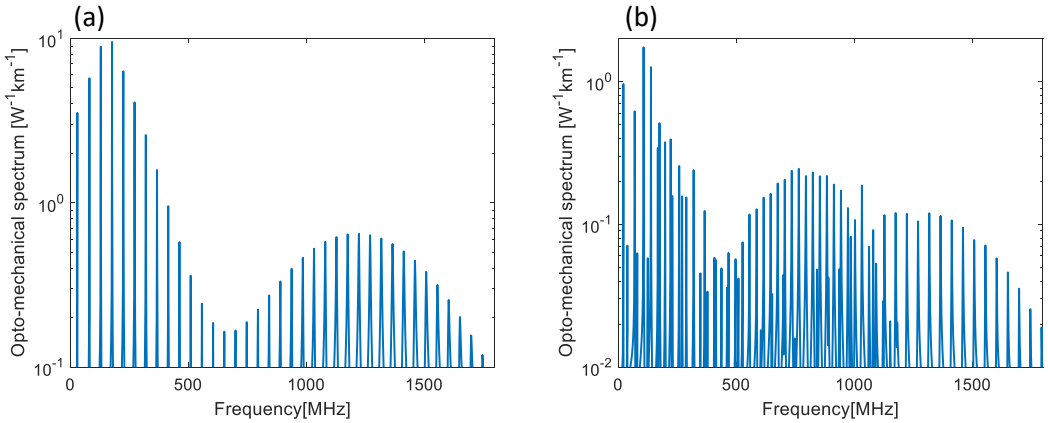

Figure 18 – Calculated opto-mechanical spectra $|\gamma(\Omega/2\pi)|$ of intra-modal forward SBS between two optical waves in the LP_{02} mode. (a): Scattering through radial acoustic modes R_{0m}. (b): Scattering through torsional-radial acoustic modes of two-fold azimuthal symmetry TR_{2m}.

Figure 19 shows the calculated spectra of inter-modal forward SBS between the LP_{01} and LP_{02} modes. In this figure, the imaginary part of the gain coefficient $\mathrm{Im}\{\gamma_{LP01,LP02,pm}(\Omega)\}$ is plotted, rather than its absolute value as in Figures 17 and 18. The experimental procedure for the characterization of inter-modal scattering processes measured the optical power exchange between the optical waves, which is determined directly by the imaginary part [11] (see section 5.2). Here too, only the R_{0m} and TR_{2m} acoustic modes may be stimulated. Panel 19(a) presents the $\mathrm{Im}\{\gamma_{LP01,LP02,0m}(\Omega)\}$ spectrum, and $\mathrm{Im}\{\gamma_{LP01,LP02,2m}(\Omega)\}$ is plotted in panel 19(b). Both spectra differ from those of the intra-modal scattering processes through the same acoustic modes, as seen in Figures 17 and 18. The inter-modal scattering spectrum through the TR_{2m} modes is dominated by shear modes up to 700 MHz frequency and by dilatational modes above that frequency.

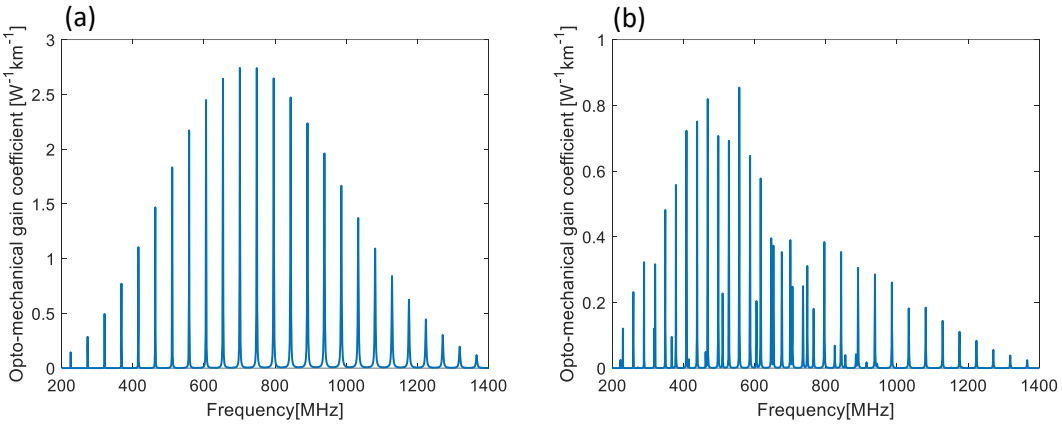

Figure 19 – Calculated opto-mechanical gain coefficients $Im\{\gamma(\Omega/2\pi)\}$ of inter-modal forward SBS between one optical wave in the LP_{01} mode and another in the LP_{02} mode. (a): Coupling through radial acoustic modes R_{0m}. (b): Coupling through torsional-radial acoustic modes of two-fold azimuthal symmetry TR_{2m}.

Figure 20 presents calculated spectra of forward Brillouin scattering interactions driven by optical fields in the LP_{11} mode group. The group consists of the TE_{01}, TM_{01} and HE_{21} exact modal solutions. The experimental setup only allows for the coupling of light to all three modes together, and it does not separate between them. Panel 20(a) presents the $\left|\gamma_{LP11,LP11,0m}(\Omega)\right|$ forward Brillouin scattering spectrum through the radial R_{0m} acoustic modes. The spectrum includes contributions of intra-modal scattering within each of the three modes within the LP_{11} mode group. The radio frequency phases of the three contributions may vary. In the example shown here, the mean value of the three terms is presented. The spectrum extends towards higher frequencies than those of the corresponding process in the fundamental LP_{01} mode (Figure 17(a)). The frequencies range is similar to that of the intra-modal scattering in the LP_{02} mode (Figure 18(a)). The forward Brillouin scattering spectrum $\left|\gamma_{LP11,LP11,2m}(\Omega)\right|$ for TR_{2m} acoustic modes is shown in Figure 20(b). The spectrum differs from those of TR_{2m} modes stimulated by other optical modes combinations, as presented earlier. It is dominated by dilatational modes above acoustic frequencies of 800 MHz.

Optical waves within the LP_{11} modes group can stimulate additional classes of acoustic modes, beyond the R_{0m} and TR_{2m} discussed thus far. Figure 20(c) shows the spectrum $\left|\gamma_{LP11,LP11,4m}(\Omega)\right|$ of forward Brillouin scattering through the four-fold symmetric TR_{4m} acoustic modes. These modes can be driven by two pump fields in the HE_{21} optical mode within the LP_{11} group. This class of acoustic modes cannot be observed in forward Brillouin scattering over SMFs. Shear modes within the TR_{4m} category dominate the spectrum up to 700 MHz, giving way to dilatational modes at higher frequencies. The cut-off frequencies Ω_{4m} of the TR_{4m} modes are similar to those

of the TR_{2m} modes. However, the Ω_{4m} frequencies are consistently lower than the corresponding Ω_{2m} values by 2π×1-2 MHz. These offsets are used to identify peaks associated with the TR_{4m} modes in experimental measurements (see section 5.3).

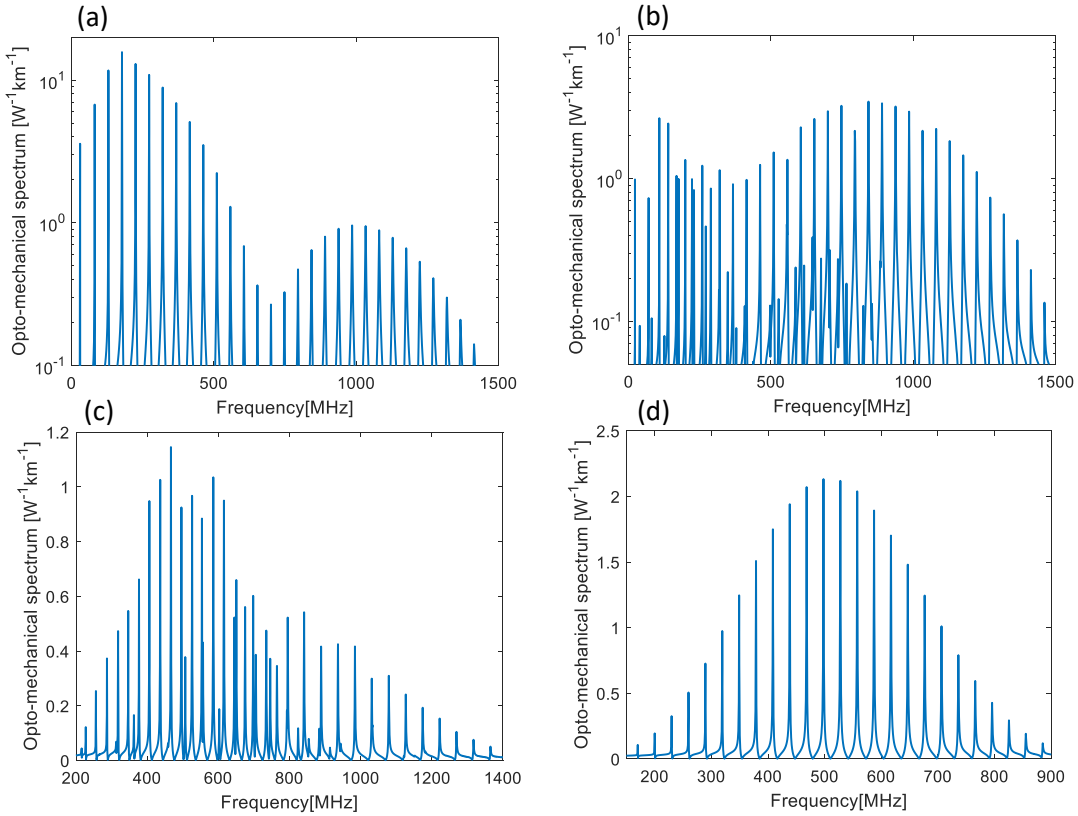

Figure 20 – Calculated opto-mechanical spectra $|\gamma(\Omega/2\pi)|$ of forward SBS between optical waves within the LP_{11} mode group. (a): Scattering through radial acoustic modes R_{0m}. (b): Scattering through torsional-radial acoustic modes of two-fold azimuthal symmetry TR_{2m}. (c): Scattering through torsional-radial acoustic modes of four-fold azimuthal symmetry TR_{4m}. (d): Scattering through purely torsional acoustic modes T_{0m}.

Inter-modal forward Brillouin scattering between one optical field in the TE_{01} mode and another in the TM_{01} mode within the LP_{11} group can stimulate purely torsional T_{0m} acoustic modes as well. The calculated spectrum is shown in Figure 20(d). The process couples optical power between the TE_{01} and TM_{01} components of the LP_{11} mode group. The cut-off frequencies of the T_{0m} are higher than those of adjacent TR_{2m} modes by 2π×1-2 MHz. The peak magnitudes of the opto-mechanical stimulation of T_{0m} modes are highest near 500 MHz frequency. Material displacement in the T_{0m} modes includes shear wave motion only.

Lastly, Figure 21 shows the calculated spectra of inter-modal forward Brillouin scattering between one optical wave in the fundamental LP_{01} mode and another in the LP_{11} modes group. The process involves the stimulation of the TR_{1m} acoustic modes of first-order azimuthal symmetry

(panel (a)), and the three-fold symmetric TR_{3m} modes (panel (b)). Both classes of modes are inaccessible to forward Brillouin scattering in SMFs. The peak magnitudes of $\mathrm{Im}\{\gamma_{LP01,LP11,1m}(\Omega)\}$, corresponding to the TR_{1m} modes, are four times stronger than those of $\mathrm{Im}\{\gamma_{LP01,LP11,3m}(\Omega)\}$, representing the TR_{3m} modes. The spectrum of TR_{1m} modes is dominated by the dilatational ones.

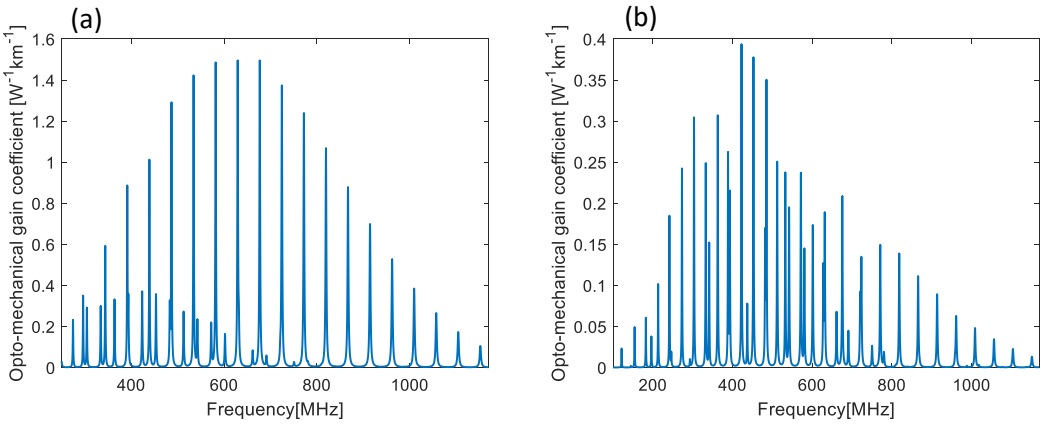

Figure 21 – Calculated opto-mechanical gain coefficients $Im\{\gamma(\Omega/2\pi)\}$ of inter-modal forward SBS between one optical wave in the LP_{01} mode and another in the LP_{11} mode group. (a): Coupling through torsional-radial acoustic modes TR_{1m} of first-order azimuthal symmetry. (b): Coupling through torsional-radial acoustic modes of three-fold azimuthal symmetry TR_{3m}.

5. Experimental setup and results

5.1. Experimental setup for intra-modal measurements

Schematic illustration of the experimental setup for the characterization of intra-modal F-SBS in a few-mode fiber is shown in Figure 22 [11,75]. A laser diode of 1550 nm wavelength was the source of pump optical waves used to stimulate acoustic modes in the fiber. Pump light passed through an electro-optic intensity modulator, driven by a sine wave voltage of variable radio frequency Ω from the output port of an electrical vector network analyzer. The modulated pump wave was amplified in an erbium-doped fiber amplifier to an average optical power of 0.2-0.4 W and launched to one of the three input ports of a first mode-division multiplexer. In some of the measurements, a polarization scrambler was used in the pump branch. The magnitude of the pump power modulation $P_p(\Omega)$ was calibrated for each radio frequency.

The mode multiplexer coupled the input pump wave to either the fundamental LP_{01} mode, the LP_{02} mode, or the LP_{11} mode group. The FMF under test was 5 meters long, and its parameters were specified in the previous Section 4. The fiber was stripped off its protective polymer coating to enhance forward SBS interactions. The coating was removed through mechanical stripping and overnight immersion in acetone for the removal of residues. The output end of the fiber under test was connected to a second mode division multiplexer which separated the LP_{01} mode, the LP_{02} mode, and the LP_{11} group to three different physical output ports. An optical bandpass filter blocked the pump wave at the mode multiplexer output.

A continuous-wave signal from a second laser diode was used for monitoring the stimulated acoustic waves through photoelastic scattering. The signal wavelength was 1532 nm and its optical power was 2 mW. The signal wave was coupled with the modulated pump and launched into the same input port of the mode division multiplexer. The stimulated acoustic waves imprinted phase modulation and/or polarization rotation at radio frequency Ω on the co-propagating signal wave [11]. The optical bandpass filter at the fiber under test output was adjusted to transmit the signal wave.

The output signal was analyzed through two detection channels. In one channel, the output signal was connected through a directional coupler to form a Sagnac interferometer loop [75]. Photoelastic phase modulation of the signal wave was converted to an intensity reading at the loop output [75]. Polarization controllers were used to maximize the output intensity modulation

[75]. The output signal wave was detected by a photo-receiver of 1.6 GHz bandwidth, and the obtained voltage was connected to the input port of the electrical vector network analyzer. The analyzer measured the transfer function $S(\Omega)$ of radio frequency voltage between the modulation of the optical pump wave and that of the detected signal wave. Traces were acquired with frequency steps of 10-20 kHz and an intermediate frequency bandwidth of 100 kHz, and they were averaged over 200 repetitions.

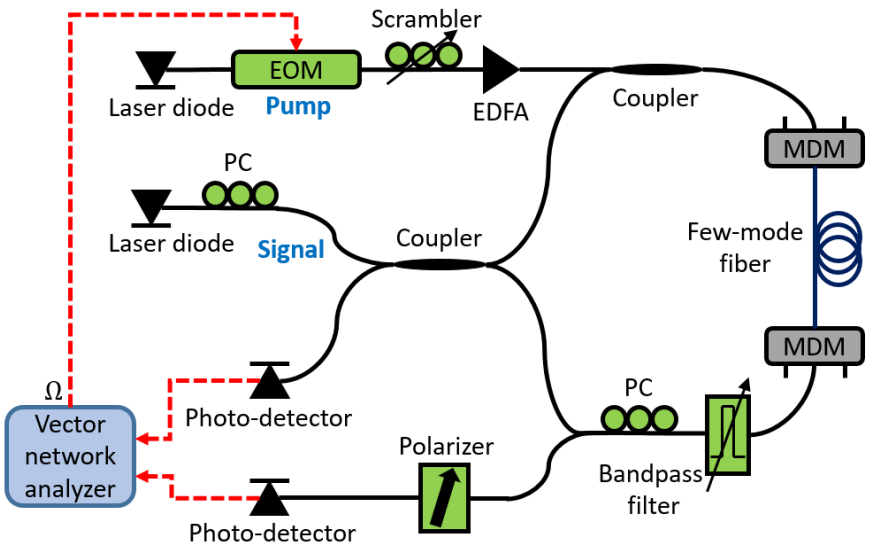

Figure 22 – Schematic illustration of the experimental setup used in characterization of intra-modal F-SBS in a few-mode fiber. EOM: Mach-Zehnder electro-optic intensity modulator; EDFA: erbium-doped fiber amplifier; MDM: mode division multiplexer; PC: polarization controller.

The frequency response of the forward SBS process was estimated by the ratio $H(\Omega) = S(\Omega)/P_p(\Omega)$ [11,75]. The polarization of the pump wave was scrambled during data acquisition at hundreds of kHz rates. In that manner, the contributions of all TR modes to the photoelastic modulation were canceled out of the collected data [76]. The measured response $H(\Omega)$ was affected by the intra-modal F-SBS through the radial modes R_{0m} only.

The signal wave at the output of the optical bandpass filter was split to a second detection channel which was based on a polarizer. A polarization controller was used to align the signal state of polarization to 50% transmission of optical power to the polarizer output. Photoelastic polarization rotation of the signal wave was converted to intensity modulation at the polarizer output [56]. Polarization rotation takes place through torsional-radial modes of all orders, but not through radial modes [76]. The output signal was routed to an identical photo-receiver and the detected voltage was analyzed by the vector network analyzer using the same settings. The

transfer function $H(\Omega) = S(\Omega)/P_p(\Omega)$ of radio-frequency voltage in this case is related to the intra-modal F-SBS through all TR_{pm} modes, of all azimuthal orders [76]. The polarization of the pump wave was not scrambled when using this detection channel.

In addition to forward SBS, the pump wave also induced phase modulation and polarization rotation of the signal via the Kerr effect [77]. The response of the Kerr effect is that of an immediate impulse, whereas that of photoelastic modulation extends over microseconds scale. The contribution of the Kerr effect may be effectively removed from the measurements using time gating, which eliminates the first few nanoseconds of the response [75]. Such gating is often performed by a synchronized optical switch within the experimental testbed [75]. Alternatively, when the output signal is acquired in the time domain, gating can be implemented through offline processing [36,77]. In this work, the F-SBS processes were monitored in the frequency domain, and time gating could not be implemented directly. Instead, the inverse-Fourier transform of the complex-valued $H(\Omega)$ was calculated offline to obtain the corresponding time-domain impulse response $h(t)$. The impulse response was then gated to remove the contribution of the Kerr effect, and the Fourier transform $\widetilde{H}(\Omega)$ of the gated $\tilde{h}(t)$ was calculated for further data analysis. The obtained $\widetilde{H}(\Omega)$ is proportional to the intra-modal F-SBS coefficient $\gamma_{1,1,pm}(\Omega)$, through either the radial or the torsional-radial modes.

5.2. Experimental setup for inter-modal measurements

Figure 23 presents a schematic illustration of the setup for characterization of inter-modal F-SBS in the same few-mode fiber [11,65]. Light from a laser diode source of 1550 nm wavelength was split into two paths. Light in the upper branch passed through a single-sideband electro-optic modulator, driven by voltage of variable radio frequency Ω from the output port of a microwave generator. The optical frequency of the upper branch wave was thereby offset by Ω. The light wave was then intensity-modulated in an electro-optic Mach-Zehnder modulator, driven by a sine wave voltage of frequency f_1 = 200 kHz from one output port of a dual-channel lock-in amplifier. The modulated wave was amplified to an average optical power of 0.1 W and launched to the few-mode fiber through one input port of the mode-division multiplexer.

The optical wave at the lower branch was intensity modulated at frequency f_2 = 503 kHz in a second electro-optic Mach-Zehnder modulator, driven by voltage from a second output port of the lock-in amplifier. The lower branch wave was amplified to 0.5 W average power and launched

through the fiber under test through a second, different port of the mode division multiplexer. Inter-modal forward SBS may lead to the coupling of optical power between the two input waves, depending on their frequency offset Ω. Such coupling manifests in intensity modulation of both waves at frequencies $f_1 \pm f_2$ [11,65].

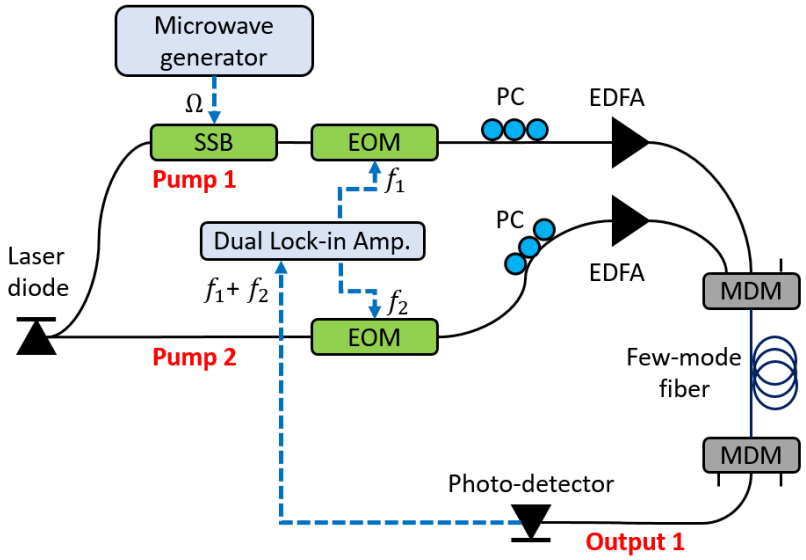

Figure 23 – Schematic illustration of the experimental setup used in characterization of inter-modal F-SBS in a few-mode fiber. EOM: Mach-Zehnder electro-optic intensity modulator; SSB: single-sideband electro-optic modulator; EFDA: erbium-doped fiber amplifier; MDM: mode division multiplexer; PC: polarization controller.

Light from one of the output ports of the second mode division multiplexer, located at the far end of the fiber under test, was detected using a photo-receiver of 20 GHz bandwidth. The detected voltage was analyzed at the input port of the lock-in amplifier, and the magnitude of the $f_1 + f_2$ frequency component was monitored. That component is proportional to the coupling coefficient of inter-modal forward SBS, $\mathrm{Im}\{\gamma(\Omega)\}$ [65]. The coupling of power may take place through all acoustic modes, radial and torsional-radial ones. Note that the Kerr effect does not induce coupling of optical power between the two fields, and its removal was not required as part of this protocol.

5.3. Results: forward Brillouin scattering spectra in a few-mode fiber

Figure 24(a) shows the measured normalized spectrum $\left|\gamma_{LP01,LP01,0m}(\Omega)\right|^2$ of intra-modal forward SBS in the fundamental LP_{01} mode of a few-mode fiber, through the radial acoustic modes R_{0m}. The corresponding calculated spectrum is plotted as well (see Figure 17(a)). The agreement between experiment and calculations is very good. The spectrum is very similar to that

of F-SBS through the same acoustic modes in single-mode fibers [7-11], as expected. The linewidths of the spectral peaks increase with frequency, from 100 kHz for the peak observed at 80 MHz up to about 1 MHz at the resonance frequency of 700 MHz. The linewidths are broader than previously observed in uncoated SMFs, and they scale linearly with acoustic frequency. Such scaling suggests broadening due to non-uniformity of the cladding diameter along the fiber under test [74]. Figure 24(b) presents the normalized measured and calculated spectra of intra-modal scattering in the fundamental optical mode through torsional-radial acoustic modes. The spectrum consists of two-fold symmetric TR_{2m} modes only. Here too, the experimental results agree with calculations and with known results in SMFs [7-11]. Both dilatational and shear modes are observed.

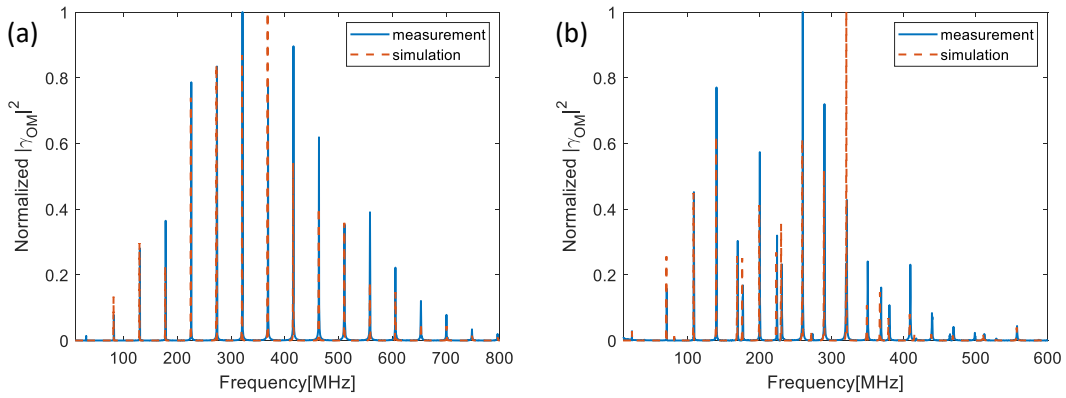

Figure 24 – Measured (solid, blue) and calculated (dashed, red) normalized spectra $\left|\gamma_{LP01,LP01,pm}(\Omega)\right|^2$ of intra-modal forward SBS in the fundamental LP_{01} mode of a few-mode fiber. (a): Radial acoustic modes R_{0m}. (b): Torsional-radial modes. The spectrum consists of the TR_{2m} modes only.

Figure 25 shows the measured and calculated normalized spectra of intra-modal forward SBS in the higher-order LP_{02} mode. Here too, the process takes place through R_{0m} (panel (a)) and TR_{2m} acoustic modes (panel (b)). Modes of both categories are observed up to a frequency of 1.8 GHz, much higher than those of corresponding intra-modal scattering in the fundamental mode. The peak magnitudes of the dilatational R_{0m} modes pass through a local minimum at acoustic frequencies near 800 MHz, due to poor spatial overlap with the optical mode. The TR_{2m} modes spectrum at that frequency range is dominated by the shear modes, identified by their closer spectral spacing, which exhibit better spatial overlap with the optical mode. The dilatational modes dominate the TR_{2m} spectrum beyond 1.1 GHz frequency. The experimental observations are in good agreement with calculations.

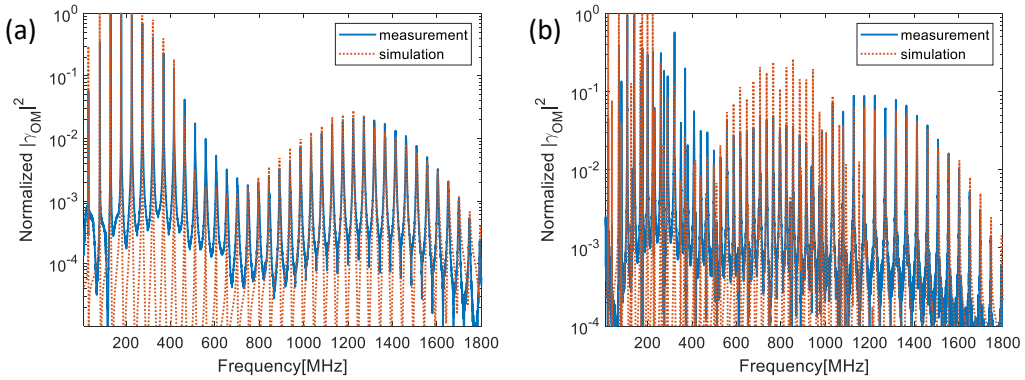

Figure 25 – Measured (solid, blue) and calculated (dashed, red) normalized spectra $\left|\gamma_{LP02,LP02,pm}(\Omega)\right|^2$ of intra-modal forward SBS in the LP_{02} mode of a few-mode fiber. (a): Radial acoustic modes R_{0m}. (b): Torsional-radial modes. The spectrum consists of the TR_{2m} modes only.

Next, the normalized spectra of forward SBS between two optical fields in the LP_{11} group are presented. Figure 26 shows the spectrum of scattering through the radial R_{0m} modes, $\left|\gamma_{LP11,LP11,0m}(\Omega)\right|^2$. The measurements meet expectations. Figure 27(a) shows the corresponding spectra for torsional radial modes. The spectrum is dominated by the two-fold symmetric TR_{2m} modes, and it matches well with calculations. This time, however, many of the spectral peaks corresponding to the TR_{2m} modes are accompanied by adjacent secondary peaks, at frequencies that are 1-2 MHz lower. The second set of peaks represents the stimulation of the four-fold symmetric TR_{4m} modes. The observed frequency separation matches the difference between calculated cut-off frequencies $(\Omega_{2m} - \Omega_{4m})/2\pi$. The TR_{4m} acoustic modes are driven by optical fields in the HE_{21} component of the LP_{11} group. They do not appear in the spectra of torsional-radial modes for intra-modal forward SBS in the LP_{01} and LP_{02} modes. Four examples of pairs of peaks are shown in Figures 27(b), (c), (d) and (e), yet other similar pairs were observed in the frequencies range of 200-400 MHz. The results signify the first observation of the TR_{4m} class of modes in forward Brillouin scattering in fibers.

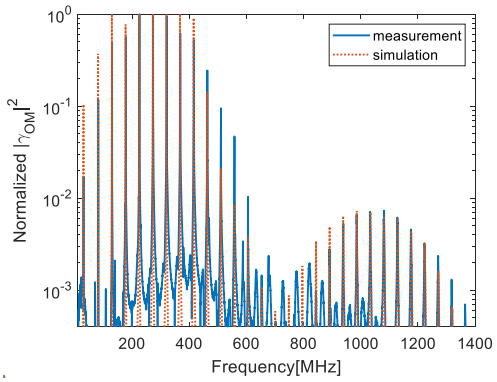

Figure 26 – Measured (solid, blue) and calculated (dashed, red) normalized spectra $\left|\gamma_{LP11,LP11,0m}(\Omega)\right|^2$ of intra-modal forward SBS in the LP_{11} modes group of a few-mode fiber, through the radial acoustic modes R_{0m}.

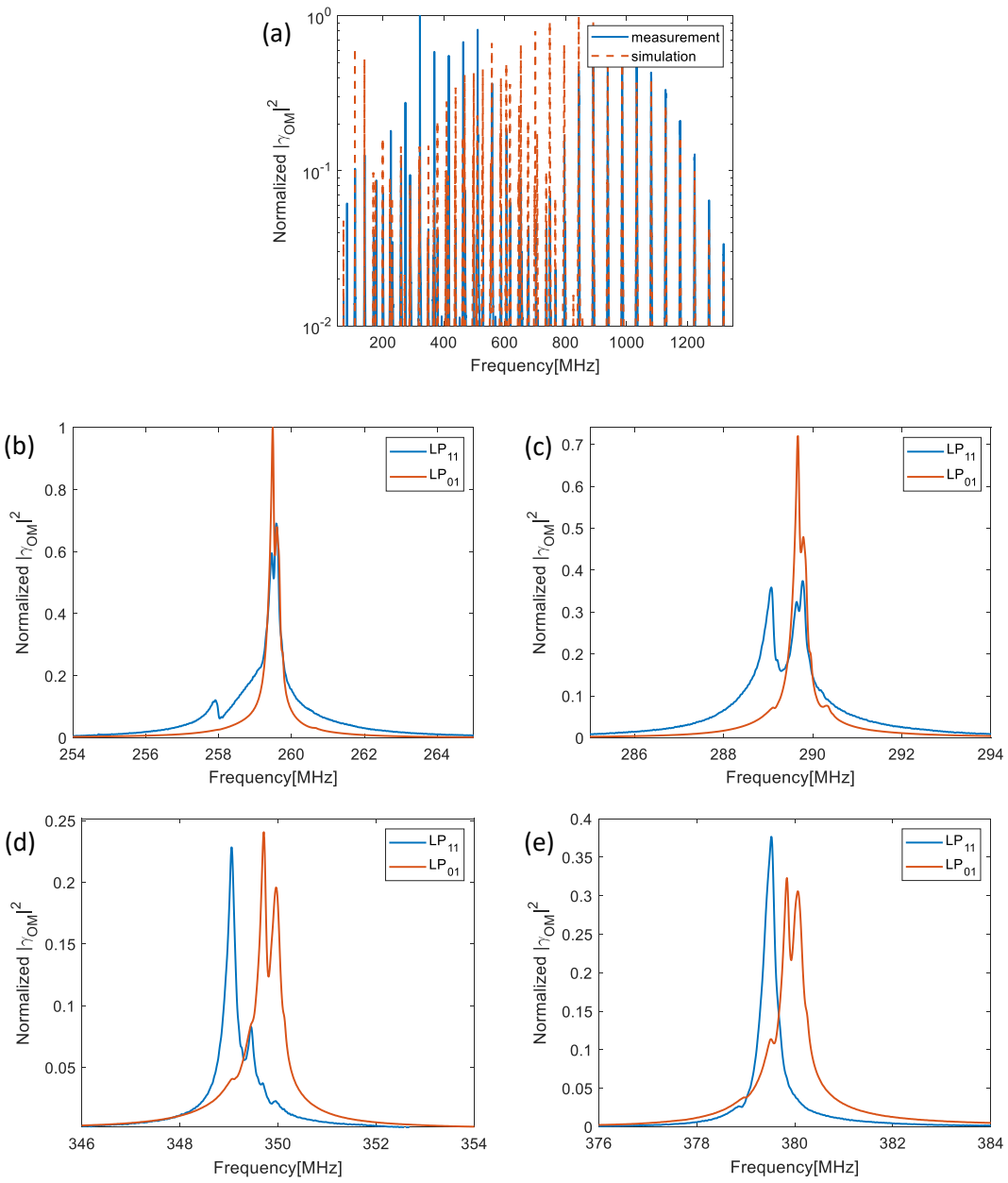

Figure 27 – (a): Measured (solid, blue) and calculated (dashed, red) normalized spectra of intra-modal forward SBS in the LP_{11} modes group of a few-mode fiber, through torsional-radial acoustic modes. The spectrum is dominated by the TR_{2m} modes. (b), (c), (d) and (e): Magnified views of the experimental trace of panel (a) (blue), alongside the measured, normalized torsional-radial modes spectrum of intra-modal scattering in the LP_{01} mode (red, repeated from Figure 24(b) as a reference). The torsional-radial acoustic modes spectrum following stimulation through the LP_{11} modes group exhibits secondary peaks, which do not appear in the corresponding LP_{01} process. The frequencies of the secondary peaks are lower than those of the primary ones by 1-2 MHz. The secondary peaks represent the stimulation of TR_{4m} acoustic modes. Four examples of pairs of peaks are shown in the figure, however others were observed as well.

Calculations also predict the stimulation of purely torsional T_{0m} acoustic modes by one field component in the TE_{01} mode and another in the TM_{01} mode within the LP_{11} group (see Figure 20(d)). The stimulation is accompanied by the coupling of optical power between the two components and may lead to polarization rotation of the combined LP_{11} polarized field. The cut-off frequencies of the T_{0m} acoustic modes are higher than those of adjacent TR_{2m} modes by 2π×1-2 MHz (as opposed to the cut-of frequencies of the TR_{4m}, which are lower than those of the TR_{2m} by comparable offsets). We were unable to resolve the stimulation of T_{0m} acoustic modes in our measurements. The division of the input field among the three constituent modes of the LP_{11} group is not controlled. It is possible that the magnitudes of the launched TE_{01} and TM_{01} fields were weak, and that the polarization rotation inducted by the T_{0m} modes was not large enough to identify alongside the much stronger response of adjacent TR_{2m} modes.

The measured normalized coupling coefficient $\mathrm{Im}\{\gamma(\Omega)\}$ of inter-modal forward SBS between the LP_{01} optical mode and the LP_{11} mode group is presented in Figure 28. The spectrum consists of stimulated TR_{1m} acoustic modes of first-order azimuthal symmetry. Forward SBS through this set of acoustic modes is also observed for the first time in this work. Like the TR_{4m} modes observed in Figure 27, the TR_{1m} set of modes cannot be stimulated in SMFs. The cut-off frequencies Ω_{1m} of these modes differ from Ω_{0m} or Ω_{2m} by tens of MHz, hence the observed peaks are distinct. The R_{0m} and TR_{2m} acoustic modes were not stimulated in this experiment, as expected. The spectrum is dominated by dilatational modes, although shear modes are observed as well at acoustic frequencies below 600 MHz.

Our analysis suggests that the inter-modal scattering process would also excite the TR_{3m} class of acoustic modes. However, the opto-mechanical coefficients for these modes are considerably weaker than those of the TR_{1m} modes (see Figure 21), and the cut-off frequencies Ω_{1m} and Ω_{3m} of the two classes differ by only 2π×1-2 MHz. We were unable to resolve the stimulation of TR_{3m} modes in our experiments, and their study remains for future work.

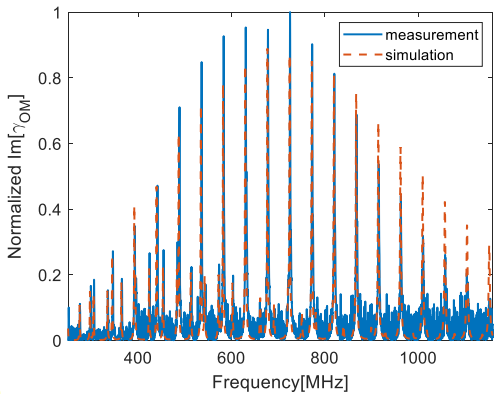

Figure 28 – Solid blue – measured normalized gain coefficient of inter-modal forward SBS between one optical wave in the fundamental LP_{01} mode and another in the LP_{11} mode group. Dashed red – calculated normalized gain coefficient $Im\{\gamma_{LP01,LP11,1m}\}$ of inter-modal forward SBS between the two optical modes through the TR_{1m} acoustic modes. Agreement with experiment is very good. The weaker stimulation of TR_{3m} modes, suggested by the analysis, was not observed in the measurements.

The normalized spectrum of inter-modal forward SBS between the LP_{01} and LP_{02} optical modes is presented in Figure 29(a). The measured response consists of the R_{0m} and TR_{2m} acoustic modes, and it agrees well with expectations. Careful comparison between the response of Figure 29(a) and the spectra of R_{0m} and TR_{2m} modes obtained through intra-modal scattering reveals a significant difference. The resonance frequencies $\Omega_{0m}^{(R)}$ and $\Omega_{2m}^{(R)}$ of the inter-modal spectrum are consistently higher than those observed through intra-modal scattering. Examples are shown in Figures 29(b), (c), (d) and (e). The difference is due to the larger axial wavenumber K of inter-modal electro-strictive stimulation (see section 3.2.4). Figure 30 plots the difference $\Delta\Omega = \Omega_{pm}^{(R)} - \Omega_{pm}$ between the inter-modal and intra-modal resonance frequencies, as a function of Ω. The difference is inversely proportional to Ω, and it follows the prediction of Eq. (98). The difference $\Delta\Omega$ is larger for dilatational modes, due to their higher velocity.

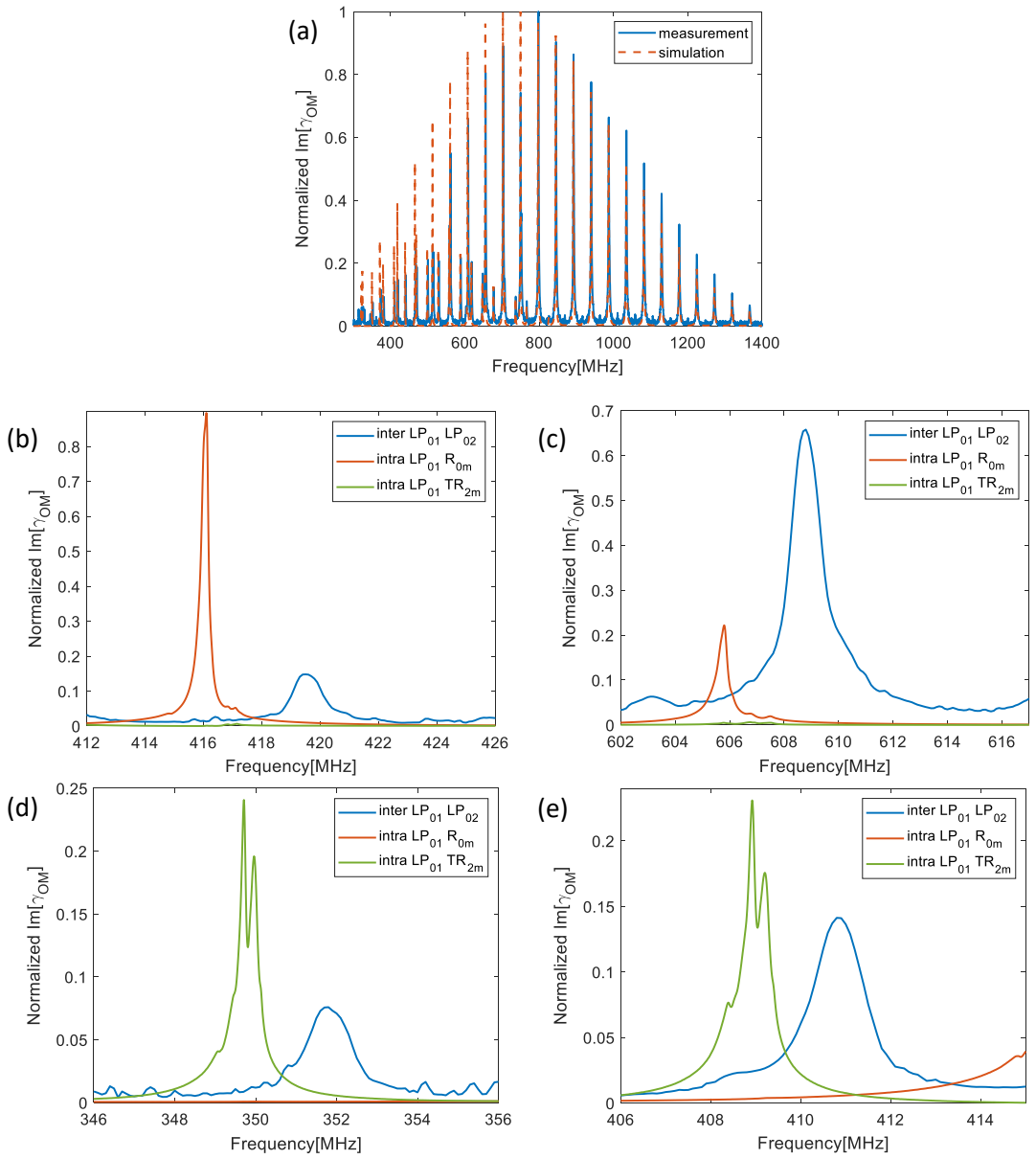

Figure 29 – (a): Solid blue – measured normalized gain coefficient of inter-modal forward SBS between one optical wave in the fundamental LP_{01} mode and another in the LP_{02} mode. Dashed red – calculated normalized gain coefficient of the inter-modal scattering process through the R_{0m} and TR_{2m} acoustic modes. Agreement with experiment is very good. (b), (c), (d) and (e): Magnified view of the measured normalized inter-modal scattering spectrum (blue), alongside the measured normalized spectra of intra-modal scattering in the fundamental LP_{01} mode. In all panels, R_{0m} modes are shown in red and TR_{2m} modes in green. In panels (b) and (c), the resonance frequencies of dilatational R_{0m} modes are higher by 3.4 MHz and 3 MHz respectively than the intra-modal trace. The corresponding differences for the TR_{2m} shear modes shown in panels (d) and (e) are 2 MHz and 1.7 MHz, respectively.

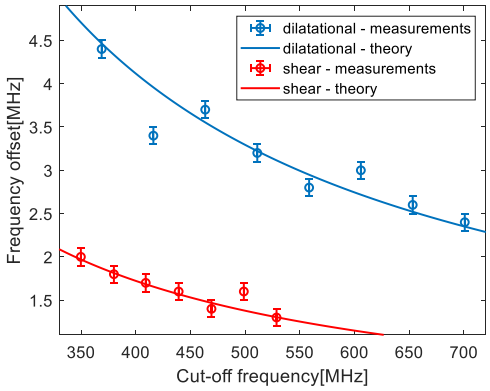

Figure 30 – Circular markers - Measured spectral offsets $\Delta\Omega/2\pi$ between the resonance frequencies of inter-modal forward SBS through the LP_{01} and LP_{02} modes, and the corresponding resonance frequencies of intra-modal scattering. The experimental uncertainties are due to the measurement resolution of 100KHz. Solid lines – calculated offsets according to Eq. (98). Modes dominated by their dilatational components are shown in blue, whereas those that are primarily of shear characteristics are shown in red. The observed spectral offsets agree with analysis. The offsets are inversely proportional to frequency, and they are larger for the dilatational modes due to their higher acoustic velocity.

5.4. Sensing demonstration

We have shown in the previous section that forward SBS in few-mode fibers can excite acoustic waves at higher frequencies than in SMFs, and addresses additional categories of acoustic modes. In particular, the TR_{1m} category has been observed for the first time, with frequencies and modal linewidths different from those of the R_{0m} and TR_{2m} classes. As discussed in section 1.3, the forward SBS effect can be used towards sensing of substances outside the fiber [36,56]. Measuring the F-SBS spectra in few-mode fibers may be utilized to enhance the capabilities of sensing protocols.

Here I present an example of the inter-modal gain coefficient of the TR_{1m} modes in the same bare FMF used above, when immersed in water. Distinction between dilatational and shear modes is observed: while the linewidths of dilatational TR_{1m} modes were broadened following immersion, those of the shear modes remained narrow. These results agree with the previous observations by our group, using the TR_{2m} modes in an SMF [56]. Addressing additional acoustic frequencies and categories might extend the characterization of the elastic properties of media outside the fiber, and enhance the application of forward SBS in fiber sensing.

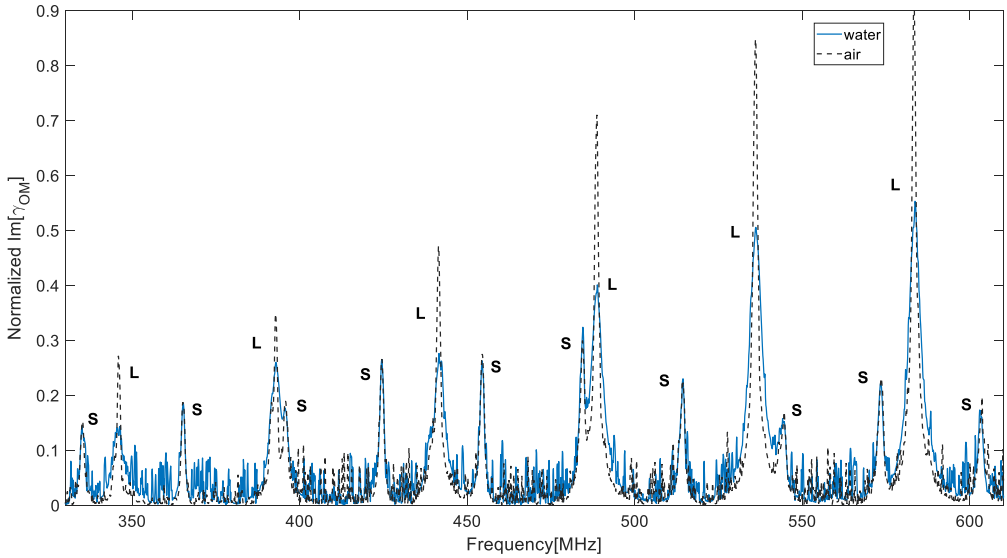

Figure 31 – Measured inter-modal forward SBS gain coefficient of the TR_{1m} modes in a bare few-mode fiber immersed in water (solid blue) and kept in air (dashed black). The linewidths of the dilatational modes (noted by L) are broadened when immersed in water, whereas the shear modes (labeled S) remain narrow.

6. Summary and discussion

6.1. Main results

This work extended the study of forward Brillouin scattering in standard, uniform-cladding fibers to the multi-optical mode regime, through analysis, calculations, and experiment. The process supports many possible combinations of intra-modal and inter-modal scattering. Acoustic modes of arbitrary azimuthal orders can be stimulated in the few-mode fiber, as opposed to the R_{0m} and TR_{2m} modes only in SMFs. In this work we experimentally demonstrated the stimulation of TR_{1m} and TR_{4m} modes. Unlike polarization maintaining or photonic crystal fibers, the forward SBS spectra in FMFs are calculated analytically.

The F-SBS spectra of the few-mode fiber extend to higher acoustic frequencies than in SMFs: resonance frequencies up to 1.8 GHz were observed in the measurements. Further, inter-modal stimulation in the few-mode fiber excited acoustic modes few MHz above their cut-off frequencies. The acoustic modes, in this case, may take up axial wavenumbers in the order of 10^4 rad×m^{-1}. Such large wavenumbers can lead to non-reciprocal coupling of signal waves between spatial optical modes and to narrowband optical isolation, as shown in polarization maintaining fibers and photonic integrated circuits [63,65].

The effect of media outside the cladding on the acoustic linewidth may differ among classes of modes [56]. Addressing additional mode groups may enhance the application of forward SBS in fiber sensing [44,45,56]. The elastic properties of media under test vary with acoustic frequency. The extension of F-SBS towards higher acoustic frequencies over few-mode fibers would enable broader characterization of acoustic dispersion.

Both the optical and acoustic waves used in this work carry angular momenta in their orbital degree of freedom [76]. The forward SBS interactions through specific choices of modes signify the exchange of orbital angular momentum quanta between the optical and mechanical domains. These interactions may potentially serve towards the manipulation of quantum states at cryogenic temperatures.

6.2. Limitations

In this work, we were not able to resolve the simulation of TR_{3m} acoustic modes alongside the TR_{1m} ones in an inter-modal forward SBS process, even though our analysis suggests that these modes should have been observed. The difficulty may have to do with the limited signal-to-noise ratio of the inter-modal measurements protocol, and the small separation between the cut-off frequencies of the TR_{1m} and TR_{3m} modes. We also could not observe the stimulation of the T_{0m} acoustic modes by optical fields within the LP_{11} mode group. The monitoring of forward Brillouin scattering within the LP_{11} group relies on polarization rotation. It is possible that the rotation associated with the coupling of light between the TE_{01} and TM_{01} field components within the LP_{11} group was too weak to be detected. The identification of the T_{0m} acoustic mode is challenging due to the presence of adjacent, stronger peaks associated with the TR_{2m} modes category. The stimulation of the T_{0m} and TR_{3m} will be revisited in future work.

6.3. Future works

While the characterization of forward Brillouin scattering in few-mode fibers has been rather extensive, it is by no means exhaustive. Even with three-mode fiber available to us, there are many additional possible combinations for the allocation of input fields to specific modes. For example, two intra-modal scattering processes can be coupled through a common acoustic mode: A pair of pump waves in a common optical mode 1 would stimulate the acoustic wave through a first intra-modal process, and a signal wave in optical mode 2 would be scattered by the same acoustic wave in a second intra-modal process. We have successfully demonstrated such coupling between intra-modal forward SBS processes in polarization maintaining fibers [65], and their exploration over FMFs remains for future study.

Moreover, inter-modal forward SBS is associated with the amplification of one input optical field at the expense of another [11]. This amplification mechanism has been the basis for a forward Brillouin laser over polarization maintaining fiber [66] and may support similar lasing in few-mode fiber as well. The gain bandwidth of forward Brillouin scattering is extremely narrow, only 100 kHz in bare fibers, hence forward Brillouin lasers can become extremely coherent. The boundary conditions of acoustic modes make forward Brillouin fiber lasers highly sensitive to their environment [66]. Compared with polarization maintaining fibers, the few-mode fibers provide

greater freedom for the choice of modes and the design of forward Brillouin lasers, and their examination remains for future work as well.

In summary, the study of forward SBS in standard FMFs extends the fundamental understanding and formulation of the effect, reaches higher acoustic frequencies and additional modal symmetries, and may find applications in fiber sensing, fiber lasing, non-reciprocal propagation, and quantum technologies.

References

[1] G. P. Agrawal, “Fiber-Optic Communication Systems 3rd Edition,” Wiley-Interscience (2002).

[2] E. Udd and W. B. Spillman WB (Eds.), “Fiber Optic Sensors: An Introduction for Engineers and Scientists,” Second Edition. John Wiley & Sons (2011).

[3] K. T. V. Grattan and B. T. Meggit (Eds.), “Optical Fiber Sensor Technology Volume 4, Chemical and Environmental Sensing.” Kluwer academic publishers (2010).

[4] L. Brillouin, “Diffusion de la lumière et des rayons X par un corps transparent homogène,” Ann Phys (Paris), vol. 9, no. 17, pp. 88–122 (1922).

[5] R. G. Brewer and K. E. Rieckhoff, “Stimulated Brillouin Scattering in Liquids,” Phys Rev Lett, vol. 13, no. 11, pp. 334–336 (1964).

[6] E. P. Ippen and R. H. Stolen, “Stimulated Brillouin scattering in optical fibers,” Appl Phys Lett, vol. 21, no. 11, pp. 539–541 (1972).

[7] R. M. Shelby, M. D. Levenson, and P. W. Bayer, “Guided acoustic-wave Brillouin scattering,” Phys. Rev. B 31, 5244–5252 (1985).

[8] A. S. Biryukov, M. E. Sukharev, and E. M. Dianov, “Excitation of sound waves upon propagation of laser pulses in optical fibers,” Quantum Electron. 32, 765–775 (2002).

[9] P. St.J. Russell, D. Culverhouse, and F. Farahi, “Experimental observation of forward stimulated Brillouin scattering in dual-mode single-core fibre,” Electron. Lett. 26, 1195–1196 (1990).

[10] P. St.J. Russell, D. Culverhouse, and F. Farahi, “Theory of forward stimulated Brillouin scattering in dual-mode single-core fibers,” IEEE J. Quantum Electron. 27, 836–842 (1991).

[11] A. Zadok, H. H. Diamandi, Y. London, and G. Bashan, Forward Brillouin Scattering in Standard Optical Fibers, Springer Series in Optical Sciences (Springer, 2022).

[12] M. Nikles, L. Thevenaz and P. A. Robert, "Brillouin gain spectrum characterization in single-mode optical fibers," J. Lightwave Technol. 15, 1842-1851 (1997).

[13] A. Kobyakov, M. Sauer, and D. Chowdhury, "Stimulated Brillouin scattering in optical fibers," Adv. Opt. Photon. 2, 1-59 (2010).

[14] A. Zadok, X. Bao, Z. Yang, and L. Thevenaz, “Chapter Seven - SBS-based fiber sensors,” in Brillouin Scattering Part 2, B. J. Eggleton, M. J. Steel, and C. G. Poulton, Eds., in Semiconductors and Semimetals, vol. 110. Elsevier (2022).

[15] T. Horiguchi and M. Tateda, “Optical-fiber-attenuation investigation using stimulated Brillouin scattering between a pulse and a continuous wave,” Opt Lett, vol. 14, no. 8, p. 408 (1989).

[16] R. Cohen, Y. London, Y. Antman, and A. Zadok, “Brillouin optical correlation domain analysis with 4 millimeter resolution based on amplified spontaneous emission,” Opt Express, vol. 22, no. 10, p. 12070 (2014).

[17] A. Zarifi et al., “Highly localized distributed Brillouin scattering response in a photonic integrated circuit,” APL Photonics, vol. 3, no. 3 (2018).

[18] S. Chin, N. Primerov, and L. Thevenaz, “Sub-Centimeter Spatial Resolution in Distributed Fiber Sensing Based on Dynamic Brillouin Grating in Optical Fibers,” IEEE Sens J, vol. 12, no. 1, pp. 189–194 (2012).

[19] A. Dominguez-Lopez, M. A. Soto, S. Martin-Lopez, L. Thevenaz, and M. GonzalezHerraez, “Resolving 1 million sensing points in an optimized differential time-domain Brillouin sensor,” Opt Lett, vol. 42, no. 10, p. 1903 (2017).

[20] Y. Dong *et al.*, “150 km fast BOTDA based on the optical chirp chain probe wave and Brillouin loss scheme,” Opt. Lett., vol. 43, no. 19, pp. 4679–4682 (2018).

[21] X. Angulo-Vinuesa *et al.*, “Brillouin optical time-domain analysis over a 240 km-long fiber loop with no repeater,” Y. Liao, W. Jin, D. D. Sampson, R. Yamauchi, Y. Chung, K. Nakamura, and Y. Rao, Eds. (2012).

[22] B. Wang, D. Ba, Q. Chu, L. Qiu, D. Zhou, and Y. Dong, “High-sensitivity distributed dynamic strain sensing by combining Rayleigh and Brillouin scattering,” OptoElectronic Advances, vol. 3, no. 12, pp. 20001301–20001315 (2020).

[23] H. Wu *et al.*, “High-performance distributed dynamic strain sensing by synthesizing ϕ-OTDR and BOTDR,” Opt Express, vol. 31, no. 11, p. 18098 (2023).

[24] S. P. Smith, F. Zarinetchi, and S. Ezekiel, “Narrow-linewidth stimulated Brillouin fibre laser and applications,” Opt. Lett. 16, 393–395 (1991).

[25] S. Molin, G. Baili, M. Alouini, D. Dolfi, and J. P. Huignard, “Experimental investigation of relative intensity noise in Brillouin fiber ring lasers for microwave photonics applications,” Opt. Lett. 33, 1681–1683 (2008).

[26] F. Zarinetchi, S. P. Smith, and S. Ezekiel, “Stimulated Brillouin fiber-optic laser gyroscope,” Opt. Lett. 16, 229–231 (1991).

[27] I. S. Grudinin, A. B. Matsko, and L. Maleki, “Brillouin lasing with a CaF2 whispering gallery mode resonator,” Phys. Rev. Lett. 102, 043902 (2009).

[28] I. V. Kabakova *et al.* “Narrow linewidth Brillouin laser based on chalcogenide photonic chip,” Opt. Lett. 38, 3208–3211 (2013).

[29] G. Bahl, J. Zehnpfennig, M. Tomes, and T. Carmon, “Stimulated optomechanical excitation of surface acoustic waves in a microdevice,” Nat. Commun. 2, 403 (2011).

[30] J. Li, H. Lee, T. Chen, and K. J. Vahala, “Characterization of a high coherence, Brillouin microcavity laser on silicon,” Opt. Express 20, 20170–20180 (2012).

[31] S. Gundavarapu *et al.,* “Sub-hertz fundamental linewidth photonic integrated Brillouin laser,” Nat. Photon. 13, 60–67 (2019).

[32] S. W. Hirschberg and A. Rienstra, “An Introduction to Acoustics.” Eindhoven University of Technology, The Netherlands, Chap. 7, p. 296 (2015).

[33] R. W. Boyd, “Nonlinear Optics,” Book, p. 613 (2008).

[34] C. Wolff, M. J. Steel, B. J. Eggleton, and C. G. Poulton, “Stimulated Brillouin Scattering in integrated photonic waveguides: forces, scattering mechanisms and coupled mode analysis,” (2015).

[35] Y. Shi, A. Cerjan, and S. Fan, “Invited Article: Acousto-optic finite-difference frequency-domain algorithm for first-principles simulations of on-chip acousto-optic devices,” APL Photonics, vol. 2, no. 2, p. 20801 (2017).

[36] Y. Antman, A. Clain, Y. London, and A. Zadok, "Optomechanical sensing of liquids outside standard fibers using forward stimulated Brillouin scattering," Optica 3, 510-516 (2016).

[37] N. Hayashi, Y. Mizuno, K. Nakamura, S. Y. Set, and S. Yamashita, “Experimental study on depolarized GAWBS spectrum for optomechanical sensing of liquids outside standard fibers,” Opt. Express 25, 2239–2244 (2017).

[38] D. M. Chow, Z. Yang, M. A. Soto, and L. Thévenaz, “Distributed forward Brillouin sensor based on local light phase recovery,” Nat. Commun. 9, 2990 (2018).

[39] D. M. Chow and L. Thévenaz, “Forward Brillouin scattering acoustic impedance sensor using thin polyimide-coated fiber,” Opt. Lett. 43, 5467–5470 (2018).

[40] G. Bashan, H. H. Diamandi, Y. London, E. Preter, and A. Zadok, "Optomechanical time-domain reflectometry," Nature Communications 9, 2991 (2018).

[41] H. H. Diamandi, Y. London, G. Bashan, and A. Zadok, "Distributed opto-mechanical analysis of liquids outside standard fibers coated with polyimide," Appl. Phys. Lett. – Photon. 4, 016105 (2019).

[42] H. H. Diamandi, Y. London, G. Bashan, K. Shemer and A. Zadok, "Forward Stimulated Brillouin Scattering Analysis of Optical Fibers Coatings," J. Lightwave Technol. 39, 1800-1807 (2021).

[43] Y. London, K. Sharma, H. H. Diamandi, M. Hen, G. Bashan, E. Zehavi, S. Zilberman, G. Berkovic, A. Zentner, M. Mayoni, A. A. Stolov, M. Kalina, O. Kleinerman, E. Shafir, and A. Zadok, "Opto-Mechanical Fiber Sensing of Gamma Radiation," J. Lightwave Technol. 39, 6637-6645 (2021).

[44] L. A. Sánchez, A. Díez, J. L. Cruz, and M. V. Andrés, "High accuracy measurement of Poisson's ratio of optical fibers and its temperature dependence using forward-stimulated Brillouin scattering," Opt. Express 30, 42-52 (2022).

[45] L. A. Sánchez, A. Díez, J. L. Cruz, and M. V. Andrés, "Recent Advances in Forward Brillouin Scattering: Sensor Applications," Sensors 23, 318 (2022).

[46] Z. Hua, D. Ba, D. Zhou, Y. Li, Y. Wang, Z. Bao, and Y. Dong, "Non-destructive and distributed measurement of optical fiber diameter with nanometer resolution based on coherent forward stimulated Brillouin scattering," Light: Advanced Manufacturing 2, 373-384 (2022).

[47] G. Yang, K. Zeng, L. Wang, M. Tang, and D. Liu, "Simultaneous sensing of temperature and strain with enhanced performance using forward Brillouin scattering in highly nonlinear fiber," Opt. Lett. 48, 3611-3614 (2023).

[48] K. Zeng, G. Yang, Z. Xu, L. Song, L. Wang, M. Tang, and D. Liu, "High-sensitivity acoustic impedance sensing based on forward Brillouin scattering in a highly nonlinear fiber," Opt. Express 31, 8595-8609 (2023).

[49] T. Li, H. Zhang, H. Li, Y. Ren, C. Chen, D. Ba, and Y. Dong, "3-mm Recognition Capability of Forward Stimulated Brillouin Scattering Measurement by Brillouin Selective Sideband Amplification," J. Lightwave Technol. 42, 898-906 (2024).

[50] T. Li, H. Li, C. Chen, Y. Ren, T. Jiang, L. Qiu, D. Ba, and Y. Dong, "Forward Brillouin Scattering for Bubble and Flow Interruption Detection Toward Microscale Liquid Systems," J. Lightwave Technol. doi: 10.1109/JLT.2024.3445167 (2024).

[51] L. A. Sánchez, M. Delgado-Pinar, A. Díez, M. V. Andrés, "Forward Brillouin Scattering Spectroscopy in Optical Fibers with Whispering-Gallery Modes," Adv. Optical Mater. 12, 2301629 (2024).

[52] K. Shemer *et al.*, “Optical fiber point sensors based on forward Brillouin scattering,” Opt Express, vol. 30, no. 22, p. 39321 (2022).

[53] C. Pang *et al.*, “Opto-mechanical time-domain analysis based on coherent forward stimulated Brillouin scattering probing,” Optica, vol. 7, no. 2, p. 176 (2020).

[54] S. Zaslawski, Z. Yang, and L. Thévenaz, “Distributed optomechanical fiber sensing based on serrodyne analysis,” Optica, vol. 8, no. 3, p. 388 (2021).

[55] K. Sharma, E. Zehavi, H. H. Diamandi, G. Bashan, Y. London, and A. Zadok, “Direct time-of-flight distributed analysis of nonlinear forward scattering,” Optica, vol. 9, no. 4, p. 419 (2022).

[56] A. Bernstein, E. Zehavi, Y. London, M. Hen, R. Suna, S. Ben-Ami, and A. Zadok, “Tensor characteristics of forward Brillouin sensors in bare and coated fibers,” APL Photonics 8, article no, 126105 (2023).

[57] O. E. Delange, “Wideband optical communication systems, Part 2-Frequency division multiplexing,” Proc. IEEE, vol. 58, p. 1683 (1970).

[58] W. Tomlinson, “Wavelength multiplexing in multimode optical fibers,” Appl. Opt., vol. 18, no. 8, pp. 2180-2194 (1977).

[59] K. Nosu and H. Ishio, “A design of optical multi/demultiplexers for optical wavelength-division multiplexing transmission,” Trans. IECE, vol.62-B, pp. 1030-1036 (1979).

[60] D. J. Richardson, J. M. Fini, and L. E. Nelson, “Space-division multiplexing in optical fibers,” Nat. Photonics, vol. 7, no. 5, pp. 354–362 (2013).

[61] R. Ryf et al., “Mode-Division Multiplexing Over 96 km of Few-Mode Fiber Using Coherent 6 x 6 MIMO Processing,” J. Light. Technol., vol. 30, no. 4, pp. 521–531 (2012).

[62] J. A. Buck, “Fundamentals of optical fibers.” Vol. 50. John Wiley & Sons (2004).

[63] E. A. Kittlaus, N. T. Otterstrom, and P. T. Rakich. "On-chip inter-modal Brillouin scattering," Nat. Commun. 8, 15819 (2017).

[64] N. T. Otterstrom, R. O. Behunin, E. A. Kittlaus, Z. Wang, and P. T. Rakich, "A silicon Brillouin laser," Science 360, 1113-1116 (2018).

[65] G. Bashan, H. H. Diamandi, Y. London, K. Sharma, K. Shemer, E. Zehavi, and A. Zadok, “Forward stimulated Brillouin scattering and opto-mechanical non-reciprocity in standard polarization maintaining fibres,” Light Sci. Appl. 10, 119 (2021).

[66] G. Bashan, H. H. Diamandi, E. Zehavi, K. Sharma, Y. London, and A. Zadok, “A forward Brillouin fiber laser,” Nat Commun 13, 3554 (2022).

[67] W. Xu, A. Iyer, L. Jin, S. Y. Set, and W. H. Renninger, “Strong optomechanical interactions with long-lived fundamental acoustic waves,” Optica 10, 206-213 (2023).

[68] K. Y. Song, Y. H. Kim, and B. Y. Kim, “Intermodal stimulated Brillouin scattering in two-mode fibers,” Opt. Lett. 38, 1805-1807 (2013).

[69] Y. H. Kim and K. Y. Song, “Recent Progress in Distributed Brillouin Sensors Based on Few-Mode Optical Fibers,” Sensors 21, 2168 (2021).

[70] B. A. Auld, Acoustic fields and waves in solids. New York: Wiley (1973).

[71] R. N. Thurston, “Elastic waves in rods and optical fibers,” J Sound Vib, vol. 159, no. 3, pp. 441–467 (1992).

[72] E. Sittig, “Zur Systematik der elastischen Eigenschwingungen isotroper Kreiszylinder,” Acta Acustica united with Acustica, vol. 7, no. 3, pp. 175–180 (1957).

[73] Qiu, W., P. T. Rakich, H. Shin, H. Dong, M. Soljačić, and Z. Wang, “Stimulated Brillouin scattering in nanoscale silicon step-index waveguides: a general framework of selection rules and calculating SBS gain,” Opt. Express 21, 31402–31419 (2013).

[74] J. Wang, Y. Zhu, R. Zhang, and D. J. Gauthier, "FSBS resonances observed in a standard highly nonlinear fiber," Opt. Express 19, 5339-5349 (2011).

[75] M. S. Kang, A. Nazarkin, A. Brenn, and P. St. J. Russell, “Tightly trapped acoustic phonons in photonic crystal fibres as highly nonlinear artificial Raman oscillators,” Nat. Phys. 5, 276–280 (2009).

[76] H. H. Diamandi, G. Bashan, Y. London, K. Sharma, K. Shemer, and A. Zadok, "Inter-polarization Forward Stimulated Brillouin Scattering in Standard Single-Mode Fibers," Laser Photon. Rev. 16, 2100337 (2022).

[77] Y. London, H. H. Diamandi, G. Bahsan, and A. Zadok, “Distributed analysis of nonlinear wave mixing in fiber due to forward Brillouin scattering and Kerr effects,” Appl. Phys. Lett. – Photon. 3, 110804 (2018).

תקציר

פיזור ברילוואן הינה תופעה אופטו-מכאנית שמצמדת בין גלים אופטיים ואקוסטיים בתווך משותף. התופעה נחקרת בסיבים סטנדרטיים למעלה מחמישים שנה, ומתקיימת הן בכיוון האחורי והן בכיוון הקדמי. בפיזור ברילוואן אחורי, שני שדות אופטיים שמתקדמים בכיוונים הפוכים יכולים לעורר אופן אקוסטי אורכי שמולך בליבה של הסיב האופטי. בפיזור ברילוואן קדמי, שני שדות אופטיים שמתקדמים יחדיו יכולים לעורר אופנים אקוסטיים רוחביים שמשתרעים על פני כל שטח החתך של מעטה הסיב. פיזור ברילוואן קדמי בסיבים בעלי אופן יחיד דווח לראשונה בשנת 1985. בשנים האחרונות גדל העניין בתופעה, למטרות חישה של נוזלים מחוץ לגבולות הסיב, היכן שהאור המולך בסיב לא מגיע. קצבי הדעיכה של האופנים האקוסטיים מושפעים מתנאי השפה האלסטיים בגבולות המעטה של הסיב, והמדידה שלהם מאפשרת ניתוח ואיסוף נתונים על התווך מחוץ לסיב.

רוב המחקרים על פיזור ברילוואן קדמי בסיבים סטנדרטיים התבצעו בסיבים בעלי אופן יחיד. זוג של שדות אופטיים באופן היסודי היחיד יכולים לעורר אופנים אקוסטיים משני סוגים ספציפיים בלבד: אופנים בעלי סימטריה רדיאלית, ואופנים בעלי סימטריה זוויתית מסדר שני. למרות שהמעטה של הסיב תומך בהולכה של אופנים אקוסטיים בעלי כל סדר זוויתי שלם כלשהו, לא ניתן לעורר סוגים נוספים של אופנים אקוסטיים בסיבים בעלי אופן אופטי יחיד. היעילות של פיזור ברילוואן קדמי נקבעת לפי החפיפה המרחבית בין הפרופילים הרוחביים של האופנים האופטיים והאקוסטיים המעורבים. בסיבים סטנדרטיים בעלי אופן יחיד, החפיפה מקסימלית עבור אופנים אקוסטיים בתחום תדרים בין 200-600 מגה-הרץ. מעל תחום תדרים זה יעילות האפקט יורדת משמעותית. בנוסף, עירור של אופנים אקוסטיים בתהליך פיזור ברילוואן קדמי בסיבים בעלי אופן יחיד יכול להתבצע רק בתדרי הקטעון של האופנים האקוסטיים. בגבול זה, האופנים האקוסטיים הינם רוחביים כמעט לגמרי, ומספר הגל הצירי שלהם זניח.

במהלך העשור האחרון, סיבים אופטיים בעלי מספר אופנים ממלאים תפקיד משמעותי בטכנולוגיות ריבוב מרחבי של ערוצי תקשורת אופטית, ומשתמשים בהם בנוסף לצורכי חישה רבים. מספר קבוצות האופנים שנתמכים על ידי הסיב נקבע לפי המימדים ומקדם השבירה של הליבה. סיבים בעלי מספר אופנים מאפשרים דרגות חופש נוספות לאינטראקציות של פיזור ברילוואן, משום שניתן להוליך בהם את השדות האופטיים המשתתפים בתהליך באופנים מרחביים שונים. אינטראקציות של פיזור ברילוואן עם אופנים אופטיים מרובים הודגמו במוליכי גל פוטוניים משולבים ובסיבים דקים בקוטר של כ- 1 מיקרון. פיזור ברילוואן אחורי נחקר בסיבים סטנדרטיים בעלי מספר אופנים, והודגם שימוש לצורך חישה של טמפרטורה ומעוות ולמדידה של דיספרסיה מודאלית. פיזור ברילוואן קדמי נחקר בסיבים משמרי קיטוב סטנדרטיים מסוג פנדה, בהם שני מצבי הקיטוב הראשיים אינם מנוונים ומהווים שני אופנים מרחביים שונים. ואולם, ההבדל בין מקדמי השבירה של שני האופנים של הסיב הוא קטן באופן יחסי, מסדר גודל של הספרה הרביעית אחרי הנקודה העשרונית בלבד. בנוסף, האופנים האוקסטיים שמולכים בסיב משמר קיטוב לא ניתנים לפתרון אנליטי ואין להם סימטריה זוויות מוגדרת. עד עתה, פיזור ברילוואן קדמי בסיבים בעלי מספר אופנים טרם נחקר.

בעבודה זו אני מציג ניתוח מתמטי, חישובים כמותיים, והדגמה נסיונית של פיזור בריללוואן קדמי בסיב בעל מספר אופנים עם מעטה אחיד ופרופיל מקדם שבירה מסוג מדרגה בין הליבה למעטה. הספקטרום של פיזור בריללוואן קדמי מנוסח עבור התקדמות השדות האופטיים והגל האקוסטי באופנים כלליים כלשהם. המערך הנסיוני תומך בצימוד סלקטיבי של אור לאופן היסודי של הסיב LP_{01}, לאופן LP_{02}, ולקבוצת האופנים LP_{11}. התוצאות הנסיוניות מראות שפיזור בריללוואן קדמי באופן האופטי LP_{02} תומך בעירור של אופנים אקוסטיים עד לתדרים של 1.8 גיגה-הרץ, תדרים גבוהים משמעותית בהשוואה לעירור באמצעות האופן היסודי. התוצאות גם מדגימות עירור של אופנים אקוסטיים מקטגוריות נוספות, בעלי סימטריה זוויתית מסדר ראשון ומסדר רביעי. קבוצות אלו של אופנים אקוסטיים לא ניתנות לעירור בסיבים בעלי אופן יחיד. בנוסף לכך, אינטראקציות בין-אופניות בין שדות אופטיים באופנים LP_{01} וLP_{02} מעוררות אופנים אקוסטיים שמוסטים מתדר הקטעון שלהם במספר מגה-הרצים. אינטראקציות של פיזור בריללוואן קדמי בין אופנים אופטיים שונים כרוכות במעבר של תנע זוויתי בין דרגות חופש אורביטליות של גלים אופטיים ואקוסטיים. התוצאות מרחיבות את הידע בתחום של אופטו-מכאניקה בסיבים אופטיים, וניתנות ליישום לצרכי חישה, לייזרי סיב, ומניפולציות של מצבים קוונטים.

עבודה זו נעשתה בהדרכתו של פרופ׳ אבי צדוק
מן הפקולטה להנדסה ע״ש אלכסנדר קופקין של
אוניברסיטת בר-אילן

אוניברסיטת בר אילן

אינטראקציות אופטו-מכאניות בסיבים בעלי מספר אופנים

אלעד ליוש

עבודה זו מוגשת כחלק מהדרישות לשם קבלת תואר מוסמך בפקולטה להנדסה
ע״ש אלכסנדר קופקין של אוניברסיטת בר אילן

רמת גן תשפ״ה